technische universität
dortmund

Inverse Faraday Effect and Optical Orientation under Excitation with a Train of Optical Pulses in Solid State Systems.

by Manuel Jäckl

Dissertation

presented to the Faculty of Physics of the
Technische Universität Dortmund, Germany,
in partial fulfillment of the requirements
for the degree of

Dr. rer. nat

Dortmund, November 2017

1. Gutachter: PD Dr. Ilya Akimov
2. Gutachter: Prof. Dr. Manfred Bayer

Datum des Einreichens der Arbeit: 24. November 2017
Datum der Disputation: 12. Januar 2018

Kurzfassung

Ein großer Teil der wissenschaftlichen Forschung beschäftigt sich heutzutage mit möglichen Alternativen zur bisherigen Informationstechnologie. Ein heißer Kandidat sind Spin Waves (SW) um Ladungen als Informationsträger abzulösen, wodurch Ohmische Verluste verringert werden würden. Die Erzeugung durch ultrakurze Laserpulse liefert einige Vorteile gegenüber der konventionelleren Methode mit Mikrowellen-Antennen. Fokussierte Laserstrahlen dienen hier als Punktquelle der SW und erlauben die Kontrolle der Ausbreitungsrichtung oder das Auswählen der jeweiligen SW Klasse. Ein einzlener Laserpuls erzeugt jedoch nur SW mit einem sehr breiten Frequenzspektrum, was sich in kurzen Propagationslängen und geringen Amplituden niederschlägt. In unserem Ansatz induzieren wir über den inversen Faraday Effekt eine Magnetisierungspräzession in magnetischen Bismuth-Eisengranat-Filmen mit zurkular polarisierten Femtosekunden Laserpulsen. Regen wir das System jedoch periodisch an mit einem Lasersystem basierend auf der ASOPS Technolgie und mit 1 GHz Repetitionsrate, so dass das Pulsintervall kürzer als die Relaxationszeit der Präzession ist, dann kann die Amplitude signifikant verstärkt werden. Diese kollektive Anregung der Magnetisierung erzeugt eine quasistationäre Quelle an SWs, eine kohärente Akkumulation von Magnonen („Magnonen Wolke"). Dieser Ansatz hat einige Vorteile: (i) Die Magnonen Quelle ist verstimmbar, (ii) die SW Amplitude kann deutlich verstärkt werden, (iii) das Spektrum der erzeugten SWs ist sehr schmal was zu wesentlich längeren Propagationslängen führt, (iv) die SW Amplitude ist annäherend ohne zeitliche Dämpfung sobald die SW sich 20 μm oder mehr von der Quelle entfernt haben und (v) die SW Emission hat eine verstellbare Vorzugsrichtung. Wenn der Q-Faktor der angeregten Mode sehr groß ist, also ihre Lebensdauer deutlich länger als das Pulsintervall ist, dann lässt sich die Wellenlänge der erzeugten SWs zwischen 15 und einigen hundert Mikrometer verstellen indem die externe Magnetfeldstärke oder die Pulsrate nur leicht verändert werden. Die vorgestellten Resultate erweitern die Möglichkeiten der ultraschnellen, kohärenten optischen Manipulierung der Magnetisierung und liefern neue Methoden zur SW Erzeugung und Kontrolle, was für zukünftige Anwendungen in der Datenverarbeitung wichtig sein kann.

Auf der anderen Seite kann die optische Orientierung (optical orientation) ein nützliches Werkzeug sein um Spin Kohärenz- und Dephasierungszeiten zu bestimmen. Die Probe, eine CdTe/CdMgTe Quantentopf-Halbleiter-Struktur, wird wieder periodisch mit zirkular polarisierten Laserpulsen angeregt, welche eine Spinpräzession in dieser anregen. Wenn resonant angeregt wird, so verstärkt sich die Präzessionsamplitude und aus ihrer Resonanzlinie kann die Spin-Dephasierungszeit T_2^* und der Lande-Faktor g bestimmt werden.

Abstract

Nowadays, a considerable part of the scientific research is searching for suitable alternatives to the state-of-the-art information technology. Spin waves (SWs) are considered as an alternative to charge currents for computation and data processing to diminish Ohmic losses. The generation of spin waves by ultrashort laser pulses provides several important advances with respect to conventional approaches using microwave antennas. In particular, focused laser spot works as a point source for spin waves and allows for directional control of spin waves and switching between their different types. However, a single laser pulse can inject spin waves (SWs) only with a broad frequency spectrum, resulting in short propagation distances and low wave amplitudes. In our approach we use the inverse Faraday effect in order to perturb the magnetization in magnetic Bismuth iron garnet films by means of circularly polarized femtosecond laser pulses. Using a laser system based on the ASOPS technology, we excite by a train of fs-laser pulses with a 1-GHz repetition rate so that the pulse separation is shorter than the decay time of magnetic modes. Then, the precession amplitude can be significantly magnified, depending on the quality-factor of the excited mode. This allows us to achieve a collective impact on the magnetization and establish a quasistationary source of spin waves, namely, a coherent accumulation of magnons (,Äòmagnon cloud,Äô). This approach has several appealing features: (i) The magnon source is tunable, (ii) the SW amplitude can be significantly enhanced, (iii) the SW spectrum is quite narrow, providing long-distance propagation, (iv) the periodic pumping results in an almost constant-in-time SW amplitude for the distances larger than $20\,\mu$m away from the source, and (v) the SW emission shows pronounced directionality. If the quality-factor of the excited mode is relatively large, i.e. its relaxation time is much longer than the pulse interval of the optical excitation, the wavelength of the SWs can be tuned from 15 to hundreds of micrometers by sweeping the external magnetic field by only a few percent or by a slight variation of the pulse repetition rate. The results expand the capabilities of ultrafast coherent optical control of magnetization and provide a new method for SW generation and control, which might pave the way for applications in data processing, including the quantum regime.

On the other hand, optical orientation experiments offer a helpful tool to determine spin coherence and dephasing times. The sample, a CdTe/CdMgTe quantum well semiconductor structure, is again excited by a train of circularly polarized laser pulses which inject a spin precession. If we again excite resonantly, using the ASOPS based laser system with 1 GHz repetition rate, the precession amplitude can be amplified and by the width of the resonance lines, we were able to evaluate the spin dephasing time T_2^* and electron g-factor.

Contents

List of Figures

List of Tables

1 Motivation and Outline

Our modern world is inconceivable connected with information technology (IT) and a big part of today's mankind's progress relies on its improvement. Basically it consists of three parts: data storage, data processing and data transfer. An ever growing data volume justifies the obligation for an increasing data storage density and we are just at the beginning of the 'age of big data': a recently published IDC whitepaper predicts that in the year 2025 the worldwide stored digital data amounts to 163 zetabytes[a] [Reinsel et al., 2017], a tremendous growth from 0.295 zetabytes in the year 2007. For decades, data storage would have been much less effective without sophisticated knowledge about magnetism. The breakthrough milestone in this topic was the discovery of the giant magnetoresistance (GMR) in 1988, independently by the groups of Albert Fert in Paris, France, and Peter Grünberg in Jülich, Germany [Baibich et al., 1988; Binasch et al., 1989]. Nine years later it was utilized by IBM for reading heads of hard disk drives, enabling the first multigigabyte storage capicities. An improvement of modern data storage techniques does not only include an increase of data density and therefore higher capacity, but also a progress in read and write speeds. In HDDs, the direction of the magnetization of each bit is seen as a '0' or '1', reversing this direction is usually performed by applying an anti-parallel directed external magnetic field, which has limitations in recording speed. In 1996 demagnetization by a 60 femtosecond laser pulse was demonstrated [Beaurepaire et al., 1996], and recently, an all-optical way of magnetic recording has been presented which outperforms conventional ways in terms of the write-read speed ($< 20\,\mathrm{ps}$) and heat load ($< 6\,\mathrm{J/cm^2}$) performance [Stupakiewicz et al., 2017].

In the last years, solid state disks (SSDs) started to replace the conventional magnetic recording method for private computers, using electronic charges for data storage. This is similar to the core of today's IT: the integrated circuit on semiconductor materials. Charges are here the equivalent to the magnetization direction in magnetic data storage: off and on are related to the '0' and '1' bit, respectively. Improving the performance of semiconductor chips is realized by decreasing size and therefore implementing more transistors on the same area. This led to an enormous growth of transistors per chip in the last decades. The *Moore's law* is cited often in this context, predicting a doubling of performance each about 18 months [Moore, 1965]. It has described quite accurately the development for electrical calculations per second for almost one century, but state of the art technology is close to fundamental limits determined by the underlying physics. The width of the nodes on modern

---

[a] 1 zetabyte = 1 trillion gigabytes = 10^{21} bytes

integrated circuits are in the order of tens of nanometers. A further shrinking will, at one point, inevitably lead to quantum effects due to confinement of the charge carriers (see also Sec. 2.4) and latest when reaching atomic sizes a boundary is reached which cannot be overcome. As soon as the sizes are as low as a few nanometers, quantum uncertainties will make transistors useless. But even before reaching fundamental limits, other disadvantages of electric currents become apparent when increasing performance density. One example are Ohmic losses, occurring in all electric devices, leading to a heating of the system. A further shrinking of the logical devices may lead to inefficiency due to power dissipation and increasing delay times [Davis et al., 2001].

Moore's law for semiconductor based integrated circuits is at the end [Waldrop, 2016]. To ensure further progress, which is important for better weather and climate modeling, for medical issues such as DNS encoding, for faster calculations of complex physical systems and many more, it is important to search for new solutions. From today's view it seems to be obligatory to get away from the CMOS (complementary metal-oxide-semiconductor) technology and find new ways to process data [Nikonov and Young, 2013]. One promising idea for the beyond-CMOS era is spin waves (SWs) technology. [Dutta et al., 2015; Verba et al., 2016]

1.1 Spin Waves

Spin waves are coherent excitations of the electron spins. Classically seen, it is a phase-coherent precessions of coupled, microscopic magnetization vectors of a magnetized medium, see Fig. 1.1. Its quasiparticle, the *magnon*, was predicted in 1929 by Felix Bloch, originally to describe the temperature dependence of the spontaneous magnetization in a ferromagnet [Bloch, 1930]. Later on, Holstein and Primakoff [1940] as well as Dyson [1956] developed the quantitative theory for magnons, showing that they behave as weakly interacting particles, which obey the Bose-Einstein statistics[b]. The term 'magnon' is used analogously to the quantized lattice vibration: the phonon. Sound waves are displacements of the atoms, while spin waves are displacements of the electron spins.

Experimentally, the topic of SWs is part of the research since the late 1940s [Griffiths, 1946; Kittel, 1947], when Griffiths used ferromagnetic resonance (FMR) for a uniform precession, which is a SW with wave vector $k = 0$. In the following decades an intense research, both experimentally and theoretically, brought much more knowledge about magnon properties. Starting from electronic ways of generation and the following propagation [Eshbach, 1962; Bailleul et al., 2001; Kruglyak and Hicken, 2006], through to reflection and refraction [Goedsche, 1970; Gorobets and Reshetnyak, 1998; Vashkovsky and Lock, 2006], interference [Choi et al., 2006] and diffraction [Birt et al., 2009] up to focussing and self-focussing [Bauer et al., 1997; Demidov et al., 2009a], Doppler shift [Vlaminck and Bailleul, 2008] and tunneling of

---

[b] The term *magnonics* is used to describe a wide field of magnetism connected with SWs in general and not only for the subfield of magnetism connected with quantum magnetic phenomena.

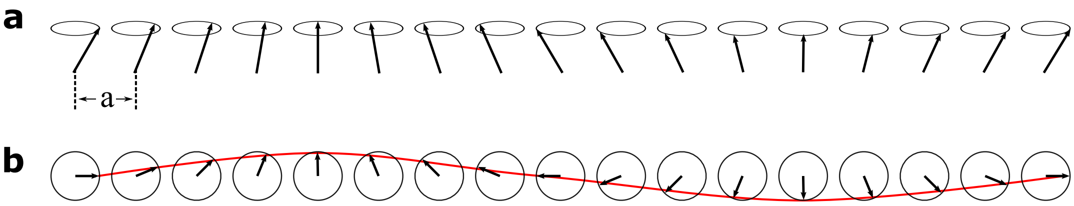

Figure 1.1: Schematical illustration of a one-dimensional string of coupled magnetic moments with precessing spins (illustrated as arrows) forming a spin wave. (**a**) Side and (**b**) top view. One full wave is shown (red line), which is going through the tips of the arrows. Graphic adapted from [Kittel, 2004]

SWs [Kozhanov et al., 2009] they exhibit in many cases a similar behavior and properties as waves of other origins. Bose-Einstein condensation of magnons in yttrium-iron garnet has been experimentally observed, even at room temperature [Demokritov et al., 2006].

In the past few years, an all magnonic transistor [Chumak et al., 2014] and different logic gates have been experimentally presented [Kostylev et al., 2005], important progress towards magnonic logic circuits [Khitun et al., 2010] as possible descendants of the conventional CMOS integrated circuit technology [Lenk et al., 2011]. Furthermore, coupling of magnons with superconducting qubits (see also Sec. 1.2) has been demonstrated [Tabuchi et al., 2015], which makes SWs an appealing technology for quantum computing challenges [Wesenberg et al., 2009].

The electron spins in a solid can be coupled with each other by two different mechanisms: first the short-distance but strong *exchange interaction* and second the relatively weak but long-range *dipolar interaction*, see also Sec. 2.1. Depending on the underlying coupling mechanisms, there are two classes of SWs. The spin excitations with relatively short wavelengths ($\lambda < 1\,\mu$m [Chumak et al., 2015]) are governed mainly by the exchange interaction and are called *exchange spin waves*, or in some text books just spin waves. For waves with a larger wavelength, the exchange interaction of the spins is negligible and, consequently, they are named dipolar or *magnetostatic waves* (MSWs) [Eshbach and Damon, 1960; Damon and Eshbach, 1961; Gurevich and Melkov, 1996; Stancil and Prabhakar, 2009]. The term 'magnetostatic' is justified not because of a non-dynamical behavior but to indicate that these waves are solutions to the Maxwell's equations for the magnetostatic approximation. The dipolar interaction of the electron spins inhere an anisotropy, and therefore, the MSWs are classified into subgroups depending on the geometry of the magnetic film plane, the magnetization $\mathbf{M}$ and the wavevector $\mathbf{k}$ to each other. For an in-plane magnetized film, two cases are distinguished: $\mathbf{k} \parallel \mathbf{M}$ and $\mathbf{k} \perp \mathbf{M}$, which are named *backward volume magnetostatic waves* (BVMSWs) and *magnetostatic surface waves* (MSSWs), respectively. For an out-of-plane magnetization the waves are *forward volume magnetostatic waves* (FVMSWs).

In general, SWs are generated when the magnetization in a magnetically ordered material is brought out of its equilibrium position. Due to the coupling of the electron spins, the perturbation is traveling across the sample in a wave pattern. Historically, magnetostatic waves have been exploited copious for microwave devices [Owens et al., 1985; Adam, 1988] as they are easily generated. It is done by stripe antennas brought in the vicinity of the sample generating microwaves, which is still the most usual way in the experimental research [Kruglyak et al., 2010; Demidov et al., 2009b]. However, SW generation by antennas has disadvantages, e.g. many setup parameters cannot be altered after fabrication of the sample with its antenna, thus shrinking the degrees of freedom for the SW dispersion. Optical excitation by laser pulses is the excitation method we used in the work of this thesis. Here, only the magnetization under the illuminated spot by the laser beam gets perturbed and SWs are launched, which enables point sources on the micron- or even submicron-scale when plasmonic nanogeometries are utilized [Uchida et al., 2015]. This contactless method of excitation allows to be shifted easily over the sample. Furthermore, changing excitation parameters, such as spatial shaping, allows to modify the SW dispersion [Satoh et al., 2012].

However, it lasted until 2002 when for the first time spin waves were generated optically by an ultrashort laser pulse [van Kampen et al., 2002]. Due to strong concentration of the energy on a short timescale of 0.1 ps and small focal point of about $10\,\mu$m, the sample is heated, which changes its anisotropy, triggering a precession of the magnetization, leading to propagating SWs. It took ten more years, thus not long ago, until the first optical non-thermal excitation of SWs was realized [Satoh et al., 2012]. Here, the authors made use of a non-thermal, non-absorptive effect: the inverse Faraday effect (IFE) [Kimel et al., 2005]. Strong, ultrashort laser pulses push the magnetization of a magnetized sample out of its equilibrium position, triggering a precession of it, by which spin waves are generated.

Concluding, the field of SWs is a hot topic in scientific research. The excitation with ultrashort optical pulses was born in this century, there are still many unknown aspects which have to be investigated, which makes it interesting for the fundamental research. For technological progress, they are of high interest, because they might be a suitable way to move away from electric currents to diminish losses from Ohmic resistances and to increase processing speeds.

1.2 Spin Coherence

One very promising descendant to the classical information processing is the *quantum computing* [DiVincenzo, 1995]. A lot of research and progress have been made in the past two decades in this field of research [Ladd et al., 2010]. The alternative to the electron charge as an information carrier is here the electron spin. While voltage and no voltage are equivalent to '1' and '0' bits, the spins could do similar. They have two different possible states: up ($|\uparrow\rangle$) and down ($|\downarrow\rangle$). Since the spin is a pure quantum mechanical phenomenon, they are called *quantum bit* or just *qubit* when it comes to information processing. In contrast to the classical bit, a qubit can not only be in either one of the the two possible states but in a superposition of both:

$$|\psi\rangle = \alpha|\downarrow\rangle + \beta|\uparrow\rangle, \tag{1.1}$$

with $|\alpha|^2 + |\beta|^2 = 1$. Thus, a system with n qubits could perform 2^n operations parallel [Stolze and Suter, 2008]. This would mean an enormous rise of the processing speed for many complex mathematical problems such as prime factorization (which is important for cryptography) or simulations of physical systems.

A propitious candidate for qubits are confined structures, e.g. quantum dots [Petta et al., 2005]. When shrinking their size to or below the de Broglie wavelength, the energy states of the electron form discrete values and the quantum dot can be considered as an artifical atom.

The greatest obstacle for quantum computing is the decoherence of the spin system. The coherence has to be at least much longer than the gate operation times are [DiVincenzo, 1995]. The *spin coherence time* T_2 is the time in which the phase between all states is preserved. For an ensemble of carrier spins with different precession frequencies due to inhomogenities, the macroscopic spin can be lost much quicker than T_2 [Yakovlev and Bayer, 2008]. The time after which the whole ensemble has lost its coherence is called *spin dephasing time* T_2^*. This dephasing time is of prime interest in the part of this thesis about the spin coherence and it can be easily calculated by resonant spin amplification (RSA) measurements [Kikkawa and Awschalom, 1998].

1.3 Scope of this Thesis

The aim of this work is to get a better view into the physics and understanding of the fundamental principles underlying the observed phenomena and to find ways of SW generation suitable for possible applications required for prospective information processing. Our chosen way is to excite SWs by the inverse Faraday effect with a train of laser pulses, i.e., with a higher repetition rate than the damping rate of the following magnetization precession. With this laser system optical spin orientation was also performed. This technique offers a view into the dephasing time of a spin ensemble. Here, we performed these measurements differently from the ordinary RSA way, where the time delay between pump and probe is set to a fixed point and the magnetic field is swept over a wide range. The main aim was to investigate if this works conveniently as well.

To answer these questions thoroughly, this thesis is divided into eight chapters. The first is this motivational part here to show the need for further progress. In Chapter 2 the theoretical background is given, which is important to understand and analyze the observed phenomena. Besides an introductory part to the topic of magnetism, it explains how the magnetization $\mathbf{M}$ of a sample can be influenced by non-thermal optical ways, and describes the subsequently launched SWs. Also it approaches the theory of semiconductor physics to understand the investigated spin dephasing time.

Chapter 3 and 4 describe the experimental part of this work. The former is about the methods used to investigate the samples, which are presented in the latter. The investigated sample are (a) dielectric, magnetic iron garnet films for the first part of the work and (b) a CdTe/CdMgTe quantum well semiconductor structure for the second part. The main setup uses a high repetition rate laser system to perform pump probe measurements, based on the *ASOPS* technique. It differs from common pump probe techniques where typically mechanical delay lines are used.

In Chapter 5 and 6 the results from the investigation on the magnetic iron garnets will be shown. First, the results from optically excited magnetization precession under resonant excitation are discussed. This means, we are measuring the magnetization dynamics within the spot illuminated by the laser beam, while in Chapter 6 we introduce a spatial shift away from the illuminated region, thus, the acquired signals origin from propagating SWs. In both chapters, the dynamics are excited resonantly by a train of laser pulses. With this resonant excitation some unique peculiarities are revealed.

Chapter 7 after all is about optical spin orientation in semiconductor structures where we are interested in spin coherence times. As with the IFE in dielectric magnetic iron garnets, a spin precession is excited by a train of optical laser pulses. But while the iron garnet samples are transparent for the wavelengths of the used laser beams, and therefore, it is a non-absorptive effect, the optical spin orientation requires absorption of the incident photons. Here, the system is also excited with a train of laser pulses, thus, the spin precession can be amplified by resonant excitation.

And last but not least, Chapter 8 gives a summary of the investigated physical phenomena and their results, and furthermore a outlook for possible prospective work and its general direction of investigation.

2 Theoretical Background

This chapter starts with a short introduction into the field of magnetism on which the experiments are based. The depth of the content of this part will be limited to the fundamentals. Based on this a non-thermal way of controlling magnetism is introduced: the inverse Faraday effect (IFE), which triggers a precession of the macroscopic magnetization $\mathbf{M}$. This will give sufficient knowledge for the first part of the experimental results (see Chapter 5). The precessional movement of $\mathbf{M}$ can launch traveling spin waves (SWs), which are theoretically described in the next section and are the essential subject of the second experimental part (see Chapter 6). Last point of the theoretical background are the fundamentals of semiconductor physics, which is relevant for the last part of this work: optical spin orientation in a CdTe quantum well (see Chapter 7).

2.1 Introduction to Magnetism

As well the inverse Faraday effect as the generation of spin waves occur only in magnetic ordered materials. The atomistic magnetic moments originate from three different principal sources: the intrinsic spin of an electron, its orbital angular momentum around the proton, and third, the influence of an external magnetic field on the orbital angular momentum and on the spin [Kittel, 2004]. Many aspects of a macroscopic magnetization can be described with classical analogs, however for a full comprehension quantum mechanics is crucial. The Bohr-van Leeuwen theorem states that if treated solely with classical physics a macroscopic medium can posses only a zero net magnetic moment [van Vleck, 1977]. Nonetheless, due to the large number of particles, macroscopic magnetism can be described by classical or semi-classical models [Stancil and Prabhakar, 2009].

2.1.1 Forms of Magnetism

Materials show different responses to an external magnetic field, depending on their magnetic properties, and can be classified into different groups, see Fig. 2.1. To compare the magnetic properties in an appropriate way, one can define a volume *magnetic susceptibility* χ as following:

$$\mathbf{M} = \chi \mathbf{H} \tag{2.1}$$

with $\mathbf{M}$ for the net macroscopic magnetization of the material and $\mathbf{H}$ for the applied magnetic field strength [O'Handley, 2000]. For isotropic materials, where the induced magnetization is either parallel or antiparallel to the externally applied magnetic field, the susceptibility χ is a scalar, but in the most general form it is a 3×3 tensor.

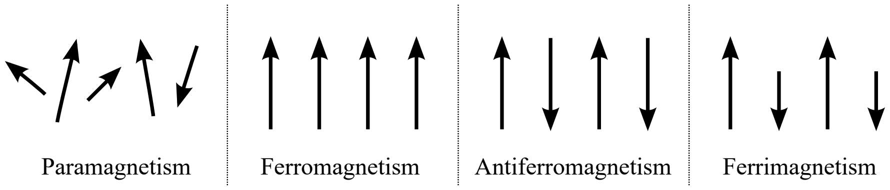

Figure 2.1: Schematic illustration of para-, ferro-, antiferro-, and ferrimagnetism. The arrows represent the magnetic moments of the atoms.

In general, all materials can be classified into two groups. Those which contain atoms or ions with permanent magnetic moments, and those which do not. Materials of the latter group are called *diamagnetic*. Inside of an external magnetic field, the electronic orbital motions are, according to Lenz's law, changed in a way, that an opposing magnetic field is generated, causing a repulsive force. When changing the magnetic field, e.g. by moving the diamagnetic material closer to it, the material is repelled by the magnetic field.

Materials containing permanent magnetic but uncoupled moments are called *paramagnetic*. Inside of a magnetic field, their magnetic moments align along it, thus reinforcing the field strength, but in absence of it they orientate randomly and, therefore, averaging to a zero net magnetization.

In a *ferromagnetic* material, the magnetic moments align spontaneously parallel to each other, giving rise to a net magnetization even without an external magnetic field. Above a specific temperature point, the *Curie temperature*, every ferromagnet loses its ferromagnetic property. In absence of an external magnetic field the magnetic order of ferromagnets breaks up into a pattern of magnetic *domains*. Inside of a domain all magnetic moments align parallel to each other, but at their boundaries, which are called *domain walls*, they change their direction in a way to minimize the net magnetization of the macroscopic sample. When exposed to an external magnetic field, the domains align along it giving rise to a net macroscopic magnetization $\mathbf{M}$, until all of them are parallel and the saturation magnetization M_s is reached.

In some materials, neighboring magnetic moments align in opposite directions, as if there are two (in the most simple instance) opposing ferromagnetic sublattices. If the magnetic moments of the two sublattices are equal, they average out and exhibit no net macroscopic magnetization, which is called *antiferromagnetic*. If the magnetic moments are unequal, a spontaneous magnetization remains like in a ferromagnet. This property is called *ferrimagnetic*. Magnetic garnets, as the main part of investigation in this thesis, are ferrimagnetic materials.

2.1.2 Exchange Interaction

The exchange interaction occurs between two identical particles and is responsible for ferromagnetism, discovered independently by [Heisenberg, 1926] and [Dirac, 1926]. The energy of interaction between two spins is described by an effective Hamiltonian, which depends only on the relative spin orientation $\mathbf{S}_1 \cdot \mathbf{S}_2$, where the $\mathbf{S}_i$ are the quantum mechanical spin operators. This is called the *Heisenberg Hamiltonian*:

$$\mathcal{H} = -2\frac{\mathcal{J}}{\hbar^2}\mathbf{S}_1 \cdot \mathbf{S}_2, \tag{2.2}$$

with $\mathcal{J}$ as the exchange constant.

To calculate the energy of any spin configuration, one can start with the simplest system of molecular hydrogen. The Hamiltonian $\mathcal{H}$ of the system can be obtained by summarizing the total energy of the system, consisting of parts for the electron kinetic energy, the potential energy between opposite charges and the repulsive force between the both electrons and both protons, respectively. Using perturbation theory, symmetric and antisymmetric wave functions $\psi_\pm$ for the two-particle system can be constructed.

Afterwards, the electron spin has to be included. Since electrons are spin-half particles, and therefore fermions, they obey the Pauli exclusion principle [Pauli, 1925] which means that no two fermions can occupy the same quantum state simultaneously. Hence, the complete wave function for the two-particle system must be antisymmetric. To obtain an overall antisymmetric wave function, a symmetric spin function χ_S is assigned to the antisymmetric ψ_- and vice versa. The first situation represents a singlet state with total spin $S = 0$ and energy $\mathcal{E}_s$, the second a triplet state with total spin $S = 1$ and energy $\mathcal{E}_t$.

From there, the exchange integral $\mathcal{J}^{\text{ex}}$ can be defined by:

$$\mathcal{J}^{\text{ex}} = \frac{1}{2}(\mathcal{E}_S - \mathcal{E}_T). \tag{2.3}$$

If $\mathcal{J}$ is positive, then $\mathcal{E}_S > \mathcal{E}_T$ and the triplet state with $S = 1$ is energetically favorable, which means electrons align their spins parallel, causing ferromagnetism in materials. For negative $\mathcal{J}$, the singlet state is favored, causing the electrons to align their spins antiparallel which can lead to antiferromagnetism.

For a solid, the generalized Hamiltonian is the sum over all pairs of electrons (i, j) in the many-electron system:

$$\mathcal{H} = -\frac{1}{\hbar^2}\sum_{i,j}\mathcal{J}_{ij}^{\text{ex}}\mathbf{S}_i \cdot \mathbf{S}_j, \tag{2.4}$$

where the factor 2 from Eq. 2.2 is included in the double counting when performing the sum. The absolute value of $\mathcal{J}$ depends strongly on the overlap of the wave function from electrons i and j, thus, it is decreasing very quickly for growing distances. This very short-ranged interaction is confined to electrons from the same atom (*intra-atomic exchange*) or nearest neighbors (*direct exchange*). Via intermediate atoms a longer-ranged interaction is possible, which is called *superexchange* (see also Section 4.1.2).

Due to this short-ranged interaction, the sum of Eq. (2.4) can be reduced to the interaction of the nearest neighbors $\langle i, j \rangle$:

$$\mathcal{H} = -\frac{\mathcal{J}}{\hbar^2} \sum_{\langle i,j \rangle} \mathbf{S}_i \cdot \mathbf{S}_j. \tag{2.5}$$

The exchange interaction is the responsible mechanism for ferromagnetism. Remarkably, the causes for this interaction are purely quantum mechanical and actually not of magnetic nature. Primarily it results from the electric repulsion and the Pauli exclusion principle. The direct magnetic interaction between two electrons is negligibly small, but important for other phenomena, see the next section.

2.1.3 Dipolar Interaction

The exchange interaction from the previous section is the strongest form of interaction between atoms in ferromagnets but decreases very quickly for growing distances, and is therefore a short-range interaction. The magnetic dipole-dipole interaction arises from the interaction between the intrinsic magnetic dipole moments μ of the atoms. The energy of two dipoles μ_1 and μ_2 separated by $\mathbf{r}$ is [Getzlaff, 2007]

$$E = \frac{\mu_0}{4\pi r^3} \left[\boldsymbol{\mu}_1 \cdot \boldsymbol{\mu}_2 - \frac{3}{r^2} (\boldsymbol{\mu}_1 \cdot \mathbf{r})(\boldsymbol{\mu}_2 \cdot \mathbf{r}) \right], \tag{2.6}$$

with μ_0 for the vacuum permeability. Thus, the energy depends not only on the distance of the dipoles, but also on their relative orientations. To get a rough idea of the order of magnitude of this energy, we choose $\mu_1 = \mu_2 = 1\mu_B$ and $r = 1\,\mathring{A}$ as typical values. This results in an estimation of the energy of

$$E \approx 10^{-23} J. \tag{2.7}$$

With $E = k_B T$ this corresponds to an energy of around 1 K which would be the Curie temperature, where a ferromagnetic material loses its ferromagnetic properties and becomes paramagnetic. This is in many cases several hundreds of Kelvin below the actual Curie temperature. Hence, ferromagnetic behavior does not originate from the magnetic dipolar interaction but from the exchange interaction. However, the dipolar interaction plays an important role for other phenomena such as anisotropy energies, since the equations for the exchange energy do not depend on the direction of $\mathbf{M}$. Furthermore and very important for the work of this thesis, it contributes to long-range interactions like spin waves with long wavelengths or magnetic domains.

2.1.4 Magnetocrystalline Anisotropy

A ferromagnetic material is considered to be magnetically anisotropic if it is energetic favorable to magnetize it in a certain direction compared to others. There exist many other types of anisotropy such as shape, exchange or induced anisotropy, but the magnetocrystalline anisotropy is much stronger and has a perceptible influence on magnetic properties of many materials [du Tremolet de Lacheisserie et al., 2005]. This is caused by spin-orbit coupling or by dipolar interaction of the spins. Since the magnetic moments form a lattice, the internal energy U_M of the system has a contribution which depends on their orientation with respect to the crystal axes, the *anisotropic energy* [Gurevich and Melkov, 1996].

The first type of anisotropy is the uniaxial anisotropy and is present in crystals with one single symmetry axis, which corresponds either to maximum or minimum energy and is then the so called *hard axis* or *easy axis*, respectively. The anisotropic energy can be expressed as a expansion series in powers of the direction cosines. The magnetization vector is written as $\mathbf{M} = M_s(\alpha_1, \alpha_2, \alpha_3)$, with M_s for the saturation magnetization. By changing to spherical coordinates $\alpha_1 = \cos\varphi \sin\theta$, $\alpha_2 = sin\varphi \sin\theta$ and $\alpha_3 = \cos\theta$ and defining the z axis as the main crystal axis, one can express the lowest order of anisotropic energy density as:

$$W_{\text{ua}} = K_u \sin^2\theta, \tag{2.8}$$

where K_u is the uniaxial anisotropy constant [Stancil and Prabhakar, 2009]. Depending on the sign of the constant either the easy axis ($K_u > 0$) or the hard axis ($K_u < 0$) is directed along the symmetry axis. In the latter case, there is an *easy plane* perpendicular to $\pm z$.

Crystals of cubic symmetry exhibit cubic anisotropy, its origin was first discussed by van Vleck [1937] using perturbation theory for a quantitative description. The energy density up to the sixth order[a] can be written as [Garcia-Otero et al., 1999]

$$W_{\text{ua}} = K_1(\alpha_2^2\alpha_3^2 + \alpha_3^2\alpha_1^2 + \alpha_1^2\alpha_2^2) + K_2\alpha_1^2\alpha_2^2\alpha_3^2, \tag{2.9}$$

with the cubic anisotropy constants K_1 and K_2.

2.2 Non-Thermal Control of Magnetism

After giving the very fundamentals of magnetism, we can now come to the dynamics in magnetism. First, we start with the non-thermal control of magnetism. For our experiments we exploit the inverse Faraday effect, which was introduced into physical research in the 60s of the last century [Pitaevskii, 1961; van der Ziel et al., 1965; Pershan et al., 1966]. About one decade ago, Kimel et al. [2005] found out that circularly polarized strong femtosecond laser pulses can be used to perturb the magnetization in a non-thermal way.

---

[a] Terms of higher orders are not necessary to describe experimentally observed phenomena.

2.2.1 Inverse Faraday Effect (IFE)

How can light influence the magnetization of a medium in a non-thermal way? The other way round, light being influenced in its polarization by a magnetized medium is manifested in various well known magneto-optical phenomena. For example the Faraday effect where the plane of polarization of linearly polarized light is rotated after transmission through a magnetized medium (see also Sec. 3.1.2). The angle of rotation in this case is [Kimel et al., 2005]

$$\phi_{\mathrm{FR}} = \frac{\chi}{n}\mathbf{M}\cdot\mathbf{k}, \tag{2.10}$$

where χ is the magneto-optical susceptibility, n the refractive index, $\mathbf{M}$ the magnetization in the medium and $\mathbf{k}$ the wave vector of the propagating light.

Much less known, though quite promising, are the inverse effects, where propagating light can deflect a magnetization inside of a medium, which is in this thesis namely the inverse Faraday effect (IFE)[b].

Phenomenological Derivation

An analytical expression for the IFE can be derived phenomenologically [Pershan, 1963; van der Ziel et al., 1965]. In a thermodynamical equilibrium one can use the free energy F as the thermodynamical potential and find a derivation of the magnetization $\mathbf{M} = \partial F/\partial\mathbf{H}$, where $\mathbf{H}$ is the external magnetic field. From this follows the static ($\omega = 0$) magnetization induced by a propagating light wave [Kimel et al., 2005]

$$\mathbf{M}(0) = \frac{\chi}{16\pi}[\mathbf{E}(\omega)\times\mathbf{E}^*(\omega)], \tag{2.11}$$

where $\mathbf{E}(\omega)$ is the electric field of the light wave at the frequency ω. It follows, that circularly polarized light induces a magnetization $\mathbf{M}(0)$ along the propagation axis k, with opposite sign when switching the helicity. Furthermore, for linearly polarized light no magnetization is induced: $\mathbf{M}(0) = 0$.

The assumptions leading to Eq. 2.11 are only valid if the timescales of excitation are long compared to the thermal relaxation times which is not justified when using femtosecond laser pulses. Here, the cross product in Eq. 2.11 is changing much faster than the typical timescales of phonon-magnon and magnon-magnon interaction [Kimel et al., 2007]. Instead, one should focus on the Hamiltonian itself, instead of thermal averages, and introduce an 'effective Hamiltonian' $\mathcal{H}_{\mathrm{eff}}$ which is optically induced. Calculations show that the cross product $[\mathbf{E}(\omega)\times\mathbf{E}^*(\omega)]$ acts as if it induces an additional magnetic field along the propagation axis [Pershan et al., 1966], quantiative theoretical discussion of the effective Hamiltonian can be found in the paper of Popova et al. [2012].

---

[b] Other inverse effects are also known, like the inverse Kerr effect [Belotelov and Zvezdin, 2012] or the inverse Cotton-Mouton effect [Kalashnikova et al., 2007].

In both Eq. (2.10) and Eq. (2.11) the same magneto-optical susceptibility χ determines the phenomena. Consequently, the inverse Faraday effect should be most efficient in materials at wavelengths where they exhibit a high Faraday rotation signal per unit magnetization. In addition, χ does not depend on any symmetry properties, and therefore, the effect is unattached to any crystallographic or magnetic structures.

Microscopic Explanation

The inverse Faraday effect is excited by laser light whose wavelength is in the transparency region of the studied iron garnet samples, thus, the effect is a non-resonant, dispersive effect. The energy of the photons is too weak for a direct excitation of the spin system. Instead, it is assumed that an impulsive stimulated Raman scattering (ISRS) is causing the spin-flip process [Shen and Bloembergen, 1966], see Fig. 2.2. Two photons with the frequencies ω_1 and ω_2, which are present in the broad laser spectrum, are involved in this process. The first one excites the atom from the ground state $|g\rangle$ into a virtual state, which is a superposition of ground and excited state $|e\rangle$. Then, a second photon with the energy $\hbar\omega_2 = \hbar(\omega_1 - \Omega_M)$ coherently stimulates a relaxation back to the ground state with reversed spin under emission of a magnon with energy $\hbar\Omega_M$, equal to the energy difference between the two ground states.

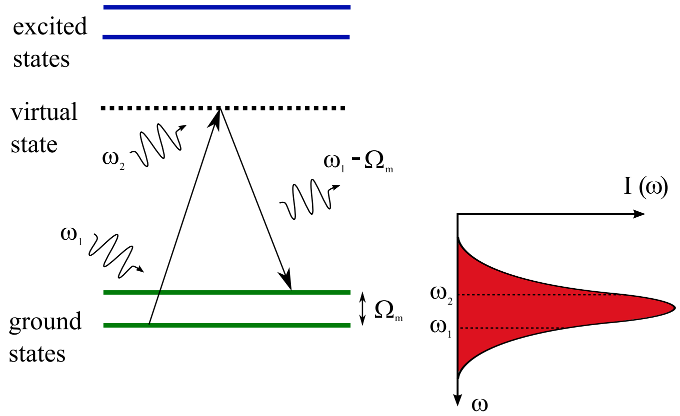

Figure 2.2: Schematic illustration of the impulsive stimulated Raman scattering which is suggested to be responsible for the electron spin flip. One photon with a frequency ω_1 from the spectrally broad laser pulse excites the electron into a virtual state with strong spin-orbit coupling. A second photon with the frequency ω_2 stimulates the relaxation back with a flipped electron spin, creating a magnon with frequency Ω_m.

In the presence of the off-resonant laser light radiation virtual absorptions and re-emissions of the incident photons result in a energy displacement $\hbar\Delta'$ of the atomic energy levels, which is known as the AC Stark shift [Delone and Krainov, 1999] and is caused by the influence

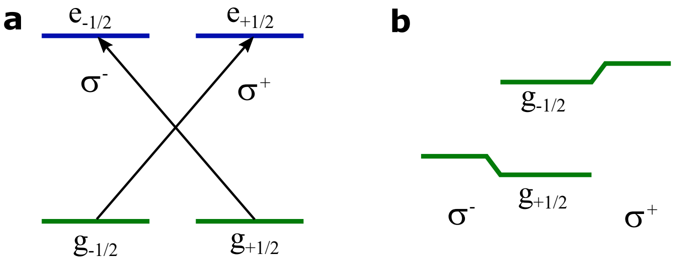

Figure 2.3: Schematic illustration of the light shift (a) for a $J_g = 1/2 \leftrightarrow J_e = 1/2$ transition. (b) σ^+ polarized light shifts only the $g_{-1/2}$ sublevel, whereas for σ^- polarized light only the $g_{+1/2}$ sublevel is shifted. Graphic adapted from [Cohen-Tannoudji, 1998].

of the altering electric field component of the incident light beam on the electrons of the atoms. The shift is given by [Cohen-Tannoudji, 1998]:

$$\Delta' = \Omega^2 \frac{\delta}{\Gamma^2 + 4\delta^2}, \tag{2.12}$$

where Ω is the Rabi frequency proportional to $\sqrt{N}$ (number of photons), $\delta = \omega_L - \omega_A$ the detuning between light frequency ω_L and atomic frequency ω_A, and Γ the natural width of the atomic excited state. Obviously, Δ is linearly proportional to N, i.e., the light intensity. Due to selection rules and angular momentum conversion, the light shift depends on the helicity of the exciting circularly polarized photons. In Fig. 2.3a a schematic illustration for a $J_g = 1/2 \leftrightarrow J_e = 1/2$ transition is shown. Right-handed polarized light shifts only the Zeeman sublevel with $m_g = -1/2$, and left-handed polarized light the sublevel with $m_g = +1/2$, see Fig. 2.3b. During the presence of the laser radiation the ground state energy levels are shifted, depending on the laser polarization. This acts on the spin system as if there is an additional magnetic field along the light propagation axis $\mathbf{k}$, changing the $\pm$-direction with the helicity.

2.2.2 Precession of Magnetization

Before the arrival of the femtosecond laser pulse the magnetization $\mathbf{M}$ of the sample is directed along an effective magnetic field $\mathbf{H}_{\text{eff}}$, which is the variational derivation of the free energy W: $\mathbf{H}_{\text{eff}} = -\partial W/\partial\mathbf{M}$. This energy has contributions from different origins, in our case: $W = W_Z + W_d + W_a + W_F$, where W_Z is the Zeeman energy in the externally applied magnetic field $\mathbf{H}$, W_d and W_a are demagnetization and magnetic anisotropy energies, respectively, and the last term comes from the inverse Faraday effect $W_F = -\mathbf{M}\cdot\mathbf{H}_F$, which is unequal to zero only during the presence of the laser pulse.

After illumination with the circularly polarized laser pulse, acting as if it was inducing an additional magnetic field $\mathbf{H}_F$ along the propagation axis, the magnetization $\mathbf{M}$ is brought out of its equilibrium position, which leads to a spatial and temporal pattern of it: $\mathbf{M} = \mathbf{M}(\mathbf{r}, t)$. When no longer parallel to $\mathbf{H}_{\text{eff}}$, a torque τ is acting on the magnetic moments $\boldsymbol{\mu}$:

$$\boldsymbol{\tau} = \boldsymbol{\mu} \times \mathbf{H}_{\text{eff}}. \tag{2.13}$$

The torque is equal to the first derivative in time of the kinetic momentum $\boldsymbol{\tau} = d\mathbf{J}/dt$. The constant of proportionality between the magnetic moment $\boldsymbol{\mu}$ and the angular momentum $\mathbf{J}$ is called *gyromagnetic ratio* γ: $\boldsymbol{\mu} = \gamma \mathbf{J}$. Now we can rewrite Eq. 2.13 to:

$$\frac{d\mathbf{J}}{dt} = \gamma \mathbf{J} \times \mathbf{H}_{\text{eff}}. \tag{2.14}$$

This is the equation of motion for one single electron. For a macroscopic media one can replace the magnetic moment $\boldsymbol{\mu}$ of a single electron by the macroscopic magnetization $\mathbf{M}$ by multiplying both sides of Eq. 2.14 with γN and noting that $\mathbf{M} = \gamma N \mathbf{J}$, leading to

$$\frac{d\mathbf{M}}{dt} = \gamma \mathbf{M} \times \mathbf{H}_{\text{eff}} \tag{2.15}$$

which is known as the lossless Landau-Lifshitz equation [Landau and Lifshitz, 1935]. This differential equation describes the dynamics of the magnetization $\mathbf{M}$ after being brought out of its equilibrium position. It predicts a precession of $\mathbf{M}$ around the effective magnetic field $\mathbf{H}_{\text{eff}}$, but the angle θ between these would remain the same. This nonphysical infinite precession is due to not taking into account the magnetic damping in this model. To solve this problem, a loss can be introduced phenomenologically by adding a component of $d\mathbf{M}/dt$ in $-\theta$ direction. One possible way was suggested by Gilbert [Gilbert, 1955]

$$\frac{d\mathbf{M}}{dt} = \gamma \mathbf{M} \times \mathbf{H}_{\text{eff}} + \frac{\alpha}{M} \mathbf{M} \times \frac{d\mathbf{M}}{dt} \tag{2.16}$$

with α as the Gilbert damping constant and $M = |\mathbf{M}|$ as the magnitude of the magnetization. The solution of this equation is a precessional movement of $\mathbf{M}$ following a spiral back to the equilibrium position. Furthermore, from Eq. 2.16 one can directly see that $\mathbf{M}$ is in equilibrium when aligned parallel to $\mathbf{H}_{\text{eff}}$ ($\mathrm{d}\mathbf{M}/\mathrm{dt} = 0$).

Combining the results from this section and the one before shows that the illumination of a magnetically ordered material with circularly polarized femtosecond laser pulses triggers a damped precession of the magnetization $\mathbf{M}$ around its equilibrium position. A graphical step by step illustration of this process can be seen in Fig. 2.4.

2.3 Spin Waves

This section will give an overview of the theory of spin waves propagation. As already mentioned in Sec. 1.1, SWs are propagating distortions of the electron spins. As shown in the previous section, illuminating a magnetized sample by ultrashort laser pulses can induce

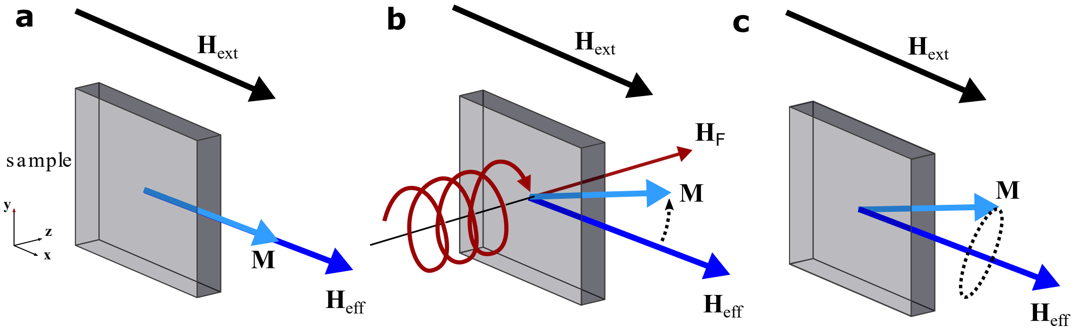

Figure 2.4: Graphical illustration of the magnetic precession. (**a**) The initial state before the arrival of the laser pulse. The magnetization **M** of the sample is directed parallel to $\mathbf{H}_{\text{eff}}$. (**b**) Circularly polarized light is inducing the inverse Faraday effect, acting as if an additional magnetic field $\mathbf{H}_F$ is applied along the propagation direction k, so that **M** is brought out of its equilibrium position. (**c**) **M** starts to precess around $\mathbf{H}_{\text{eff}}$.

the IFE, exciting the spins under the illuminated spot and triggering a precession of the magnetization. Due to the coupling of the spins in magnetically ordered materials, this spin precession is spreading away, leading to traveling SWs. Depending on the underlying coupling of the spins, two different kind of waves are excited. For SWs with a large wavelength (typically if more than $1\,\mu$m), exchange interaction can be neglected and only the dipolar interaction is important. For these cases, the magnetostatic approximation leads to the so called Walker's equation, giving a band of frequencies within which the excited SW frequency lies. When applying additional boundary conditions due to finite film thickness, we can distinguish between three different classes of dipolar spin waves.

2.3.1 Magnetostatic Approximation

For magnetostatic waves (MSWs), also known as dipolar waves, the wavelength λ_{MSW} of the wave in the medium is much smaller than of the corresponding electromagnetic wave with the same frequency ω, i.e. $\lambda_{\text{MSW}} \ll \lambda_{\text{light}} = 2\pi c/\omega$, with c for the vacuum speed of light. This is called the quasistatic approximation.

Let us first divide the quantities H, B and E for magnetic field intensity, magnetic flux density and electric field intensity, respectively, into constant and time-dependent components:

$$\mathbf{H} = \mathbf{H}_0 + \mathbf{h}(\mathbf{r}, t), \tag{2.17}$$

$$\mathbf{B} = \mathbf{B}_0 + \mathbf{b}(\mathbf{r}, t), \tag{2.18}$$

$$\mathbf{E} = \mathbf{E}_0 + \mathbf{e}(\mathbf{r}, t), \tag{2.19}$$

where $\mathbf{h}(\mathbf{r},t) = \mathbf{h}(\mathbf{r})e^{i\omega t}$, $\mathbf{b}(\mathbf{r},t) = \mathbf{b}(\mathbf{r})e^{i\omega t}$ and $\mathbf{e}(\mathbf{r},t) = \mathbf{e}(\mathbf{r})e^{i\omega t}$. Here, the time-dependent part is much smaller than the constant: $h(\mathbf{r}) \ll H_0$, $b(\mathbf{r}) \ll B_0$ and $e(\mathbf{r}) \ll E_0$. The Maxwell's equation for the magneto-quasi-statics are then: [Stancil and Prabhakar, 2009]

$$\nabla \times \mathbf{h} = 0, \tag{2.20}$$

$$\nabla \cdot \mathbf{b} = 0, \tag{2.21}$$

$$\nabla \times \mathbf{e} = i\omega \mathbf{b}. \tag{2.22}$$

The time-dependent components of the magnetic field intensity and flux density are connected by:

$$b = \overline{\mu} \cdot h, \tag{2.23}$$

with $\overline{\mu} = \mu_0(\mathbb{1} + \overline{\chi})$ for the permeability tensor.

Eq. (2.20) justifies to introduce a magnetostatic scalar potential:

$$h = -\nabla\psi, \tag{2.24}$$

which leads in combination with Eq. (2.21) and (2.23) to [Kabos and Stalmachov, 1994]:

$$\frac{\partial^2\psi}{\partial x^2} + (1+\chi)\left(\frac{\partial^2\psi}{\partial y^2} + \frac{\partial^2\psi}{\partial z^2}\right) = 0, \tag{2.25}$$

(the magnetic field is set along the x axis), which is known as the Walker's equation [Walker, 1957] and since it is solely based on magnetostatic equations (Eqs. (2.20) and (2.21)), its solutions are usually referred to as *magnetostatic modes*. Although, one has to keep in mind that the solutions are not completely magnetostatic because time variations with microwave frequencies are assumed. [Stancil and Prabhakar, 2009]

Let us first consider a uniform plane wave $\psi = \psi_0 \exp(-i\mathbf{kr})$ propagating in an infinitely large ferromagnetic medium. Thus, we do not have to consider boundary conditions. Eq. (2.25) then becomes:

$$k_x^2 + (1+\chi)(k_y^2 + k_z^2) = 0. \tag{2.26}$$

For propagation under the angle θ with respect to the x axis:

$$k_x^2 = k^2 \cos^2\theta, \tag{2.27}$$

$$k_y^2 + k_z^2 = k^2 \sin^2\theta, \tag{2.28}$$

which gives

$$\chi \sin^2\theta = -1. \tag{2.29}$$

χ can be expressed in terms of frequency ω by [Stancil and Prabhakar, 2009]

$$\chi = \frac{\omega_0 \omega_M}{\omega_0^2 + \omega^2} \tag{2.30}$$

which yields to:

$$\omega^2 = \omega_0(\omega_0 + \omega_M \sin^2 \theta), \tag{2.31}$$

with $\omega_0 = -\gamma\mu_0 H_0$ and $\omega_M = -\gamma\mu_0 M_s$. Apparently, the value for the frequency is independent of k. The calculated frequencies from Eq. (2.31) are the asymptotes for large k for waves propagating parallel or perpendicular to the applied bias magnetic field, when $\theta = 0$ or $\theta = \pi/2$, respectively. For the former case, Eq. (2.31) becomes the precession frequency of the ferromagnetic resonance (FMR), also known as the Kittel formula [Kittel, 2004], which is a special case of a standing spin wave with wavevector $k = 0$. The frequency degeneracy is removed either by considering effects of the boundaries of finite samples or the exchange interaction.

Eq. (2.31) gives a band of frequencies with a lower and upper limit for propagating spin waves in ferrites:

$$\omega_0 < \omega < \sqrt{\omega_0(\omega_0 + \omega_M)} \tag{2.32}$$

2.3.2 Thin Films

When excited in thin films, three different classes of MSWs are distinguished which are determined by the orientation of the applied magnetic field relative to the SW propagation direction and surface plane of the sample film [Serga et al., 2010]. The classical work of calculating the different dispersion relations was performed in the Sixties of the last century [Eshbach and Damon, 1960; Damon and Eshbach, 1961; Damon and Vaart, 1965], good textbooks about MSWs in finite films are written by Kabos and Stalmachov [1994]; Gurevich and Melkov [1996]; Stancil and Prabhakar [2009], the latter as the main source for this section. An overview of the three different geometries is shown in Fig. 2.5, for the explanation see the following three paragraphs.

Forward Volume Waves

This kind of MSWs is present in a normally magnetized film, so $H_{\text{ext}} \parallel \mathbf{n}$, where $\mathbf{n}$ is normal to the surface plane, while the SW is propagating in the film plane, thus, $\mathbf{k} \perp H_{\text{ext}}$, see Fig. 2.5a. For the derivation of the solutions, one has to use the Walker's equation (Eq. (2.25)) for inside of the film and the Laplace equation for outside ($\chi = 0$) and then consider boundary conditions for the time-dependent parts in Eqs. (2.17)–(2.19). Several solutions

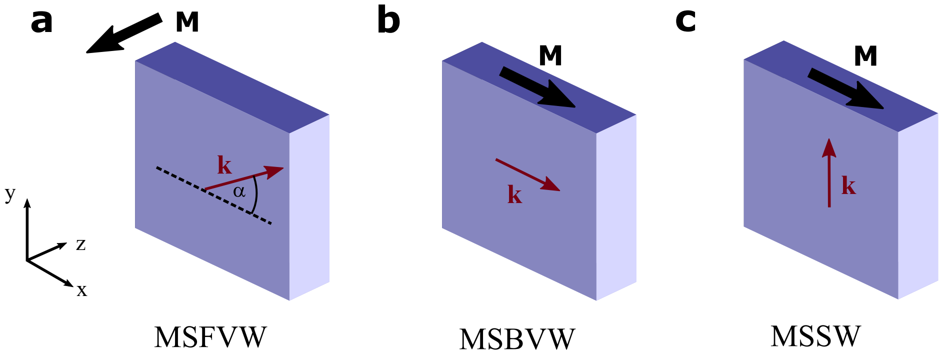

Figure 2.5: Different geometries for magnetostatic waves in a ferrite film. (a) Normally magnetized ferrite film with in-plane $\mathbf{k}_t = \mathbf{k}_x + \mathbf{k}_y$ (any arbitrary angle α), (b) tangentially magnetized film with $\mathbf{k} \parallel \mathbf{M}$ and (c) $\mathbf{k} \perp \mathbf{M}$. MSFVW: magnetostatic forward volume wave, MSBVW: magnetostatic backward volume wave, MSS: magnetostatic surface wave.

can be found for different modes in this geometry, an approximation which is explicitly solvable for ω for the lowest order is [Kalinikos, 1980]

$$\omega^2 = \omega_0 \left[\omega_0 + \omega_M \left(1 - \frac{1 - e^{-k_t d}}{k_t d} \right) \right], \tag{2.33}$$

where k_t is the tangential wave vector component and d the sample thickness. For infinite thick samples Eq. (2.33) becomes the upper limit of Eq. (2.32).

Group and phase velocity, $v_p = \omega/k$ and $v_g = \partial\omega/\partial k$, respectively, have different magnitudes but are both in the same direction, which means they are *forward waves*, while the wave amplitude is sinusoidally distributed through the *volume* of the film. These two points, combined with the magnetostatic approximation for finding solutions, justifies why these modes are called *magnetostatic forward volume waves* (MSFVWs).

Backward Volume Waves

For the former case with a normally magnetized film, the wave propagation was isotropic and independent of the direction in the film plane (as long as we neglect magnetocrystalline anisotropy). For the case of a tangentially magnetized film this symmetry is no longer given and the dispersion of the MSWs depends on the geometry of $\mathbf{k}$ relative to $\mathbf{H}_{\text{ext}}$. Let us first consider the case for $\mathbf{k} \parallel \mathbf{H}_{\text{ext}}$ (see Fig. 2.5b). For the boundary conditions, first, we require the wave function ψ to be continuous at the surface of the sample, and second, that the normal component of $\mathbf{b}(t)$ is continuous. With the Walker's equation (2.25) we get an equation connecting k_x with k_z:

$$k_x^2 + (1 + \chi) k_z^2 = 0 \tag{2.34}$$

which, if we require k_x and k_z to be real, can only be solved if $(1+\chi) < 0$. Further calculations give us transcendental equations connecting the wave vector k with the frequency ω. For modes with an odd potential function it is:

$$\tan\left(\frac{k_x d}{2\sqrt{-(1+\chi)}}\right) = \sqrt{-(1+\chi)}, \tag{2.35}$$

where k_x is the k-vector component along the magnetic field, and for even potentials:

$$-\cot\left(\frac{k_x d}{2\sqrt{-(1+\chi)}}\right) = \sqrt{-(1+\chi)}. \tag{2.36}$$

χ can again be expressed in terms of ω, see Eq. (2.30).

With the identity $\tan(\theta - \pi/2) = -\cot\theta$ we can now combine both dispersion relations, even and odd, into one single equation:

$$\tan\left(\frac{k_x d}{2\sqrt{-(1+\chi)}} - \frac{(n-1)\pi}{2}\right) = \sqrt{-(1+\chi)}, \qquad n \text{ is integer}, \tag{2.37}$$

whose solutions can be found graphically. An approximation of Eq. (2.37) for the lowest order ($n = 1$) is: [Kalinikos, 1980]

$$\omega^2 = \omega_0 \left[\omega_0 + \omega_M \left(\frac{1 - e^{-k_x d}}{k_x d}\right)\right]. \tag{2.38}$$

The dispersion relation for the lowest order is calculated by Eq. (2.38) and shown in Fig. 2.6 for ω/ω_M against $k_x d$. The dashed lines give the upper and lower limits from the frequency band of Eq. (2.32). For $k_x = 0$ the wave is not propagating along the applied bias field and the frequency is equal to the FMR frequency (upper limit, $\theta = \pi/2$). The lower limit is approached in the limit of large k_x ($\theta = 0$).

The phase velocity $v_p = \omega/k_x$ of each mode at a given point $(\omega_1, k_{x,1})$ is positive, while the group velocity is determined by the slope $v_g = \partial\omega/\partial k_x$ and is negative. Thus, both velocities point in opposite directions. This is why waves in this geometry are called *backward wave*. As with forward volume waves, the wave amplitude is also distributed sinusoidally throughout the sample, thus, these waves are called *magnetostatic backward volume waves* (MSBVWs).

Surface Waves

The last class of magnetostatic waves is for the remaining geometry where the sample is again tangentially magnetized but the propagation direction of the waves is perpendicular to the applied magnetic field: $\mathbf{k} \perp \mathbf{H}_{\text{ext}}$ (see Fig. 2.5c), thus $k_x = 0$. We use

$$\psi_{\text{film}} = \psi_0 \cos(k_z z) e^{i\nu k_y y} \tag{2.39}$$

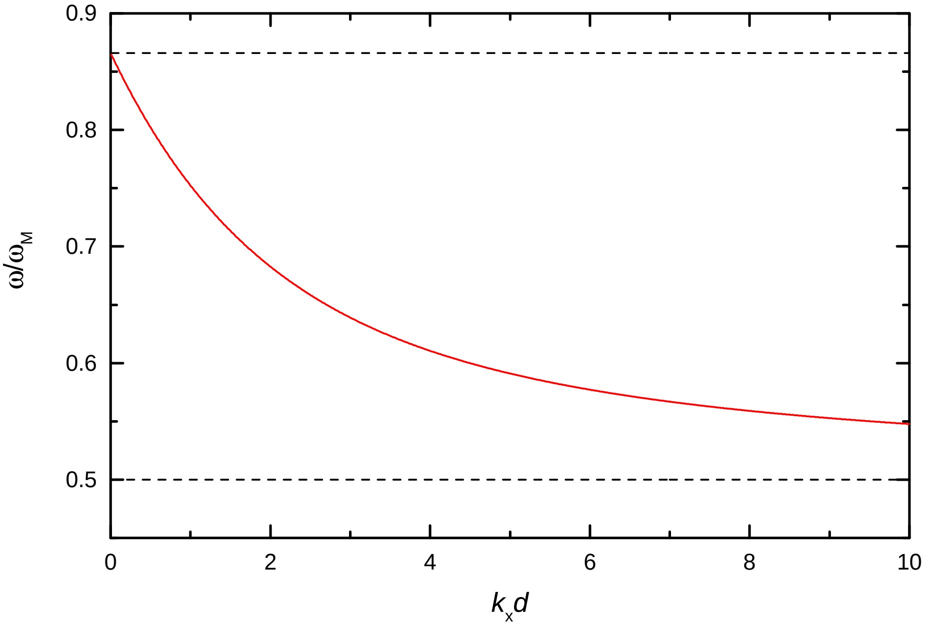

Figure 2.6: Dispersion relation of backward volume waves of lowest order ($n = 1$), calculated by Eq. (2.38) with $\omega_0/\omega_M = 0.5$. The dashed lines give upper and lower limits for the frequency (see Eq. (2.32)).

as a trial solution for the potential function inside of the ferrite film, where the constant ψ_0 gives the mode amplitude and $\nu = \pm 1$. Then, the Walker's equation (2.25) connects k_y and k_z inside of the ferrite by

$$(1 + \chi)(k_y^2 + k_z^2) = 0. \tag{2.40}$$

One possible solution would be $\chi = -1$, but this gives only one specific frequency value and not a band of solutions as we had in the cases before. Instead, we require $k_z^2 = -k_y^2$ and, if we additionally require k_y to be real to obtain propagating waves, then k_z is imaginary, and thus, ψ_{film} is not oscillatory in z direction but consists of growing and decaying exponentials:

$$\psi_{\text{film}} = \left(\psi_{0+}e^{kz} + \psi_{0-}e^{-kz}\right) e^{i\nu ky}, \tag{2.41}$$

with $k \equiv k_y = |k_z|$.

If we express equations for the potential functions inside of the ferrite for the other two cases, the Walker's equation and boundary conditions give real wavenumbers, and therefore, the oscillatory signal in z direction remains, which is the reason why these are called volume modes. Due to the exponentially decaying signal in Eq. (2.41) the amplitude distribution is largest at the surface of the film and decays for an increasing depth. This is why these modes are called *magnetostatic surface waves* (MSSWs).

The dispersion relation of these waves is:

$$\omega^2 = \omega_0(\omega_0 + \omega_M) + \frac{\omega_M^2}{4}\left(1 - e^{-2kd}\right). \tag{2.42}$$

It can be strongly influenced by bringing a metallic layer on the ferrite film, especially if this is done on only one of both sides [Kabos and Stalmachov, 1994].

2.4 Semiconductor Physics

For the second part of this work we studied a non-magnetic semiconductor structure. The underlying physical phenomena differ considerably from the magnetization precession in magnetic iron garnets triggered by the IFE but at the same time the principle idea is the same: a spin precession is optically induced by a train of ultrashort laser pulses and if the precession frequency is tuned to certain values, resonance cases can be achieved and the spin precession amplified. In contrast to the iron garnet materials, the spins of the investigated semiconductor sample do not align by placing it into an external magnetic field, but by illuminating it with circularly polarized laser light of certain wavelengths, caused by selection rules. This is called optical spin orientation, or just optical orientation. Then, an external magnetic field splits the eigenstates for spin-up and spin-down, leading to a spin precession. Another distinction is the wavelenght of the laser light. While for the IFE it lies in the transparent region of the sample and the effect is based on Raman scattering, absorption is crucial for the optical spin orientation. This section starts with a general introduction to semiconductors and then explains the physics behind the spin precession induced by optical orientation.

2.4.1 Basics

A semiconductor is, as the name indicates, a material whose electrical conductivity lies between a conductor ($> 10^4\,\mathrm{S/cm}$), such as copper, and a dielectric ($< 10^{-10}\,\mathrm{S/cm}$), such as glass [Seeger, 1991]. They are characterized by the band gap E_g which is an energy range of a solid, where no allowed electron states exist, separating the top of the valence band and the bottom of the conduction band. At low temperatures the valence band is fully occupied with electrons while the conduction band is completely empty. The band gap can range from small values as $E_g = 0.18\,\mathrm{eV}$ for InSb to several eV such as $E_g = 5.48\,\mathrm{eV}$ for diamond [Kasap and Capper, 2006]. The band gap is either of direct or indirect type. In the former case the maximal-energy state in the valence band and the minimal-energy state of the conduction band occur at the same point in the Brillouin zone, while in the indirect band gap both extremes occur at different points. In a direct band gap semiconductor electrons and holes are assigned with the same momentum and, therefore, electronic transitions are allowed without the need of momentum transfer to the crystal lattice by an additional involved

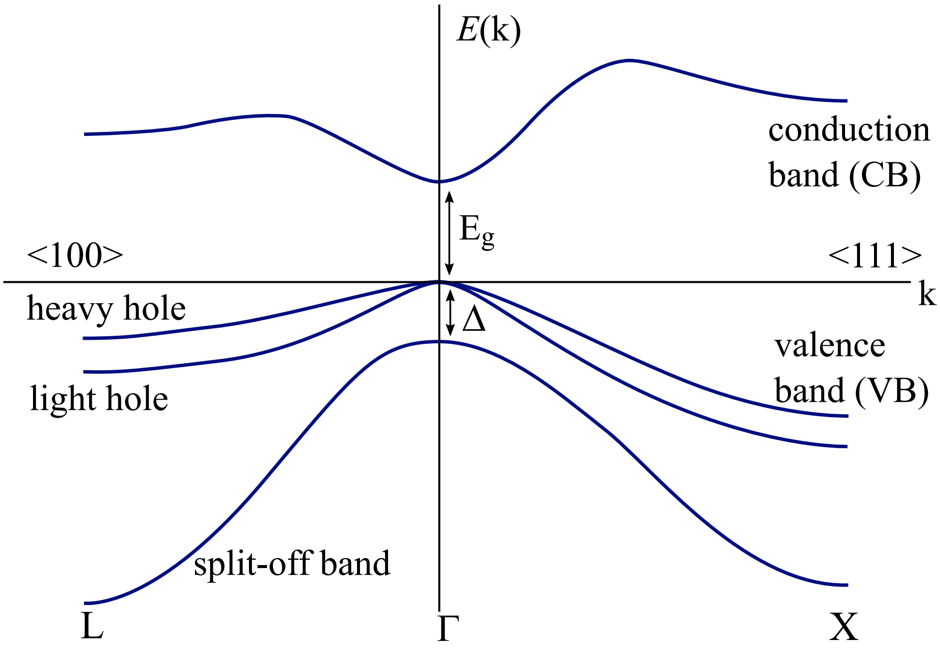

Figure 2.7: Band structure of the CdTe semiconductor along symmetry lines. The minimum of the conduction band and the maximum of the valence band lie both at the Γ point ($k = 0$), where the bands for the heavy and the light holes are degenerated. Drawing adapted from [Cardona et al., 1988].

phonon. The semiconductor CdTe investigated in this work has a direct band gap, its band structure is shown schematically in Fig. 2.7 [Cardona et al., 1988]. At the center of the Brillouin zone, the Γ point, the bands for the heavy and the light hole are degenerated. The split-off band is separated by the spin-orbit splitting Δ.

Modern sample fabrication methods allow preparations of nanostructures with different band gaps, such that the electrons are confined in space. Depending on the dimensions of confinement, there are quantum wells (confined in one dimension), quantum wires (two dimensions), and quantum dots (all three dimensions). Quantum wells (QWs) consist of a semiconductor film with a smaller band gap sandwiched by semiconductors with a larger band gap, see also Sec. 4.2. When the size of the QW is comparable to or smaller than the de Broglie wavelength, the confinement leads to quantum effects, resulting in discrete energy levels for electrons and holes in conduction and valence band, respectively.

2.4.2 Optical Spin Orientation and Bound Electron-Hole States

Optical transitions follow selection rules. Along with energy and momentum conversation, the conversation of the angular momentum is a fundamental law of physics. Photons of right and left handed circularly polarized light have an angular momentum of ±1 (in units of $\hbar$) along their propagation direction. When illuminated with light of either helicity, only

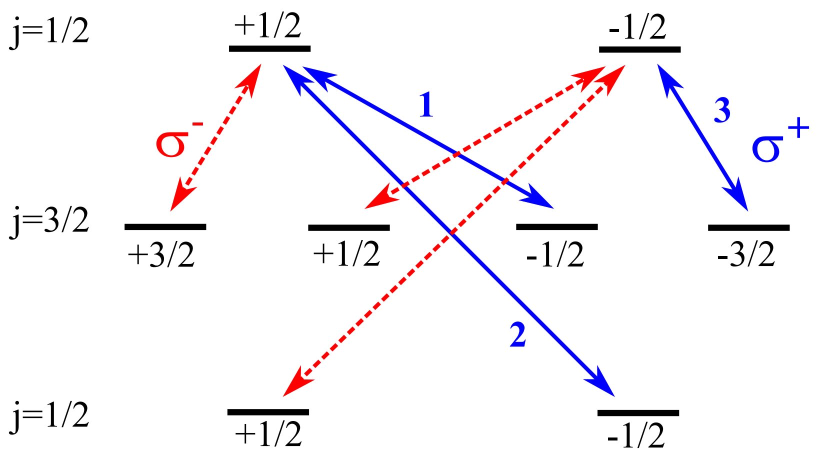

Figure 2.8: Optical transitions of electrons in semiconductors. The states (black bars) in the upper row are in the conduction band (total angular momentum $j = 1/2$), in the middle the light and heavy holes ($j = 3/2$) and in the lower row the split-off band ($j = 1/2$). The numbers under the states indicate m_j, the component of the angular momentum along the z axis. The blue arrows indicate optical allowed transitions under illumination with σ^+ light, the red for σ^- light. The bold number next to the blue arrows give the probability ratio of the transitions: 3:2:1.

certain transitions are allowed, see Fig. 2.8. For σ^+ polarized light, only the transitions indicated with blue arrows are allowed where $\Delta m_j = +1$, for example between the atomic state with $j = 3/2, m_j = -1/2$ and $j = 1/2, m_j = 1/2$. The different channels vary in their probabilities of transition when illuminated with the corresponding polarized light, indicated by bold blue numbers next to each arrow.

If the energy $\hbar\omega_{\text{exc}}$ of the incident photon is higher than the band gap but less than the additional spin-orbit splitting Δ, such that $E_g < \hbar\omega_{\text{exc}} < E_g + \Delta$, only transitions from the light and heavy hole band to the conduction band are allowed. Due to the different transition probabilities, three times more electrons are in the $m_j = -1/2$ state than in the $m_j = +1/2$ state. The average electron spin along the direction of excitation is then: $(+1/2)(1/4) + (-1/2)(3/4) = -1/4$ and the average hole spin $+5/4$, summing up to $+1$ which is equal to the angular momentum of the absorbed photons.

After the optical excitation of an electron, the former position of it in the valence band is empty leaving a hole behind, also called *electron hole*. Due to the missing negative charge, there is a net positive charge. For simplification, one can treat the electron hole as a quasiparticle which is positively charged and with an effective mass. Due to the Coulomb interaction between the electron and its hole, they are forming a hydrogen-like bound state, which is called *exciton* (often abbreviated with X). The exciton binding energy is typically of the order of several meV and does not exceed 1 eV. This is much smaller than the exciton binding energy of a hydrogen atom of $1Ry = 13.6\,\text{eV}$.

Excitons can be seen as an analogous to a hydrogen-atom. Then it should be possible to form a charged exciton, consisting of two electrons and one hole or vice versa, experimentally first observed in 1995 [Finkelstein et al., 1995], contributing to the photoluminescence spectrum below the free exciton energy. This formation of an exciton with an additional third (quasi-)particle, either electron or hole, is called *Trion* ($T^{\pm}$). Its total spin is half-integer and according to Kramer's theorem, it is doubly degenerated in absence of a magnetic field. [Akimov et al., 2008]

2.4.3 Larmor Precession

If additionally an external magnetic field is applied perpendicular to the direction of the excited spin and therefore also to the propagation direction of the photons (called *Voigt geometry*), the eigenstates for spin-up and spin-down are split up due to the Zeeman splitting. The magnetic field is directed along the x axis, the spins are oriented along the k vector of the laser beam, which is set as the z axis. We choose the spins $+1/2$ ($|\uparrow\rangle$) and $-1/2$ ($|\downarrow\rangle$) along x as a basis. Illumination by circularly polarized light leads to a superposition of the two eigenstates $(|\uparrow\rangle \pm |\downarrow\rangle)/\sqrt{2}$ with an oscillating phase called Larmor precession, whose frequency Ω_L is determined by the spin splitting due to the magnetic field:

$$\Delta E = \hbar\Omega_L = \frac{e\hbar B}{m_0}, \tag{2.43}$$

where e is the elementary charge. The Larmor frequency can be written as:

$$\Omega_L = \frac{g_0 \mu_B B}{\hbar}, \tag{2.44}$$

using the Bohr magneton $\mu_B = e\hbar/2m_0$ and the Landé g-factor of the free electron $g = 2.002$. The oscillation between the two states is also often called *spin beats*.

The same results can be achieved with a classical picture, where the external magnetic field $\mathbf{B}$ acts as a torque $\boldsymbol{\tau}$ on the magnetic dipole moment $\boldsymbol{\mu}$ produced by the macroscopic spin polarization: $\boldsymbol{\tau} = \boldsymbol{\mu} \times B$, similar to the magnetization precession from Sec. 2.2.2.

2.4.4 Spin Relaxation

Spin relaxation caused by disappearance of initial spin polarization is the central issue of the semiconductor research part of this work. The relaxation process can be described by two different times: T_1 and T_2, describing the relaxation of the longitudinal (parallel to B) and the transversal (perpendicular to B) spin component, respectively [Abragam, 1994]. The former process describes the relaxation from the upper to the lower Zeeman spin state. This requires energy dissipation to the surrounding, e.g. to the lattice by emission of phonons, and is therefore also called spin-lattice relaxation.

For the latter case, T_2 gives the time after which the phase relation of the two eigenstates of the Larmor precession is lost and therefore it is called *spin coherence* time. It does not necessarily come along with energy transfer and it is caused by any arbitrary scattering event. [Yakovlev and Bayer, 2008]

The term T_2 describes the coherence time of an individual spin. However, an ensemble of carrier spins have slightly different precession frequencies due to different g-factors or other inhomogenities. Thus, the additional term for inhomogeneous spin relaxation time T_2^{inh} is introduced:

$$\frac{1}{T_2^*} = \frac{1}{T_2} + \frac{1}{T_2^{\mathrm{inh}}}, \tag{2.45}$$

where T_2^* is the *spin dephasing time* in which the spin ensemble loses its coherence. It is the quantity which is usually measured experimentally.

The several possible mechanisms which can be responsible for spin relaxation are: [Maekawa, 2006]

Elliot-Yafet Mechanism: This is a spin relaxation by momentum scattering, e.g. on impurities or phonons, where spin-up and spin-down states are mixed and, therefore, a spin-flip can occur after a sufficient number of scattering processes.

Dyakonov-Perel Mechanism: This mechanism occurs in crystals with no inversion symmetry such as GaAs and is related to the spin-orbit splitting in the conduction band. Here, spin-up and spin-down electrons have different energies for the same momentum $\mathbf{p}$, leading to an effective magnetic field where the spins precess around. Due to scattering the momentum changes and so does the precession. This randomization leads to spin dephasing.

Bir-Aronov-Pikus Mechanism: This relaxation channel arises from spin-flip scattering of an electron on the holes and is due to the exchange interaction between their spins. It applies for p-type semiconductors.

Hyperfine Interaction with Nuclear Spins: This mechanism arises from the hyperfine interaction of the electron spin with the lattice nuclei and becomes important for localized electrons in impurity sites or confined in quantum dots.

3 Experimental Methods

This chapter describes the experimental techniques which were utilized to study magnetization dynamics and spin coherence. Basically two different methods of measuring came to use. Section 3.1.1 describes the first method, which is based on the magneto-optical Kerr effect (MOKE), performed in two different geometries (longitudinal and transversal) and is rather for a characterization of new samples than for studying unknown phenomena. In section 3.2 time-resolved pump-probe techniques are described. First a method with a low repetition rate laser system, where one single laser pulse is exciting the system out of its equilibrium position each time when one of the subsequent pulses arrives. Second, and the main part of this work, describes the method where a high repetition rate laser system was used. Here, the physical system gets excited by the laser pulse, but before it relaxes back to the equilibrium position, the next pulse is incident, which justifies the expression that we excite in this case by a 'train of laser pulses'.

3.1 Magneto-Optical Effects

Magneto-optical effects are all phenomena where light is influenced by the magnetization of a medium. First reported in 1845 by Michael Faraday [Faraday, 1846] who discovered the rotation of the plane of polarization of light after its transmission through a piece of glass which was placed between the poles of a magnet. The corresponding effect for a light beam reflected from the surface of a medium is known as the Kerr effect, at first discovered by John Kerr in 1877 [Kerr, 1877]. In general, when a linearly polarized beam is incident on the medium, the magneto-optical effects manifest in a rotation of the plane of polarization and an additional ellipticity for the light beam after transmission or reflection.

These effects originate from a Zeeman splitting of the ground and excited states creating an anisotropy of the magnetized medium [Freiser, 1968]. The presence of a magnetic field causes off-diagonal elements in the permittivity tensor ε of the material.

3.1.1 Magneto-Optical Kerr Effect (MOKE)

Depending on the orientation of the magnetization vector relative to the light's plane of incidence, we can distinguish between three different magneto-optical Kerr effects: polar, longitudinal and transverse, see Fig. 3.1, or abbreviated: PMOKE, LMOKE and TMOKE. Only the former two are of interest for the work of this thesis. In these cases, the influence of the magnetization of the medium manifests in a rotation of the plane of polarization and appearance of ellipticity in the reflected light beam, if linearly polarized light is incident [Zvezdin and Kotov, 1997].

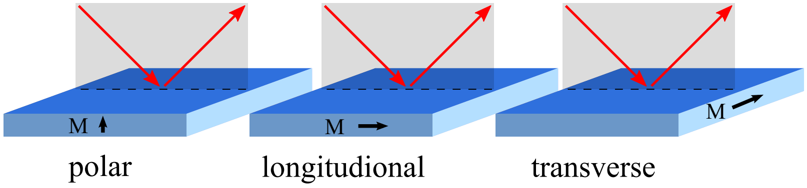

Figure 3.1: Different MOKE geometries, depending on the relativ orientation of the magnetization with respect to the plane of incidence of the light: polar (PMOKE), longitudinal (LMOKE) and transverse (TMOKE).

Since both Kerr rotation angle and Kerr ellipticity depend on the magnetization of the medium, measuring the two quantities gives an insight of the magnetization in the sample. A setup based on the magneto-optical Kerr effect, as schematically illustrated in Fig. 3.2, is employed to find out the minimal necessary externally applied magnetic field strength for which the magnetization of each sample is fully saturated, as well as to distinguish between the hard and easy axis of each sample. For this purpose, a cube laser is used as a source for continuous wave (cw) laser radiation with a wavelength of $\lambda = 405\,\mathrm{nm}$. Polarization optics, here a half-wave retardation plate ($\lambda/2$) in combination with a Glan-Thompson prism, allow the adjustment of power and polarization of the incident laser beam. The reflected beam is modulated with a frequency of 42 kHz in its polarization with a photo elastic modulator (PEM), whose main axis is perpendicular to the incident laser polarization. Only if the plane of polarization of the reflected light is rotated, it is modulated by the PEM. To measure the Kerr rotation angle, the PEM is set to half-wave retardation of the laser wavelength, for Kerr ellipticity measurements it is set to quarter-wave retardation. The second Glan-Thompson prism is tilted by 45° so that 50 % of the unrotated beam is transmitted. If the polarization of the beam is then rotated due to the Kerr effect, the intensity after the second prism is modulated, which is then measured by a photo diode and its output signal demodulated at the double PEM frequency $2f$ ($1f$ for Kerr ellipticity measurements) by means of a lock-in amplifier (Model 7230 by AMETEK Signal Recovery, USA).

3.1.2 Faraday Effect

Illumination of the sample by strong pump laser pulses induces a physical effect, which is of interest to investigate. The later arriving weaker probe pulse should be influenced by the perturbed system then to monitor the magnetization dynamics. For this, we utilize the normal Faraday effect, which is similar to the Kerr effect but for transmitted light instead of reflected. Like its counterpart, the Faraday effect manifests in a rotation and ellipticity of a formerly purely linearly polarized laser beam after transmission through the medium. The

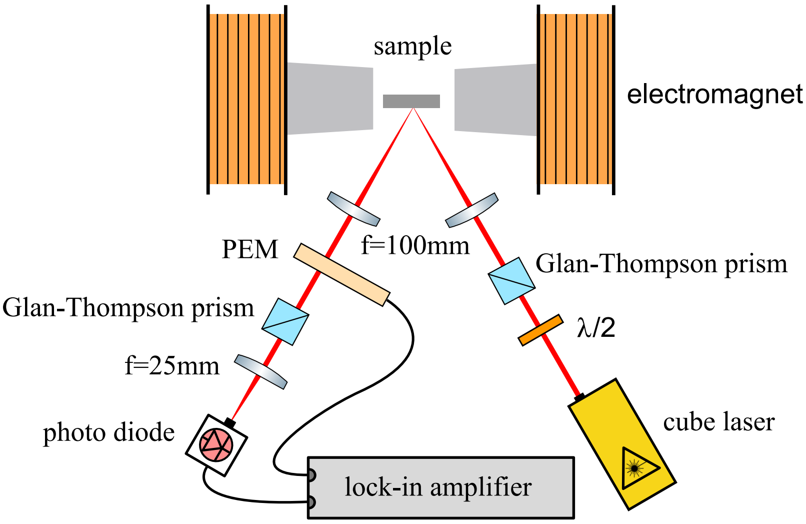

Figure 3.2: Scheme of magneto-optical Kerr measurements setup, here for the longitudinal geometry. For the polar geometry, the electromagnet is rotated by 90 degrees. In this case one ferrite is replace by one with a hole to direct the incident and the reflected laser beam through it. In this configuration the lenses for focusing on and collimating from the sample are replaced by lenses with focal length of 300 mm.

rotational effect originates from magnetic circular birefringence, which results in different velocities for left- and right-handed circularly polarized light. Linearly polarized light can be seen as a superposition of two circularly polarized waves with opposite helicities with a fixed phase between them. After passing through the optical active medium, the phase changes and therefore the direction of the plane of linear polarization [Zvezdin and Kotov, 1997]. Due to magnetic circular dichroism the absorption coefficients for both helicities are also different, which results in the additional ellipticity of the transmitted laser beam.

The angle of the Faraday rotation is

$$\phi_{\mathrm{FR}} = VBd \tag{3.1}$$

where V is the Verdat constant, B the magnetic field density along the propagation axis of the light and d the length of the path where the magnetic field interacts with the light. The sign of ϕ_{FR} depends on the sign of B, and therefore, the angle doubles when the light is reflected at the end of the material and travels back through it afterwards.[Zvezdin and Kotov, 1997] Since the Faraday rotation angle is proportional to the projection of the magnetic field along $\mathbf{k}$ of the propagating light, one can estimate the temporal evolution of the magnetic oscillations in the sample by measuring changes in the polarization plane of the transmitted probe beam.

Detection and Calculation of the Faraday Rotation Angle ϕ_{FR}

In all pump-probe setups, the detection of the probe laser was performed with a balanced difference photoreceiver consisting of two silicon diodes. A Wollaston prism splits the beam into two perpendicular to each other linearly polarized parts which are focused on one of the diodes each. With a half-wave retardation plate before the prism the plane of polarization can be adjusted in a way that the intensity of both split beams are equal. The output signal of the receiver in this case is $\Delta U = 0$.

When the magnetization in the sample along the k vector of the probe is changing after the pump pulse was incident, the plane of polarization is rotating due to the normal Faraday effect. For small angles one can easily calculate it by detecting the difference signal ΔU and the total intensity I_{tot}.

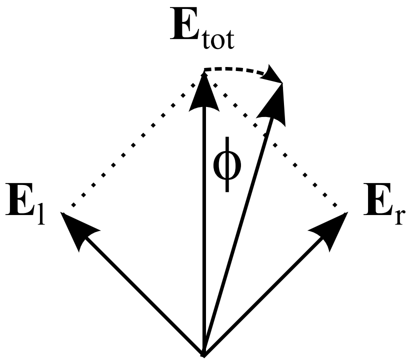

Figure 3.3: Illustration for calculating the Faraday rotation angle ϕ. $\mathbf{E}_{\mathrm{tot}}$ is the electric field vector of the incoming probe beam before transmitting through the Wollaston prism, $\mathbf{E}_l$ and $\mathbf{E}_r$ the electric field vectors of the beams incident on the left and the right diode, respectively, of the photoreceiver.

According to Fig. 3.3, the electric field amplitudes $E_i = |\mathbf{E}_i|$ of both beam fractions are

$$E_l = \cos\left(\tfrac{\pi}{4} + \phi_{\mathrm{FR}}\right) E_{\mathrm{tot}} \tag{3.2}$$

$$E_r = \cos\left(\tfrac{\pi}{4} - \phi_{\mathrm{FR}}\right) E_{\mathrm{tot}} \tag{3.3}$$

where E_{tot} is the electric field component of the probe beam before it is split and E_l and E_r the field components for the beams incident on the left and the right diode, respectively. With $I = |E|^2$ one can write

$$\Delta I := I_r - I_l = \left[\cos^2\left(\frac{\pi}{4} - \phi\right) - \cos^2\left(\frac{\pi}{4} + \phi\right)\right] I_{\mathrm{tot}}. \tag{3.4}$$

With the reduced trigonometric expression

$$\cos^2\left(\frac{\pi}{4} \pm \phi\right) = \frac{1}{2}\left(1 \mp \sin(2\phi)\right), \tag{3.5}$$

$U \propto I$, $U_{\mathrm{tot}} = 2U_{\mathrm{DC}}$ (U_{DC} is the average voltage measured on one diode) and the small-angle approximation ($\sin\phi_{\mathrm{FR}} \approx \phi_{\mathrm{FR}}$) follows from equation (3.4) an expression for the Faraday rotation angle:

$$\phi_{\mathrm{FR}} \approx \frac{\Delta U}{4U_{\mathrm{DC}}}. \tag{3.6}$$

For the investigation on the CdTe sample (see section 4.2 and chapter 7) we measure the Faraday ellipticity, for this purpose an additional quarter-wave plate was put into the probe beam in the detection in front of the Wollaston prism.

3.2 Time-Resolved Pump-Probe Techniques

Since the aim of this work is the study of magnetization dynamics which happen on the time scales of picoseconds a time-resolved measurement technique with a resolution of the same time scale or better is necessary. With commercially available femtosecond laser systems modern optical pump-probe techniques are a suitable way to obtain these time resolutions. The idea of this method is to excite the sample with a first strong pulse into a non-equilibrium state, followed by a second weaker pulse probing the response of the sample. These pulses are named *pump* and *probe* pulses, respectively. Increasing the time delay t between both pulses gives the sample response at different points in time, leading to time-resolved spectroscopy. Two different techniques are used in this work, conventional optical sampling with a delay line for varying the time delay (Section 3.2.2) and a less common approach without any mechanically moving elements, called *asynchronous optical sampling* or in short ASOPS (Section 3.2.3).

3.2.1 Geometries

For all pump probe experiments we used the geometry shown in Fig. 3.4. The sample plane lies in the xy-plane with the z-axis along the sample surface normal. The externally applied magnetic field H_{ext} is directed along the x-axis. Pump and probe beams are focused by the reflective microscopic objective under an angle of $(17 \pm 6)\,^{\circ}$ with respect to the z-axis. The pump and probe beams are directed along the red and the orange rod, and are tilted in x and y direction, respectively.

3.2.2 Single Pulse Optical Excitation

A schematic illustration of the experimental setup for the single pulse excitation can be seen in Fig. 3.5.

Source of the laser radiation is the PHAROS lasersystem (by Light Conversion, Lithuania), a Yb oscillator emitting strong laser pulses at a center wavelength of $\lambda = 1030\,\mathrm{nm}$ and repetition rate of $F_{\mathrm{Rep}} = 30\,\mathrm{kHz}$, triggered by an internal clock. The radiation is then divided into a strong pump beam and a weaker probe beam, which is directed through an optical

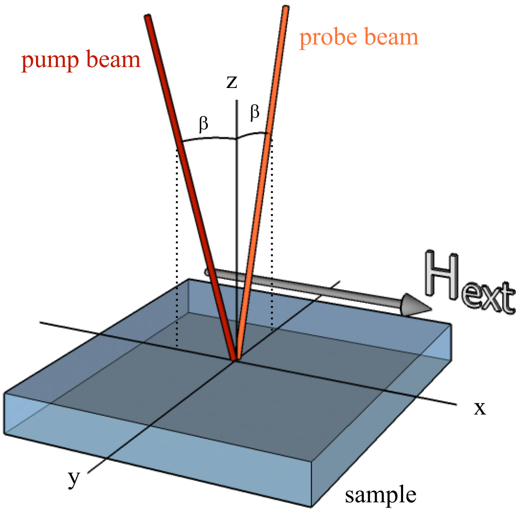

Figure 3.4: Geometry of all pump probe experiments. The externally applied magnetic field H_{ext} is directed along the x-axis. Pump (along the red rod) and probe (orange rod) are incident on the sample (blue cuboid) under an angle of 17 °with respect to the z-axis (normal to the sample surface). The tilt is in x and y direction for pump and probe, respectively.

parametric amplifier (OPA) ORPHEUS-PS (by Light Conversion, Lithuania), changing its wavelength tunable between 515 – 1030 nm. This two-color pump-probe setup allows the installation of a shortpass filter (FES) at 950 nm in the detection, eliminating scattered pump light to reduce noise significantly.

The pump beam is directed on a mechanical delay line to adjust the temporal delay t between both laser beams. The delay line consists of a retroreflector (RR) mounted on a linear translation stage. The length of the delay line of $l = 1\,\text{m}$ limits the maximal delay to $t = s/c = 2l/c \approx 6.7\,\text{ns}$, with c for the speed of light.

Afterwards the pump beam is passing through an electro-optical modulator (EOM) consisting of a Pockels cell, which responds to an electric field by modification of the refractive index. If the upper and lower level of an AC rectangular voltage is chosen correctly, the polarization of the laser is modulated between 0 °and 90 °rotation. With an additional quarter-wave plate ($\lambda/4$) after the EOM the polarization of the laser beam is modulated between left- and right-handed circularly polarized light (σ^- and σ^+, respectively). A function generator is converting the laser clock signal into a rectangular signal with half of its frequency, which is then passed through a pulse amplifier delivering the required voltages for the Pockels cell. With $F_{\text{EOM}} = F_{\text{Rep}}/2$ each subsequent pump pulse is modulated between σ^+ and σ^- polarized light.

To compensate for angular divergence of the probe beam, a telescope is installed. Two lenses with focal length of $f = 150\,\text{mm}$ each are varied in their distance with $d \neq 2f$ so that the beam after passing the second lens is collimated.

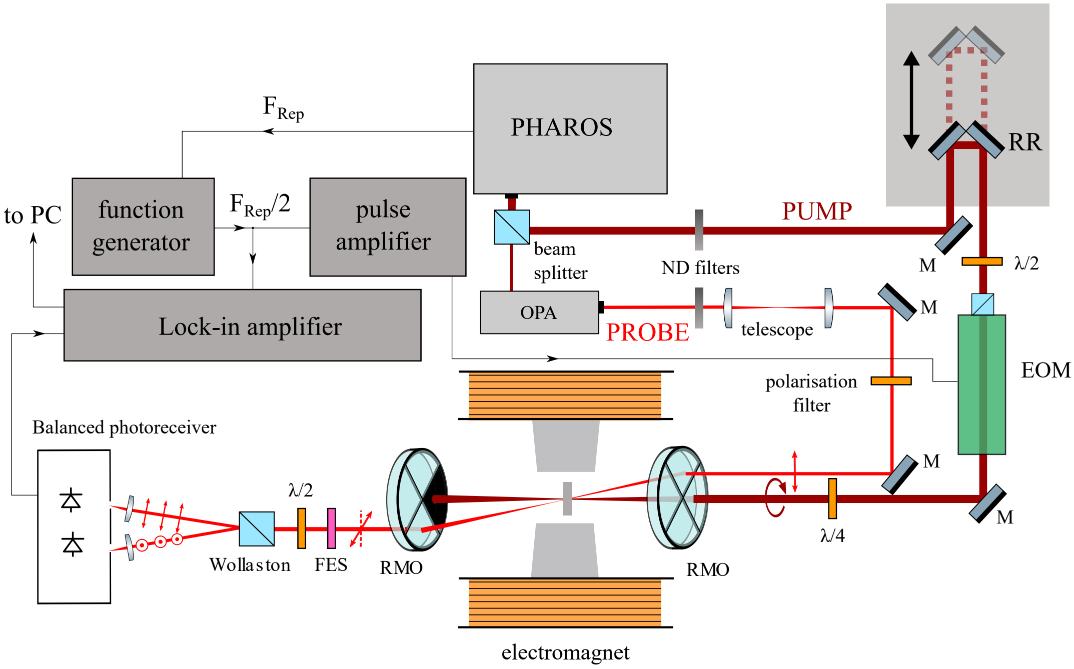

Figure 3.5: Scheme of the single pulse excitation setup. M: silver mirrors, RR: retroreflector, ND filter: neutral density filter, EOM: electro-optical modulator, $\lambda/4$ and $\lambda/2$: quarter- and half-wave retardation plate, RMO: reflective microscope objective, FES: short pass filter.

The pump and probe beams are adjusted in their intensities by neutral density filters (ND filters) and focused by a gold coated reflective microscope objective (RMO, distributed by Newport Spectra-Physics GmbH, Germany) on the sample surface on spot diameters of about 8 and 9 μm. The sample is in the middle of an electromagnet (distributed by GMW Associated, USA) with a variable pole distance allowing to apply magnetic fields of up to about 500 mT. For low temperature measurements the sample is put into a liquid helium flow cryostat MICROSTAT HE-R (by Oxford instruments, United Kingdom) and cooled down by liquid helium to temperatures of $T \approx 10$ K. The transmitted probe beam is then collimated by a second RMO and passed through a short pass filter (FES) for elimination of scattered pump light and a Wollaston prism in combination with a half-wave retardation plate ($\lambda/2$). The latter is required for balancing the intensities on the two diodes, while the prism divides the beam into two perpendicular to each other polarized beams, propagating under an angle of 20°. Both parts of the beam are then focused on the diodes of a balanced difference photoreceiver (NIRVANA 2007 by Newport Spectra-Physics GmbH, Germany). According to section 3.1.2 and equation (3.6) one can measure and calculate the Faraday rotation angle ϕ_{FR} by measuring the output voltage of the receiver ΔU and the average DC signal per diode U_{DC}.

The photoreceiver output signal, modulated at the EOM frequency, is passed on to a lock-in amplifier (SR830 by Stanford Research, USA) which demodulates the signal, leading to a strongly increased signal-to-noise ratio.

3.2.3 High Repetition Optical Excitation

Here, we are using a laser system with a high repetition rate of $F_{\mathrm{Rep}} = 1\,\mathrm{GHz}$. The short temporal distance between two subsequent emitted pulses ($T_{\mathrm{Rep}} = 1\,\mathrm{ns}$) justifies the expression of a 'train of laser pulses'. However, this also means low pulse energy when the total laser intensity cannot be increased arbitrarily. With a maximum pump power of about $P_{\mathrm{Pump}} = 50\,\mathrm{mW}$ the energy of each pulse is as low as $E_{\mathrm{pump}} = 50\,\mathrm{pJ}$. Consequently, we expect only a small magnitude of the inverse Faraday effect induced by the laser pulses, which requires a sufficiently large signal-to-noise ratio. To achieve high repetition optical excitation with low noise of the total signal, we utilized the ASOPS technology, which will be introduced at the beginning of the following section. Then, details of the used laser system will be given, followed by an extensive description of the optical setup.

Asynchronous Optical Sampling

Asynchronous optical sampling (ASOPS) is a method for time-domain spectroscopy with some advantages over ordinary pump-probe techniques. For this approach two independent mode-locked Laser oscillators are employed, one (the probe beam) with the fixed repetition rate F_{Rep}, the other (pump beam) with a repetition rate which has a small constant offset such that $F_{\mathrm{Rep,Pump}} = F_{\mathrm{Rep}} + \Delta F$. Due to this offset the time delay t between both pulses is linearly increased with every subsequent emitted pulse pair from zero delay (temporal overlap of both pulses), see Fig. 3.6, until $t = 1/F_{\mathrm{Rep}}$ and both pulses coincide again. This means, the time window T between two following pump pulses is scanned automatically after $1/\Delta F$ real time. When acquiring time resolved signals, the probe beam is detected and digitalized as a function of the real-time, which can be calibrated into a time delay scale by applying the conversion factor $\Delta F/F_{\mathrm{Rep}}$. Further noise reduction is possible by averaging several time traces. [Bartels et al., 2006]

Advantages over conventional time-resolved measuring methods, i.e., with a mechanical employed time delay, besides the quick data acquisition time, is a high signal-to-noise ratio, which is in our case a relative noise of 10^{-8} compared to the total signal $2U_{\mathrm{DC}}$, and the absence of fundamental limits due to mechanical movements, such as beam pointing and diameter stability. Since the offset frequency ΔF can be stabilized as a much higher frequency than any mechanical movement control could operate, the effective bandwidth of this technique can be much higher. [Prasankumar and Taylor, 2016]

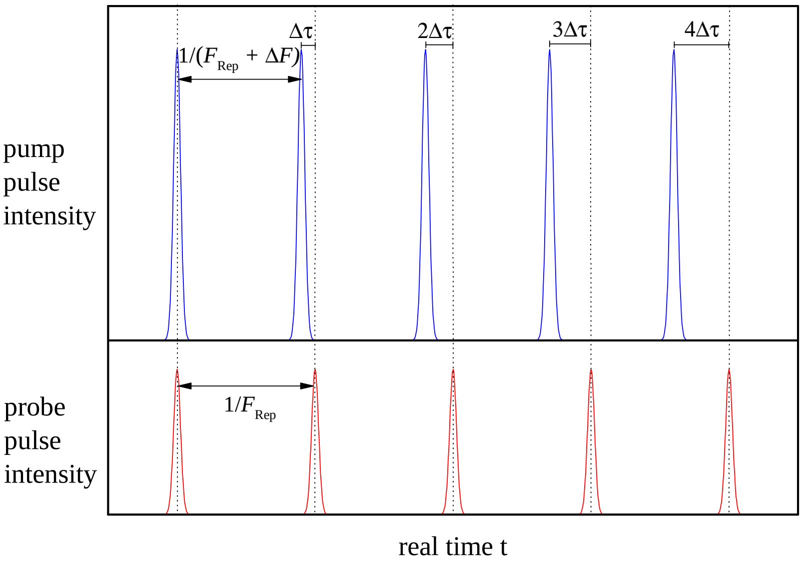

Figure 3.6: Schematic illustration of the increasing time delay between pump and probe with every subsequent emitted pulse pair with real-time axis.

Laser System

To use the ASOPS technique, consequently two laser oscillators are required. Here we use the commercially available laser system Gigajet twin 20c/20c (distributed by Laser Quantum Ltd, UK) containing two almost identical Ti:sapphire oscillators (called *master* and *slave*) emitting pulsed laser radiation with repetition rates of $F_{\mathrm{Rep}} \approx 1\,\mathrm{GHz}$, pulse durations of about 50 fs at wavelengths independently tunable between 750 and 850 nm. The oscillators are pumped optically by a 532 nm continuous wave laser Finesse pure 10W (Laser Quantum Ltd., UK), whose emitted beam is divided by a 50/50 beam splitter and then guided to each of the oscillators. The offset between the repetition rate of both laser beams have been set to $\Delta F = 2 - 20\,\mathrm{kHz}$, leading to step sizes of $\Delta t \approx 5 - 50\,\mathrm{fs}$ and a scan time of $5 - 50\,\mu\mathrm{s}$ for acquiring one time trace. The signal, measured by a photoreceiver, is then digitalized by a PCIe digitizer card (Razor Express 14X2 CompuScope, by GaGe Applied Technologies) inside of a computer. This 14-bit card acts as a fast 125 MHz oscilloscope, triggered by the TL-1000 unit (see below), where the digitized measured time traces are saved by the computer. All measured time traces acquired by the ASOPS system which are shown in this thesis are averaged over a high amount of single measurements, depending on the desired signal-to-noise ratio. Typically it is averaged over 1,024,000 million single traces, leading to a total duration of 51.2 s per measurement (for $\Delta F = 2\,\mathrm{kHz}$). For some measurements it was convenient to measure more than one time window of 1 ns, consequently the measuring time increases in these cases. If the signals are very weak, more averaging might be necessary to achieve a better signal-to-noise ratio.

To achieve the desired offset ΔF in the repetition rates, two of the cavity mirrors in the slave oscillator are mounted on piezo crystals with which the cavity length can be controlled electronically and, therefore, the repetition rate. In order to maintain a well-defined calibrated time axis, the offset has to be stabilized actively. For this a small part of each emitted laser beam is picked up by a beam splitter and focused on fast 10 GHz bandwidth photodetectors ET-4000 (EOT Inc., USA). Their signal is fed to the TL1000-ASOPS (Laser Quantum Ltd., UK) repetition rate offset stabilization unit. In principal, the actual offset between both repetition rates is measured and the difference to the desired offset $\Delta F = 2 - 20\,\mathrm{kHz}$ given as the error frequency, which is then used for the control of the two piezo crystals where one is slowly driven for the correction of a rough and merely temporal constant deviation of the offset frequency, while the other one can be changed very quickly to compensate external perturbations of the system (e.g., by sudden vibrations on the setup table). This enables stable measurements over a long time allowing averaging of multiple time traces for noise reduction. To achieve a minimal possible temporal resolution of 45 fs, the electronic stabilization unit works with the 10^{th} harmonic of the measured repetition frequencies, for more information see the paper of Gebs et al. [2010].

Experimental Setup

A scheme of the experimental high repetition rate setup can be seen in Fig. 3.7.

Since both pump and probe beams contain angular divergence, they are passed through telescopes. The focal lengths of the lenses are $f_{\mathrm{Pump},1} = 200\,\mathrm{mm}$ and $f_{\mathrm{Pump},2} = 150\,\mathrm{mm}$ and $f_{\mathrm{Probe},1} = f_{\mathrm{Probe},2} = 100\,\mathrm{mm}$ for the pump and probe beams, respectively. The choice of the focal lengths and the distances between both lens pairs determine the beam angular divergence and their diameters when they enter the reflective microscope objective (RMO) entrance sectors. They have to be small enough in diameter to not be cut off at the sector edges and at the same time as big and collimated as possible, to focus the beams on spot sizes of not more than 10 and $12\,\mu\mathrm{m}$ for probe and pump, respectively. Bigger spot sizes would decrease the pump fluency density quadratically and therefore the strength of the inverse Faraday effect.

A polarization bridge, consisting of a half-wave plate ($\lambda/2$) and a Glan-Thompson prism, allows to reduce and adjust the pump laser intensity. An additional quarter-wave plate ($\lambda/4$) polarizes the laser radiation circularly, which can be switched from right- (σ^+) to left-handed (σ^-) helicity. The beam is then directed to the sample via a mirror on a piezo motor driven mount (CONEX-AG-M100D distributed by Newport Spectra-Physics GmbH, Germany) with absolute positioning ability. This enables to shift the focused pump and probe beams away from each other for measuring traveling spin waves. The mirror mount is placed as close as possible in front of the RMO to maximize the tilt angle range.

For the probe beam much weaker intensities are necessary. Thus, a half-wave plate ($\lambda/2$) in combination with a fused silica wedged window, on which the beam incides under the

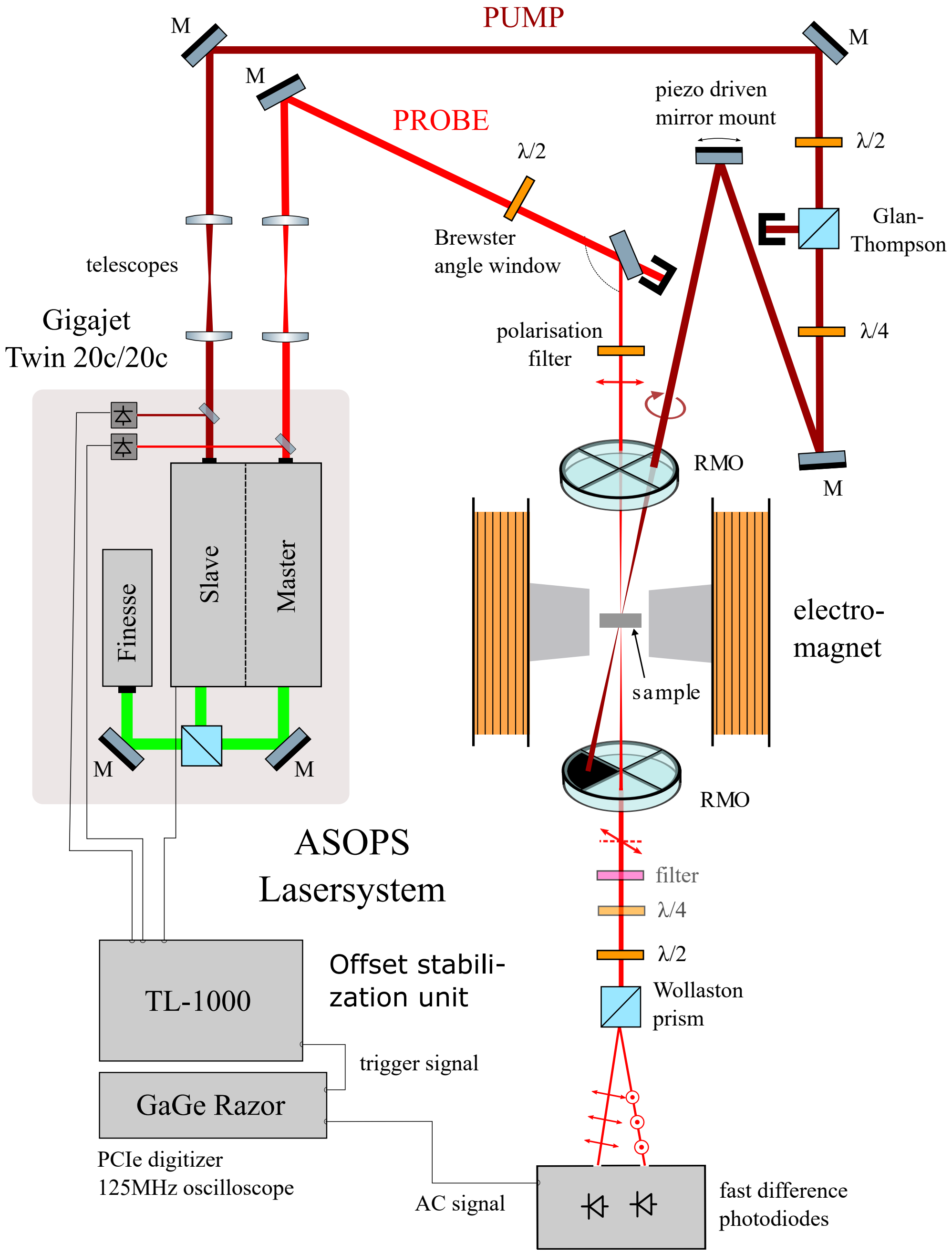

Figure 3.7: Scheme of the 1 GHz setup in transmission geometry for IFE and SW propagation measurements. M: silver mirrors, highly reflective for NIR light, $\lambda/2$ and $\lambda/4$: half- and quarter-wave retardation plates, respectively, RMO: reflective microscopic objective.

Brewster angle β, is built in the beam path. Only s-polarized light is reflected from the front surface of the window, and therefore, by rotating the plane of polarization of the incident beam, the intensity of the reflected beam can be adjusted between $\sim 0 - 13\,\%$.

Focusing on the sample, collimating, and detection is almost equal to the setup of section 3.2.2. In the detection a NewPort 2107-FC photoreceiver with Silicon diodes is used instead of the Nirvana and an optional bandpass filter (chosen accordingly to the probe wavelength) instead of the short-pass filter. Again, for low temperature measurements the sample is located in the He flow cryostat and cooled down by liquid helium to temperatures of $T \approx 10\,\mathrm{K}$. For ellipticity measurements an additional quarter-wave retardation plate ($\lambda/4$) is necessary before the half-wave retardation plate. The photoreceiver allows to adjust a gain up to $G = 3 \times 10^4$ and a DC filter, resulting in an AC output signal. This signal is then digitized by the digitizer card, averaged by the computer and saved.

Some of the measurements have been performed in a reflection geometry. For this purpose a 100 nm thick gold film is applied on the side of the magnetic film from where the probe beam is reflected. One single RMO acts for both focusing and collimating. This geometry has the advantage of a larger signal, since the beams are passing the sample twice doubling the effective sample thickness, which results in a twice larger Faraday rotation angle according to equation 3.1. On the other hand the signal is more sensitive on focusing the beams on the sample (on the interface between magnetic and gold film), leading to an increased noise if vibrations cause small modulations of the focus position of the sample.

Pulse Shaping

For the measurements on the CdTe semiconductor, the expected Faraday rotation and ellipticity signal is strongest when the probe beam is in resonance with the trion energy of the sample. To achieve the largest signal, the wavelength should be on the same spectral position and as narrow as the resonance linewidth. The emitted pulses of the laser system have a duration of about 50 fs, thus, their spectral width becomes several nanometers broad due to the time-energy uncertainty. To sharpen the spectral width of the probe beam, a pulse shaper as depicted in Fig. 3.8 is built into the probe beam path of the setup in Fig. 3.7 between the telescope and the polarization filter.

When light is incident on a grating with slits spacing d, it gets diffracted, which leads to maxima of j-th order. The angle of the first order of the diffracted beam is calculated by

$$\theta = \arcsin\left(\frac{\lambda}{d} - \sin\theta_i\right) \tag{3.7}$$

with θ_i as the angle of the incident light and λ for the wavelength of the light. According to the equation above, the grating disperses the different spectral components of the incident light at slightly different angles. A spherical mirror with a focal length of $f = 500\,\mathrm{mm}$ is collimating and reflecting the beam. A slit, variable in its width, is then blocking all light

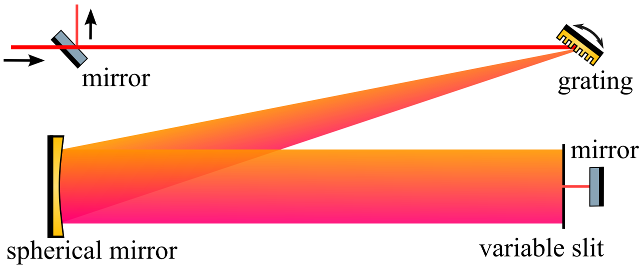

Figure 3.8: Graphical illustration of the pulse shaper. The incident light beam with a broad spectrum is diffracted by a specially designed gold grating. In combination with a gold coated spherical mirror and a slit with a small width, a narrow part of the spectrum can be separated with FWHM of $\approx 1\,\mathrm{nm}$.

except of that with the desired center wavelength. The width of the spectrum is much more narrow then and tunable by the slit width. The energy-time uncertainty leads to a temporal broadening of the laser pulses, which limits the temporal resolution of the measured time traces.

Both grating and spherical mirror are gold coated to increase the reflectivity. The former is designed in a way that the first diffraction order has the highest intensity (instead of the reflected beam). By rotating the grating one can choose the center wavelength which is led through the slit, and by changing the width of the slit, one can change the spectral width of the beam after passing through the pulse shaper.

Since a big part of the light is blocked in the pulse shaper, the intensity of the outgoing beam is much smaller. Hence, the fused silica window is not necessary anymore. Instead, the intensity is adjusted with an additional neutral density filter.

3.2.4 Calibration of the Piezo Motor Driven Mirror Mount

For the spin wave measurements, pump and probe spots have to be shifted away from each other when hitting the sample surface. For stability reasons, it is more suitable to shift the pump beam. To get reproducible results, a closed-loop piezo motor driven mirror mount in the path of the pump beam path is used. The minimum step size of the mirror mount is $\varphi = 0.001^\circ$. The calibration is done by increasing the tilt angle and measuring the shift distance s of the pump on the display of the camera imaging the sample surface, performed for all four directions ($\pm x$-axis and $\pm y$-axis displacement from center) separately, see Fig. 3.9. Since the pump is going through the side entrance sector of the objective, the shift in plus and minus x direction might differ, while for the y direction it should be the same due to the symmetry.

A linear function is fitted via the least square method to the experimental results, for the fitparameters m for the slope and b for the intercept, see Tab. 3.1. The results for $\pm y$ are

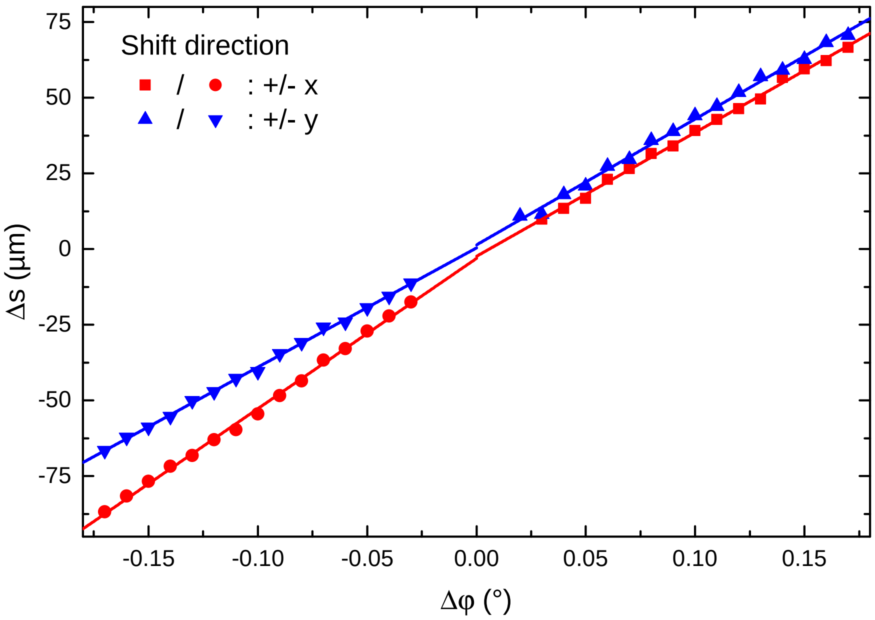

Figure 3.9: Calibration of the piezo motor driven mirror mount. Measured shift distance s for increasing tilt angle φ (symbols) and least square fit of a linear function (lines) for each direction.

very similar, the difference is just a few percent. From there, one can calculate the step size in degree per micrometer distance:

$$s = m\varphi + b. \tag{3.8}$$

The standard error of the resulting distance can be calculated using the propagation of uncertainty method:

$$\Delta_s = \sqrt{(m\Delta_\varphi)^2 + \Delta_b^2}, \tag{3.9}$$

where Δ_i is the absolute error of the quantity i.

Shift direction	m [μm/°]	Δ_m [μm/°]	b [μm]	Δ_b [μm]
$+x$	1493	±20	-8.7	±2.2
$-x$	1812	±23	11.3	±2.5
$+y$	1517	±23	5.1	±2.5
$-y$	1438	±16	-1.7	±1.7

Table 3.1: Fit paremters for the calibration of the piezo motor driven mirror mount.

The absolute error of the shift is in almost all cases around1 μm. Only for shifts smaller than 17 μm in $-y$ direction it is about 0.5 μm.

3.2.5 Calculation of the Polar Angle of the Magnetization Oscillations

All measured time traces give the signal in terms of the Faraday rotation angle ϕ_{FR}. Since the specific Faraday rotation value is strongly dependent on the investigated material, the polar angle of the magnetization oscillation θ, the quantity we are actually interested in, can differ heavily for various samples. θ is the angle between the magnetization $\mathbf{M}$ and the sample surface and is for small angles given by:

$$\theta = \arcsin \frac{M_z}{M} \approx \frac{M_z}{M}, \tag{3.10}$$

where M_z is the out-of-plane component of the magnetization and $M = M_s = |\mathbf{M}|$. Since the measured signals are only weakly alternating, i.e., $M_x \approx M = \text{const.}$ and the probe beam is propagating in the YZ-plane, the Faraday rotation angle can be written as:

$$\phi = v M_z d, \tag{3.11}$$

where v is a proportionality constant and d the magnetic film thickness. After measuring the Faraday rotation angle ϕ_0 for the magnetic film saturated in the out-of-plane direction, the angle of the magnetization oscillation can be calculated by:

$$\theta \approx \frac{M_z}{M} = \frac{\phi}{\phi_0} \tag{3.12}$$

For measurements in reflection geometry, the FR angle ϕ_{FR} doubles, thus, the equation above has to be additionally divided by a factor of 2.

4 Investigated Samples

In this chapter the investigated samples are introduced. Within the scope of this thesis the investigations on two different types of samples are presented. The main part is about different Bismuth-substituted magnetic iron garnet films, see Sec. 4.1, while the last part of this work is about a semiconductor CdTe/CdMgTe quantum well, see Sec. 4.2.

4.1 Iron Garnet Films

4.1.1 General Properties

Natural garnets have been playing an important role for many centuries as gem stones. Depending on their chemical composition, several different gems are known, as pyrope, almandine or demantoid, with characteristic colors originating from the content of transition metals such as Fe, Mn, Cr or Ti [Winkler, 1981].

Synthetic production of ferrimagnetic garnets started in the 1950s and with their many interesting properties in magnetism, soon they became a favorable material to be studied intensively. Nowadays, they are highly useful due to the possibility of a wide range of chemical substitutions, with a particular crystal structure, for tailoring the sample to favored properties.

According to the work of Menzer [1930], garnets form crystals of a cubic symmetry. The general formula of garnets is $\{C_3^{3+}\}[A_2^{3+}](D_3^{3+})O_{12}^{2-}$ where C, A, and D are cations with eight, six and four nearest oxygen ion neighbors, located on the center of the dodecahedral c-sites, the octohedral a-sites and tetrahedral d-sites of the oxygen polyhedra, respectively, see also Fig. 4.1. All cations with an ionic radius between 0.26 and 1.29 $\mathring{A}$ can be incorporated into the crystal lattice of garnets which offers a tremendous variety of possible combinations, enabling 'molecular engineering' to synthesize garnets with desired physical parameters such as the anisotropy energy. The lattice constant of garnets is typically between 12 and 13 $\mathring{A}$. [Winkler, 1981]

The prototype and most studied ferrimagnetic iron garnet is yttrium iron garnet (YIG) or $Y_3Fe_5O_{12}$ with low absorption and high Faraday rotation for wavelengths above $\lambda = 1000\,\text{nm}$ [Wettling et al., 1973]. When used in the visible or near infrared (NIR) region, the Faraday rotation angle can be enhanced by substituting suitable ions at the dodecahedral sites (where the yttrium ions in YIG are located). It has been seen that bismuth is a suitable

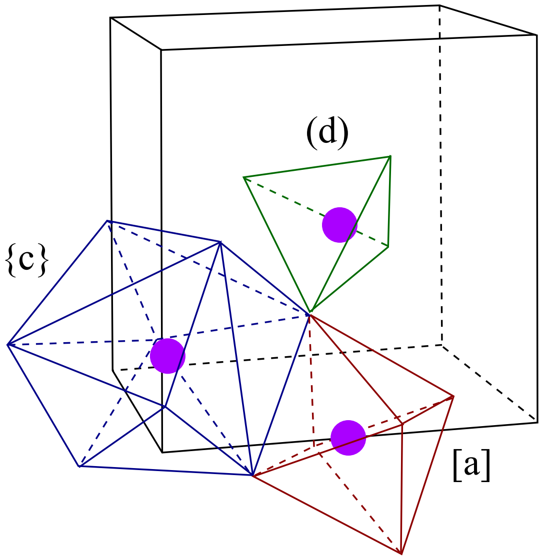

Figure 4.1: The garnet crystal structure, adapted from [Gilleo and Geller, 1958]. Illustration of the arrangement of the {c}, [a] and (d)-sites in the center of octahedra, dodecahedra and tetrahedra, respectively. The cube represents one octant of the unit cell.

material, enhancing the Faraday rotation angle and the strength of magneto-optical effects greatly [Robertson et al., 1973].

4.1.2 Bismuth Substituted Iron Garnets

The magnetic properties of iron garnets arise from the magnetic ions. In our case for bismuth iron garnet (BIG) the Bi^{3+} are diamagnetic, and the trivalent Fe^{3+} ions (see table 4.1) are responsible for the net magnetic moment of the material. Each ion is in the $3d^5$ electronic configuration, leading to $S = 5/2$ and $L = 0$ and a weak coupling with the crystal lattice, i.e., with phonons. In a ferrimagnet they exhibit a magnetic moment of around $\pm 5\mu_B$ (where μ_B is the Bohr magneton) at the absolute zero temperature $T = 0\,\mathrm{K}$ [Kittel, 2004]. Each iron ion is surrounded by oxygen ions, influencing their electronic configuration and mediating a superexchange interaction between the sublattices of the Fe^{3+} ions on the [a]- and (d)-sites, see also Fig. 4.2. According to the Neel model of ferrimagnetism, the two sublattices are ordered magnetically antiparallel [Winkler, 1981] which results in a net magnetism of one Fe^{3+} ion or $5\mu_B$ per formula unit of $Bi_3Fe_5O_{12}$. While fully substituted BIG has a large Faraday rotation angle and pronounced magneto-optical properties, its absorption is rather high in the spectrum of visible light [Kahl et al., 2003]. To increase $\phi_{\mathrm{FR}}/\alpha$, the magneto-optical figure of merit and relation of the specific Faraday rotation angle ϕ_{FR} to the absorption α, substitutions are necessary. For example, substituting the tetrahedal sites by gallium (Ga) lowers the saturation magnetization M_s, and substituting the octaheral sites by scandium (Sc) increases M_s [Scott and Lacklison, 1976].

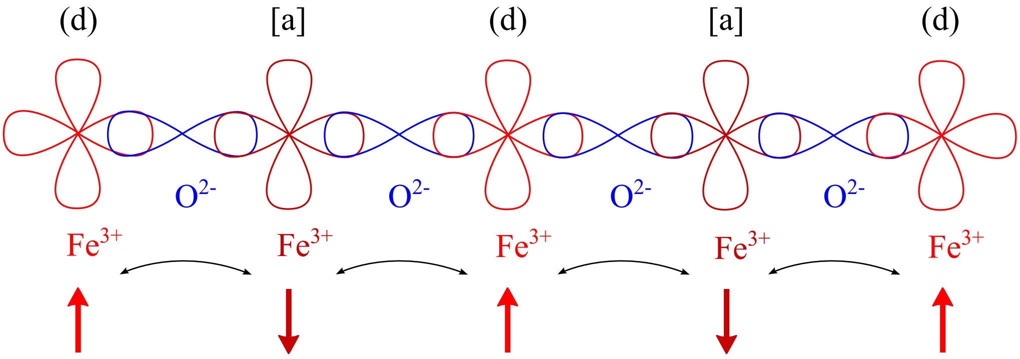

Figure 4.2: Illustration of the superexchange coupling in magnetic iron garnets between the 3d orbitals of the Fe^{3+} cations through the 2p orbitals of the intervening O^{2-} anions. The two electrons of the 2p shells in the oxygen ions must be antiparallel according to the Pauli exclusion principle, which are shared with the 3d shells. Hence the three iron ions from the tetrahedral (d) sites and the two from the octahedral [a] sites have antiparallel spins, leaving a net magnetic moment of $5\mu_B$ from one iron ion per unit cell BIG.

4.1.3 Investigated Magnetic Iron Garnet Samples

In this thesis the work on three studied magnetic iron garnet samples with different chemical compositions is shown. An overview of the compositions and film thicknesses is listed in table 4.1. All three sample were grown with liquid phase epitaxy on gadolinium gallium garnet (GGG) substrates with substrate composition of $Gd_3Ga_5O_{12}$ for sample-A and -B and $(CaMgZrGd)_3Ga_5O_{12}$ for sample-C. To calculate the polar angle of the magnetization after being deflected, the maximum FR angle for each film when fully magnetized in out-of-plane direction is needed (see also Sec. 3.2.5), which is given for $\lambda = 800\,\text{nm}$ for the specific sample thickness in the last column of the table.

Sample	Chemical composition	Thickness [μm]	ϕ_0 [deg]
A	$(Bi_{0.9}Lu_{1.4}Tm_{0.4}Y_{0.2}Sm_{0.1})(Fe_{4.7}Ga_{0.3})O_{12}$	5.0	1.3
B	$(Bi_{0.8}Lu_{2.2})Fe_5O_{12}$	4.0	2.0
C	$(Bi_{1.4}Y_{1.6})(Al_{1.55}Sc_{0.2}Fe_{3.25})O_{12}$	0.6	0.9

Table 4.1: Overview of the studied magnetic iron garnet films.

4.2 CdTe/CdMgTe Quantum Well Sample

In the last part of this work, see Chapter 7, the studied sample is a cadmium telluride (CdTe) based terneray alloy where a part of the Cd atoms are replaced by magnesium (Mg) atoms. CdTe itself is a direct band gap semiconductor where the band gap ranges from $E_g = 1.606\,\mathrm{eV}$ at low temperature of $T = 4.2\,\mathrm{K}$ down to $E_g = 1.5\,\mathrm{eV}$ at room temperature of $T = 300\,\mathrm{K}$ [Fonthal et al., 2000], and a spin-orbit splitting of $\Delta = 0.871\,\mathrm{eV}$ [Cardona et al., 1988]. It crystallizes in the zincblende structure with a lattice constant of $a = 0.648\,\mathrm{nm}$ at room temperature [Williams et al., 1969]. In general the CdTe semiconductor is widely used for thin film photovoltaic since its band gap is close to the value of about 1.5 eV where they work most efficiently for sun light.

Replacing the cadmium atoms by magnesium atoms reduces the lattice constant (due to the smaller radius of the Mg atoms), which increases the overlap of the atomic orbitals raising the band gap energy. By changing the amount of Mg atoms, the band gap can be tuned over a wide range from the value for zincblende CdTe up to $E_g = 3.5\,\mathrm{eV}$ (zincblende MgTe). For any concentration x of Mg atoms in $\mathrm{Cd}_{1-x}\mathrm{Mg}_x\mathrm{Te}$, the energy gap can be calculated by [Klingshirn, 2004]

$$E_g(x) = (1.5 + 1.7x + 0.3x^2)\,\mathrm{eV}. \tag{4.1}$$

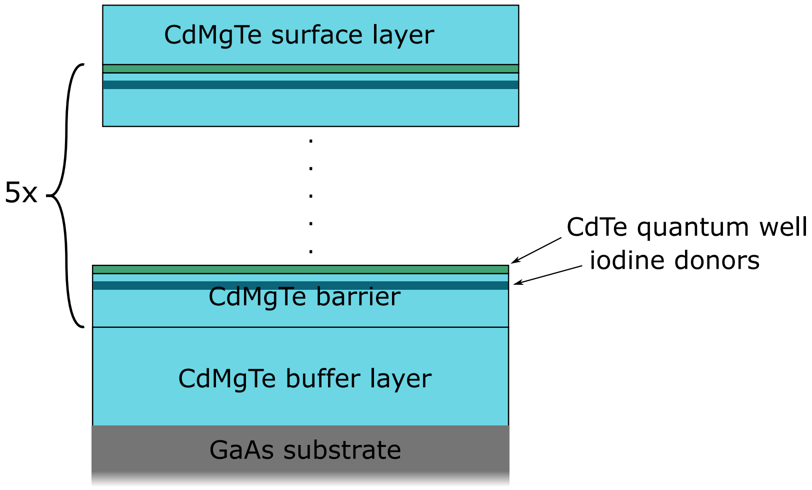

Figure 4.3: Sketch of the CdTe/CdMgTe quantum well sample. It consists of five 20 nm thick QWs of CdTe, surrounded by 110 nm CdMgTe barriers, which contain a 15 nm thick layer doped with iodine donors. The pictures is not to scale.

The sample studied in this work is a CdTe/CdMgTe heterostructure quantum well, shown schematically in Fig. 4.3. It was grown by molecular-beam epitaxy [Herman and Sitter, 1996] on a (100)-oriented GaAs substrate followed by a 2 µm-thick buffer layer of CdMgTe. The heterostructure consists of five periods where each of them is built up by a 110 nm thick CdMgTe barrier and a 20 nm thick CdTe quantum well (QW). The barriers contain a 15 nm thick layer, which is doped with iodine donors, separated by a 15 nm thick spacer from the quantum well. On top of the sample an additional 110 nm thick surface barrier of CdMgTe was grown to reduce contribution of surface charges. Electrons from the barrier donors collect in the CdTe QW and provide a two-dimensional electron gas (2DEG) with a low density of about $n_e \approx 1 \times 10^{10}\,\mathrm{cm}^{-2}$. In all layers made of CdMgTe the magnesium concentration is $x = 0.22$, therefore the investigated sample is a CdTe/$\mathrm{Cd_{0.78}Mg_{0.22}Te}$ quantum well. For measurements in transmission geometry the GaAs would absorb the incident laser light. Therefore, the sample was placed on a glass plate and the GaAs substrate removed by mechanical and chemical etching.

5 Magnetization Precession in Iron Garnet Films

This chapter presents the results from the studies on the magnetization precession in the iron garnet samples. It can be divided into three main sections. Section 5.1 shows the characterization measurements via the magneto-optical Kerr effect for the longitudinal and the polar geometry, which give an insight into the anisotropy of each sample. In section 5.2 we present the results of the optical excitation of the magnetization precession triggered by the inverse Faraday effect (see section 2.2.1). If we excite with a relatively short pulse interval compared to the lifetime of the magnetization precession, resonant excitation is possible. Then, the precession amplitude exhibit maxima and minima for different H_{ext}, where the contrast depends on the quality factor Q of the excited mode. And finally, in Section 5.3 we show the results from investigating the influence of the temperature on the precession, namely for decreasing it from room temperature down to cryogenic temperatures of about 10 K.

5.1 Magneto-Optical Measurements

The magneto-optical Kerr effect (MOKE) was measured in the polar and longitudinal geometry, see Sec. 3.1.1. The results for the polar geometry on sample-A are shown in Fig. 5.1 with both Kerr rotation and ellipticity measurements (red and blue lines, respectively). Obviously, both methods give the same information, so for the following results it is sufficient to show only the results of one method. The measurements in the longitudinal geometry are displayed in Fig. 5.2. The Kerr effect, which is shown as the y-axis in each plot, is proportional to the magnetization $M = |\mathbf{M}|$ of the sample.

In the polar geometry, the value of the Kerr effect and therefore the value of the magnetization M depends linearly on the field strength of the externally applied magnetic field H_{ext} for values from $H_{\text{ext}} = -1.0\,\text{kOe}$ until $+1.0\,\text{kOe}$. Afterwards the effect remains at the maximum level. This is the point at which the sample is fully magnetized at saturation magnetization M_s. However, in the longitudinal geometry, M approaches the maximum level asymptotically and reaches M_s when $H_{\text{ext}} \approx 0.8\,\text{kOe}$ is applied. Consequently, the *easy axis* for magnetization lies in the surface plane of the sample film, while the *hard axis* is perpendicular. For magnetization along the easy axis a small hysteresis of a few tens of Oersted is visible.

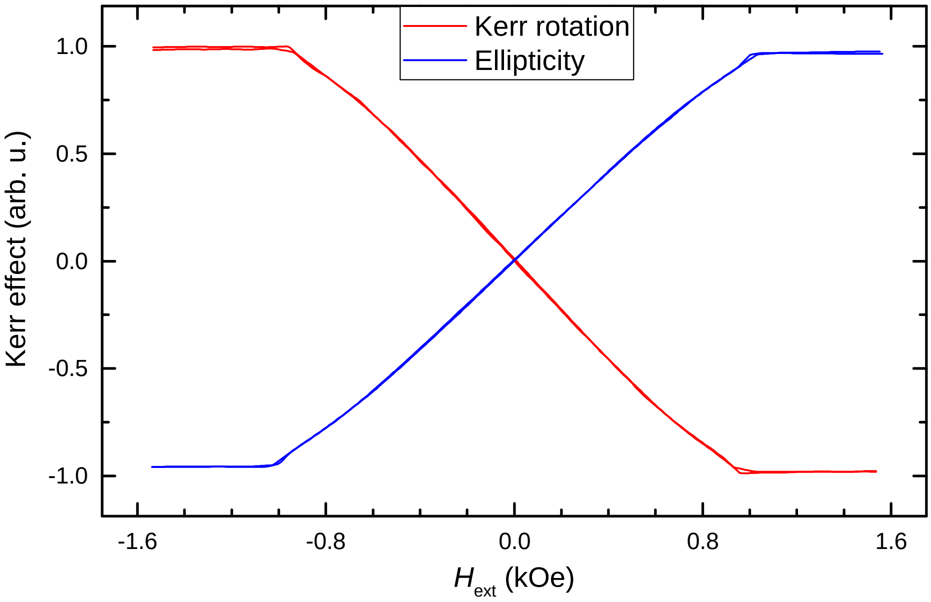

Figure 5.1: PMOKE signal of sample-A. Red line is Kerr rotation, blue line ellipticity signal. Both directions, for increasing and decreasing H_{ext} were measured, no hysteresis is visible. For $H_{\text{ext}} = 1.0\,\text{kOe}$ the sample is fully magnetized in the out-of-plane direction.

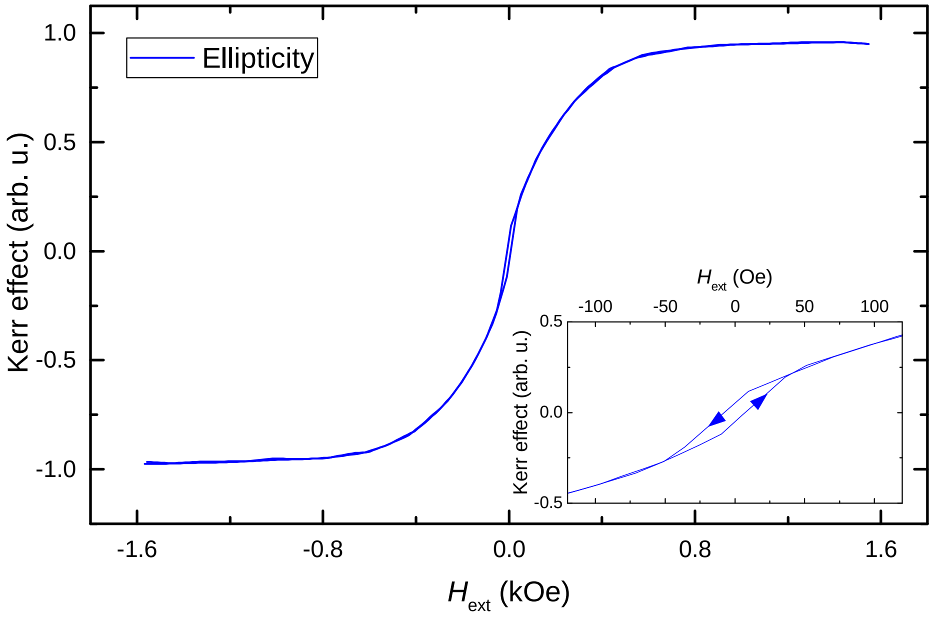

Figure 5.2: LMOKE signal of sample-A. Only ellipticity was measured (blue line). The inset shows a zoom of the same signal for a smaller H_{ext} range. The arrows indicate the direction of sweeping H_{ext}, a small hysteresis from $\pm 40\,\text{Oe}$ is visible. For $H_{\text{ext}} = 0.8\,\text{kOe}$ the sample is fully magnetized along the surface plane.

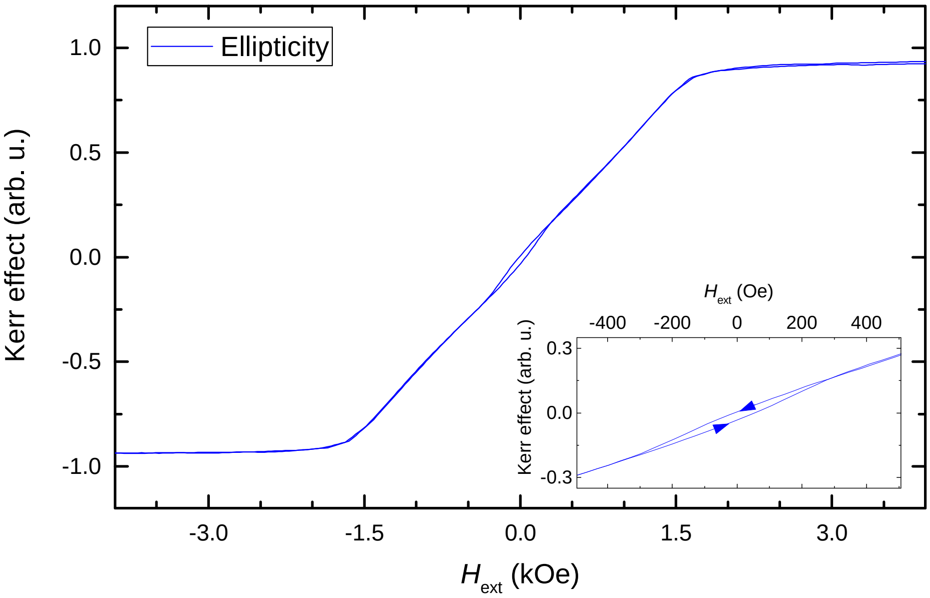

Figure 5.3: PMOKE signal of sample-B. Only ellipticity was measured (blue lines). The inset shows a zoom of the same signal for a smaller H_{ext} range. The arrows indicate the direction of sweeping H_{ext}. For $H_{\text{ext}} = 1.7\,\text{kOe}$ the sample is fully magnetized along the surface plane.

For sample-B the results are shown in Fig. 5.3 and 5.4 for the polar and the longitudinal geometry, respectively. The results are qualitatively the same as for sample-A, the easy axis of magnetization is in-plane of the film and the hard axis perpendicular to it. But along the easy axis the magnetization is saturated already after around 50 Oe, while along the hard axis it needs $H_{\text{ext}} = 1.7\,\text{kOe}$ to reach M_s.

5.2 Resonant Excitation of Magnetization Precession

Now, let us come to the results of magnetization precession triggered by the IFE, induced by circularly polarized femtosecond laser pulses. In general, the physical mechanisms behind the observed effects is very similar to conventional ferromagnetic resonance (FMR) measurements. In contrast to common pump-probe setups we do not perturb the system when it is in its equilibrium position, but excite it again before the precession can fully decay: excitation by a train of laser pulses. It is strongly connected with Chapter 6, the excitation part is exactly the same, but in this chapter the probing is limited to take place at the same sample position where the pump beam is incident. Thus, only non-propagating effects are studied here.

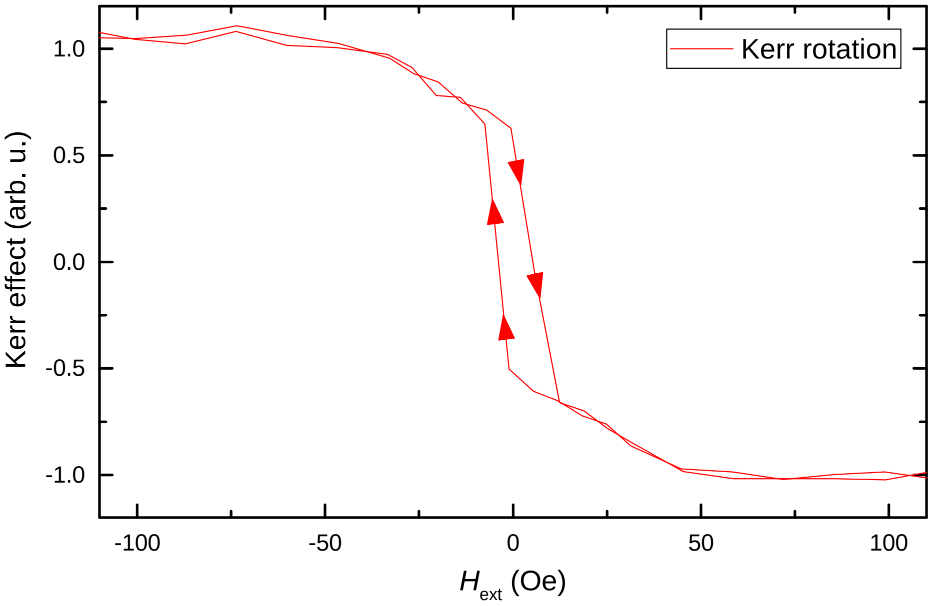

Figure 5.4: LMOKE signal of sample-B. Only Kerr rotation was measured (red lines). The arrows indicate the direction of sweeping H_{ext}. For $H_{\text{ext}} = 50\,\text{Oe}$ the sample is fully magnetized along the surface plane.

5.2.1 Results for Sample-A

Before we investigate the resonant excitation, let us first take a look on the inverse Faraday effect induced by a single laser pulse. For this we excite sample-A with the single pulse setup from Sec. 3.2.2. The measured time-resolved Faraday rotation signals for different external magnetic fields are shown in Fig. 5.5. The colored circles are the measured and averaged Faraday rotation values ϕ_{FR} (calculated from $\Delta U/U_{\text{DC}}$ with Eq. (3.6)) for a ramped time delay t between pump and probe pulse. It is clearly visible that the arrival of the pump pulse at $t = 0$ triggers a sinusoidal oscillation of the magnetization.

For further investigation, the oscillations can be described by a decaying sine function:

$$\theta(t) = \theta_0 e^{-t/\tau} \sin(\omega t + \zeta), \tag{5.1}$$

with the amplitude θ_0, the lifetime τ, the radial frequency ω and the phase ζ. Note that in the entire thesis θ denominates the angle of the magnetization precession while ϕ is used for the FR angle, see also Fig. 5.18. Depending on which kind of plot the function is fitted to, one might have to replace the quantities. All acquired time traces are fitted by this function, see cyan thin lines in Fig. 5.5. The initial phase ζ of the signal is close to zero for all magnetic fields, revealing that the change of magnetization $\Delta\mathbf{M}$ is perpendicular to the propagating probe beam normal to the film plane directly after illumination with the pump beam which then induces an oscillatory movement of $\mathbf{M}$ along the $\pm z$ direction.

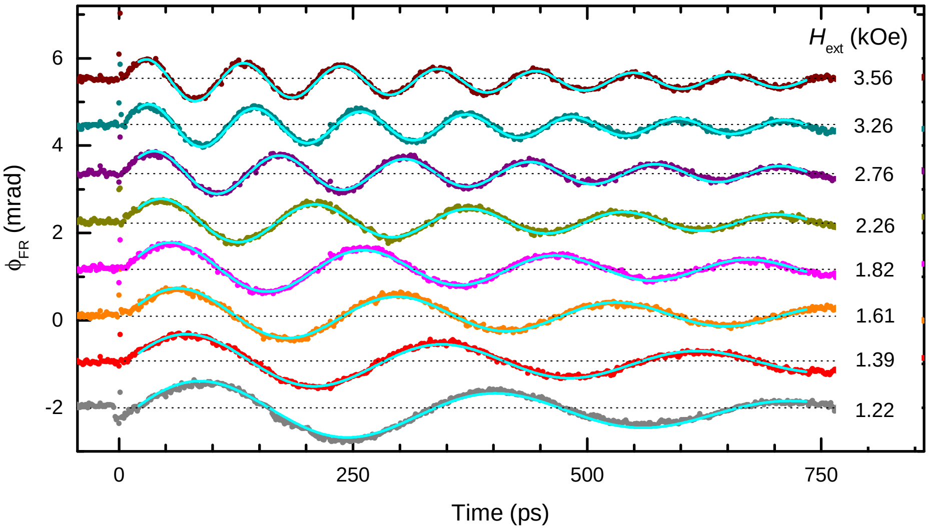

Figure 5.5: Time-resolved Faraday rotation signal (colored circles) for different field strengths of the externally applied magnetic field B_{ext} under low repetition optical excitation. The cyan thin lines are fits with decaying sine functions. Both measured time traces and decaying sine fits are shifted along the y-axis for better visibility.

Plotting the fit parameters ϕ_0 and ω versus the externally applied magnetic field shows a dependency of both from the magnetic field strength H_{ext}, as shown in Fig. 5.6. The precession frequency ω of $\mathbf{M}$ is given by the Kittel formula [Kittel, 1948]:

$$\omega = \gamma\sqrt{BH} \tag{5.2}$$

$$= \gamma\sqrt{(H_{\text{ext}} + 4\pi M_s - H_a)H_{\text{ext}}} \tag{5.3}$$

with γ for the gyromagnetic ratio, $4\pi M_s$ for the saturation magnetization, anisotropy field H_a and the externally applied magnetic field H_{ext}. The solid cyan line in Fig. 5.6 shows a best fit of Eq. (5.3) using $4\pi M_s = 1000\,\text{Oe}$ and $\gamma = 1.76\times10^7\,\text{rad}\,\text{Oe}^{-1}\text{s}^{-1}$, with the resulting fit parameter $H_a = 1102\,\text{Oe}$. For fields high above the anisotropy field, the dependency of the frequency on the external magnetic field is close to linear, thus one can easily adjust the precession frequency by changing the external magnetic field strength. The decrease of ϕ_0 with an increasing magnetic field is expected. However, the lifetime τ of the precession, see Fig. 5.21, remains almost constant when changing H_{ext}.

What is the fundamental physics triggering these magnetization dynamics induced by the femtosecond laser pulses? Possible mechanisms are the inverse magneto-optical effects related to the impulsive stimulated Raman scattering (ISRS), in case of circularly polarized light namely the inverse Faraday effect described in section 2.2.1, induced magnetocrystalline anisotropy, or thermal effects [Kirilyuk et al., 2010; Bossini and Rasing, 2017]. To evaluate this question, we measured the time-resolved Faraday rotation signal on sample-A

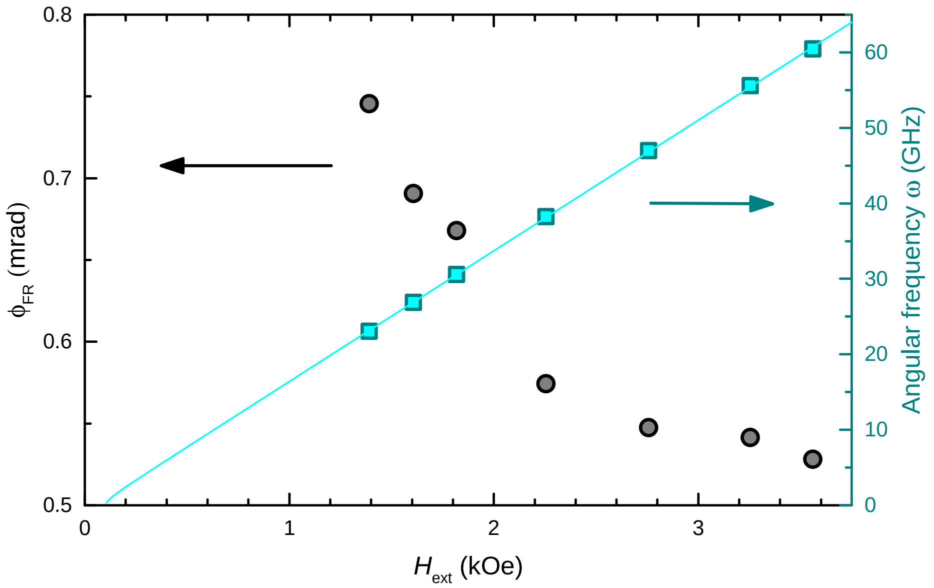

Figure 5.6: Faraday rotation amplitude θ_{FR} (grey circles) and precession frequency f (cyan squares) for the different magnetic fields. The cyan thin line is a best fit of equation (5.3) to the measured data, using $4\pi M_s = 1000\,\mathrm{Oe}$

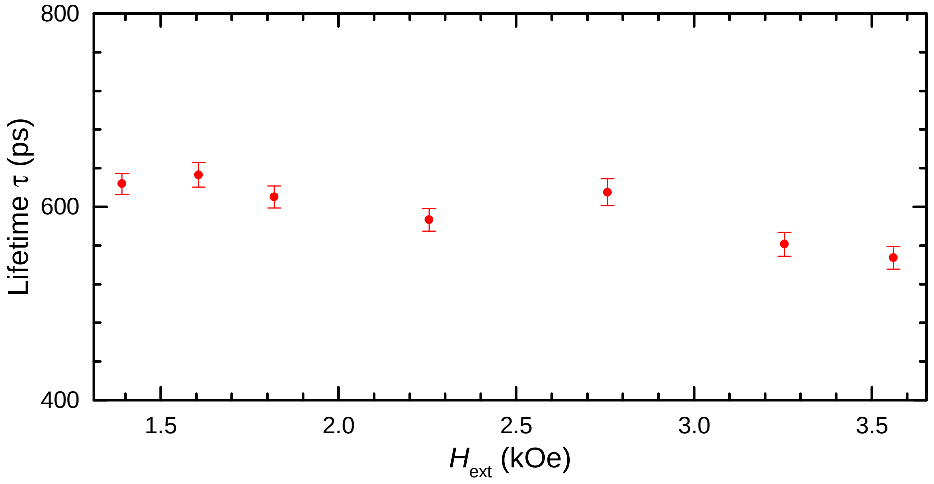

Figure 5.7: Magnetization precession lifetime against H_{ext} with standard deviation. The values show almost no dependency on the magnetic field. Excited by a single pulse.

for opposite helicities and observe a phase shift of π when switching from σ^+ to σ^-, see Fig. 5.8a. Also, there is a direct proportionality between the amplitude of the precession and the pump fluency, see Fig. 5.8b. These are clear evidences that a non-thermal effect is underlying for the triggering mechanism, which is in agreement with the fact that the pump wavelength ($\lambda = 800\,\text{nm}$) is in the range of transparency of all investigated samples with an absorption coefficient of about $90\,\text{cm}^{-1}$, so thermal effects can be neglected in this case. Furthermore, the birefringence is negligibly small for iron garnet films. Summarizing these points leads us to the assumption that the inverse Faraday effect is responsible for the excitation of the magnetization oscillations.

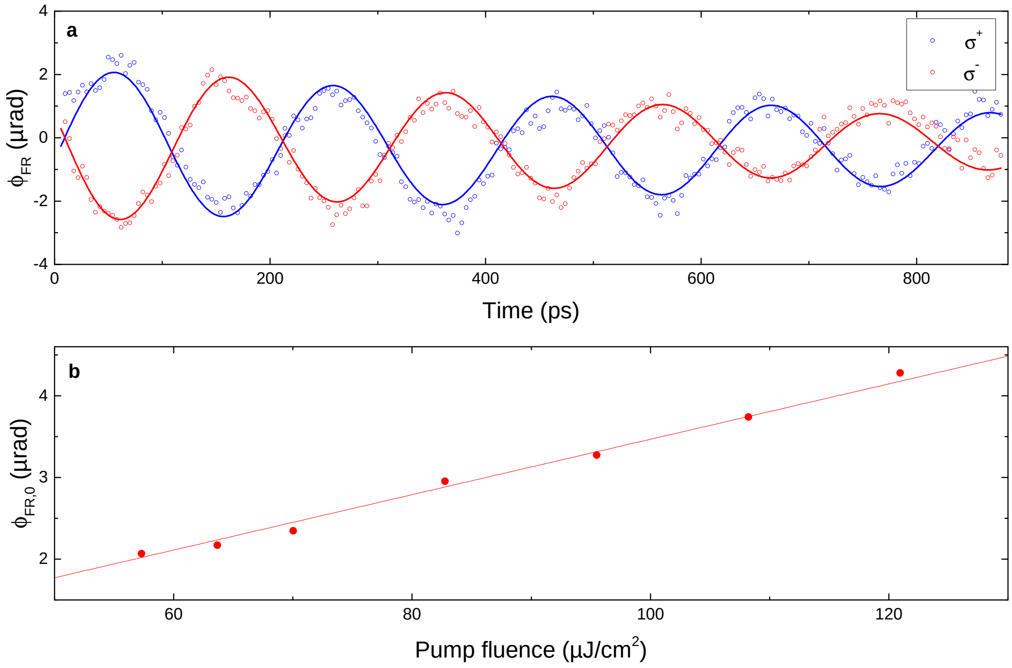

Figure 5.8: (**a**) Time-resolved Faraday rotation for the opposite hellicities σ^+ and σ^- (blue and red circles, respecitvely), which results in a phase shift of π. The solid lines are fits with the decaying sine function from equation (5.1). (**b**) The amplitude of the oscillations for different pump fluences, increasing linearly. The solid line is a linear fit to the measured data points. Concluding, these are clear evidences that a non-thermal effect is underlying for the triggering mechanism. $H_{\text{ext}} = 1.73\,\text{kOe}$ in both figures.

A change of the externally applied magnetic field H_{ext} modifies the frequency ω of the magnetization oscillations, as shown in Fig. 5.6. Using the setup with the high repetition rate, i.e. exciting the precession by a train of laser pulses, should also modify the amplitude θ_0 and phase ζ when changing H_{ext}. But first of all, let us take a look at the results with this setup for one fixed magnetic field of $H_{\text{ext}} = 2.04\,\text{kOe}$, see Fig. 5.9. At a time delay of $0\,\text{ps}$ one pump pulse is incident, triggering the decaying precession of $\mathbf{M}$. After $t \approx 1000\,\text{ps}$, when the next pump pulse is incident, the precession has not fully decayed and for each impinging pump pulse $\mathbf{M}$ is not in its equilibrium position but $d\mathbf{M}/dt \neq 0$. Depending on the phase of the precession, its amplitude should be increased or decreased compared to a single-pulse excitation. The FR signal is periodic with a period of $T_{\text{Rep}} = 1/F_{\text{Rep}}$.

Sweeping H_{ext} over a wide range of several kilo-Oersted reveals cases where the amplitude shows resonances with maximal values and anti-resonance cases with minimal values, as it is visible for selected acquired time traces in Fig. 5.10a with maximal and minimal values of θ_0 and in the 2D color plot in Fig. 5.10b, where maxima are visible for fields with highest blue-red contrast and minima for the weakest contrast.[a]

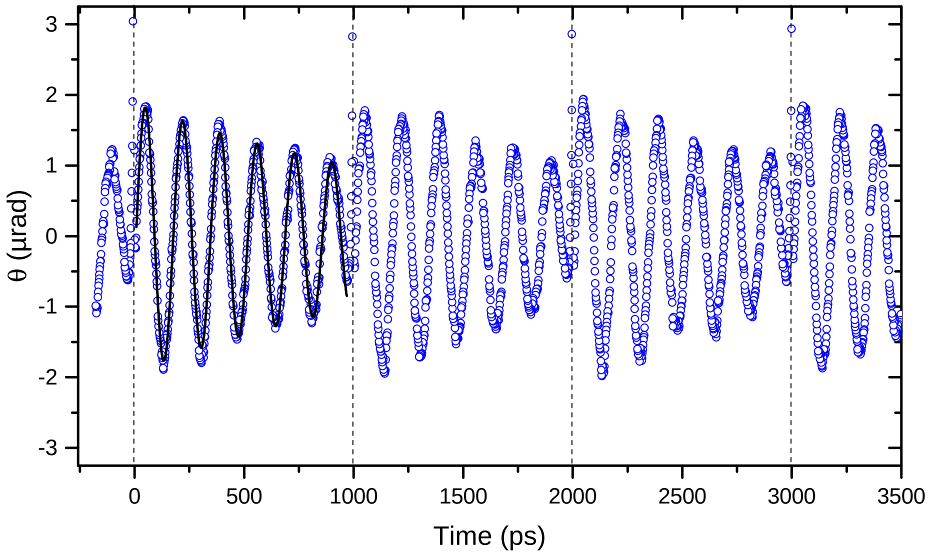

Figure 5.9: Magnetization precession (blue symbols) excited by the high repetition rate laser system acquired for a time window containing several impinging pump pulses. It is clearly visible that the excited precession is still ongoing when the next pump pulse is incident and therefore, the laser pulses do not excite the system out of its equilibrium position. Pump pulses were σ^+ polarized, external magnetic field $H_{\text{ext}} = 2.04\,\text{kOe}$. The black solid line is the best fit of a decaying sine function to the experimental data.

Fitting the decaying sine from Eq. (5.1) to each measured time trace for the different H_{ext} values (cyan solid lines in Fig. 5.10a, small deviations from the measured data are caused by excitation of spin waves) and extracting the fit parameter θ_0 shows a strong dependency on the external magnetic field strength, see Fig. 5.11. Strikingly, the amplitude shows maxima

---

[a] The y-axis of Fig. 5.10a and the color code of Fig. 5.10b gives the magnetization angle θ_0, calculated from the Faraday rotation angle ϕ with equation (3.12), as from here on all plots for magnetization oscillations will show this quantity.

at these fields where the precession frequency is an integer multiple of the laser repetition rate $F_{\mathrm{Rep}} = 1\,\mathrm{GHz}$ corresponding to the following resonance condition:

$$\frac{\omega}{2\pi} = N F_{\mathrm{Rep}}; \qquad N \text{ is integer.} \tag{5.4}$$

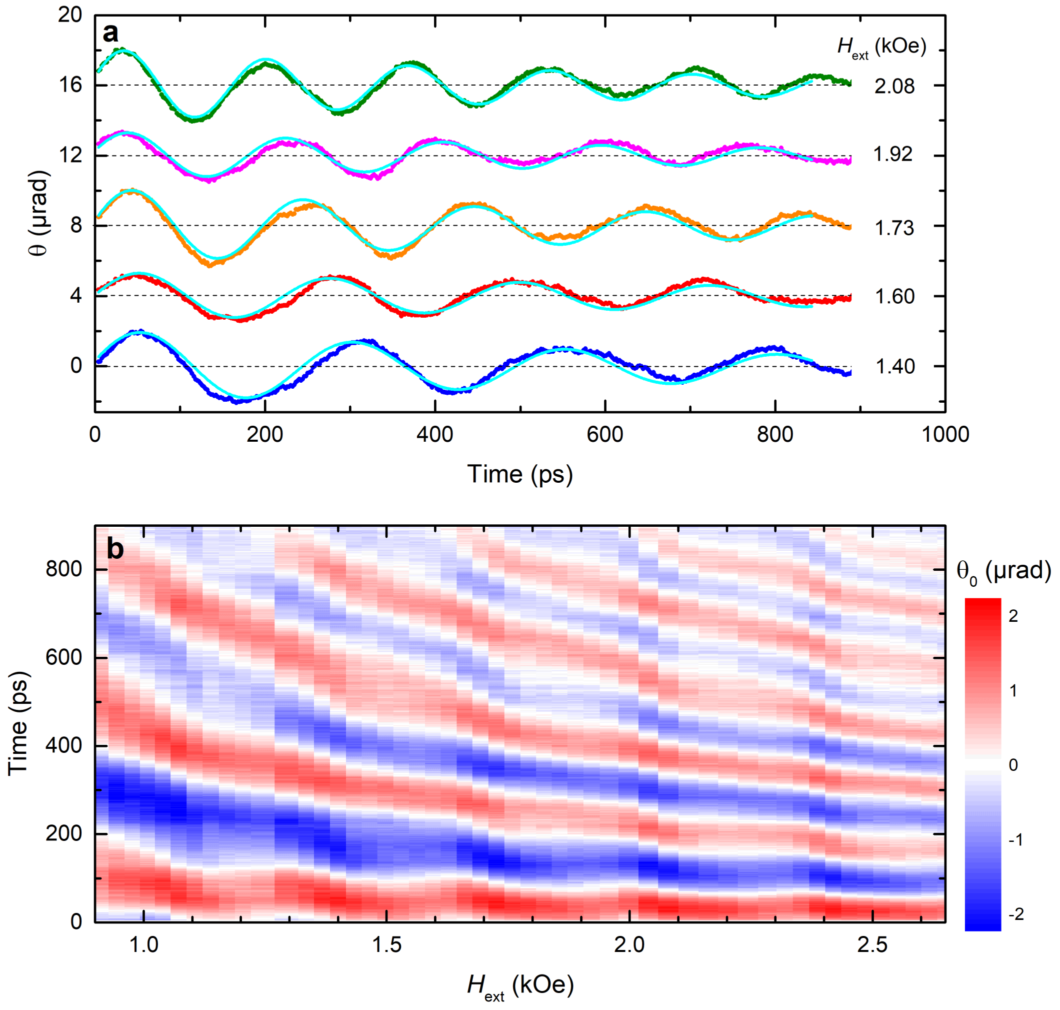

Figure 5.10: Magnetization oscillations under high repetition excitation. (**a**) Selected measured time traces (colored symbols) for different magnetic fields corresponding to maximal and minimal amplitude, i.e. resonance and anti-resonance cases. The thin cyan lines are best fits of decaying sine functions to experimental data. (**b**) Color plot for magnetic field scan. Increasing oscillation frequency for increasing magnetic field is clearly visible. At some magnetic fields the contrast, i.e. the amplitude of the oscillation, is higher, which occurs when resonance condition for the excitation of magnetization precession is achieved.

Consequently, for $N = 4, 5, 6$, and 7, the resonances appear at $H_{\mathrm{ext}} = 1.40$, 1.73, 2.08, and 2.43 kOe, respectively. In such resonance cases, θ_0 exceeds its minimal value (in the anti-resonance case for $N + 1/2$ on the right hand side of Eq. (5.4)) by around 60 %. The FWHM (full width at half maximum) of the resonance lines is about 130 Oe. Also, in the resonance cases the phase ζ is vanishing, see blue, orange and green time traces in Fig. 5.10a. This means that there is no phase shift, which results from spin synchronization: The oscillations from each excitation cycle are synchronized with each other, or in other words, the precession triggered by one laser pulse is in phase with the previous, still ongoing precession, which implies the resonance condition from equation (5.4).

When taking a look at the lifetime τ of the excited mode, see Fig. 5.7, we see that it is roughly in the same order as the seperation $T_{\mathrm{Rep}} = 1$ ns of two subsequent pump laser pulses. Due to this relatively short lifetime one oscillation is damped to < 30 % after 1 ns and close to zero after 2 ns (see equation 5.1). Thus, the resonant pumping with 1 GHz has a low efficiency for the case of sample-A .

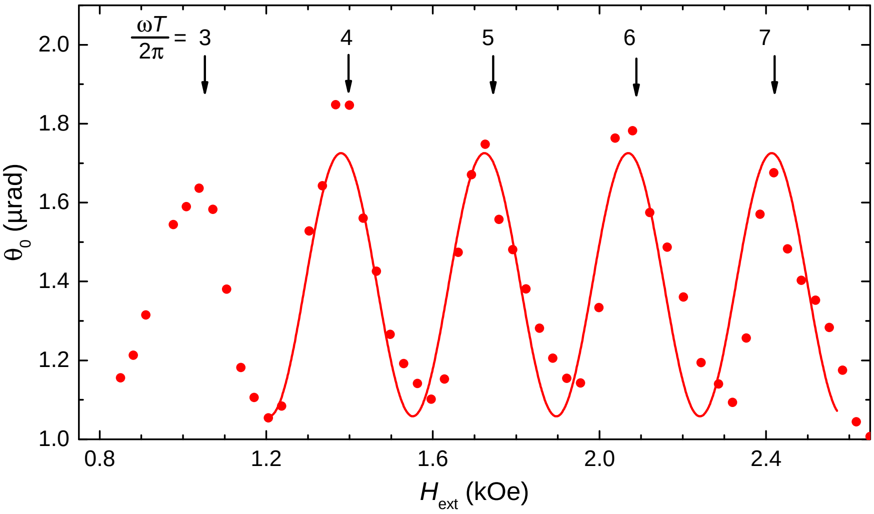

Figure 5.11: Measured precession amplitude θ_0 vs external magnetic field strength H_{ext} (filled circles). The solid curve is a best fit of equation (5.18) to the experimental data, with resulting fit parameter $\tau = 0.70 \pm 0.04$ ns.

5.2.2 Results for Sample-B

It is obvious from the results of the previous section, that modes with a longer lifetime τ would be amplified more efficiently by resonant excitation. Pumping the iron garnet sample-B reveals for all magnetic fields a fast decaying mode, termed mode-1 from here on, with a lifetime significantly below 1 ns, and therefore, the influence on its amplitude is negligible, see red, orange and pink traces in Fig. 5.12.

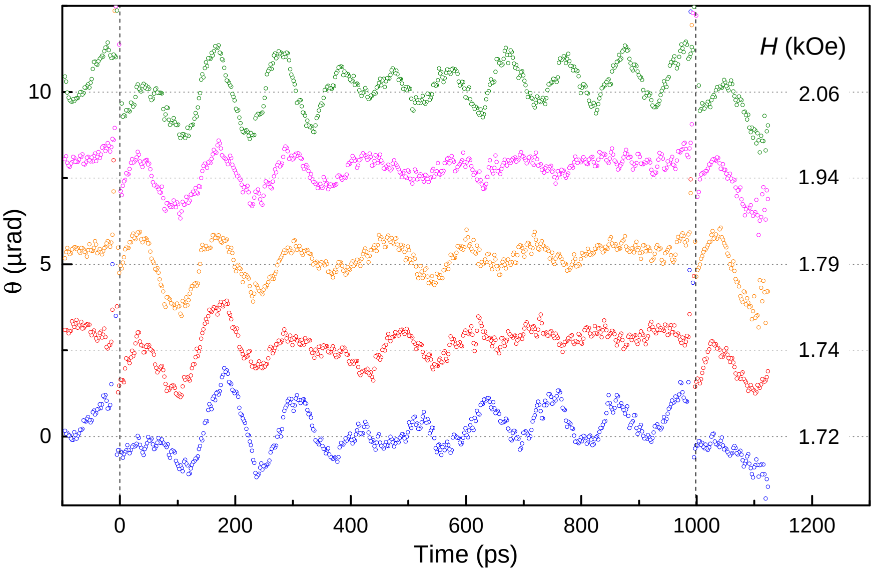

Figure 5.12: Magnetization oscillations in sample-B for different magnetic fields. Two modes are observed: a relatively fast decaying one, visible for all magnetic fields, and a long living mode, detectable only under resonant excitation when resonance condition (eq. (5.4)) is fulfilled, here at $H = 1.72\,\mathrm{kOe}$ and $2.06\,\mathrm{kOe}$, where a beating of both modes is visible. The dashed vertical lines indicate the incident pump pulses.

However, for some magnetic fields, e.g. $H_{\mathrm{ext}} = 1.72\,\mathrm{kOe}$ and $2.06\,\mathrm{kOe}$, additionally a much slower decaying mode (we will call it mode-2) is clearly identified for time delays larger than 700 ps, when mode-1 is almost completely damped. This mode is only detectable for resonant magnetic fields, disappearing even at a small detuning of H_{ext}, compare the time traces at $H_{\mathrm{ext}} = 1.72\,\mathrm{kOe}$ and $1.74\,\mathrm{kOe}$. At these resonant fields a beating of both modes is visible for time delays smaller than 700 ps. To isolate mode-2 from mode-1, one can subtract the signals at slightly off-resonant fields from the resonant signals. Four extracted consecutive resonances of mode-2 for $N = 8$, 9, 10, and 11 are shown in Fig. 5.13. The oscillations are fitted with a decaying sine function, analog to section 5.2.1. In the time window of 1 ns between two subsequent pump pulses no decay is visible, indicating a lifetime τ of more than 3 ns.

Once again the amplitude of the oscillations is extracted for each acquired time trace while scanning the external magnetic field. Due to its long lifetime, the amplitude of mode-2 is changing much more prominently than of mode-1 or the excited mode in sample-A, see Fig. 5.14. In the resonance case, i.e. when the precession frequency is an integer multiple of the excitation frequency, the amplitude is four times higher than the noise level and comparable to the mode-1 amplitude. A small detuning of the external magnetic field strength away from the resonance position lets the amplitude decrease strongly and it gets smaller than the noise level quickly, thus becoming not detectable anymore. When the magnetization precession

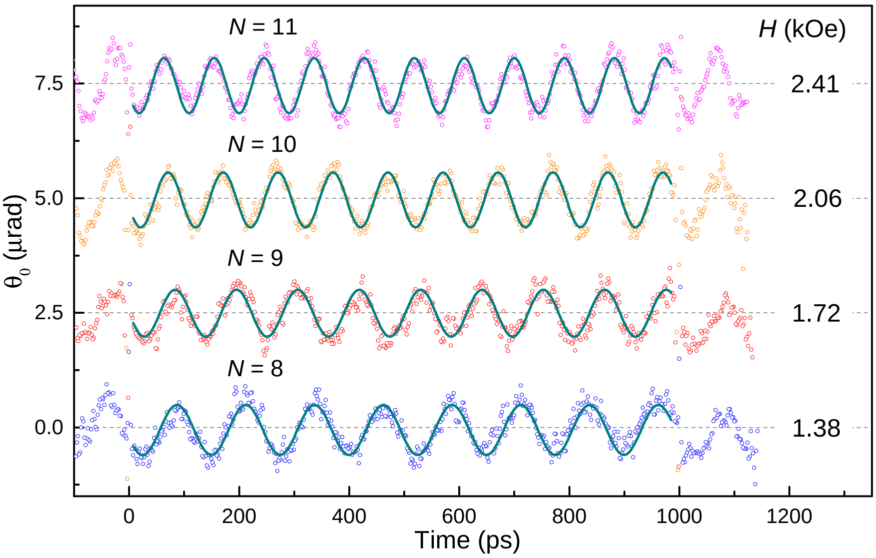

Figure 5.13: Isolated resonances of the slowly decaying mode-2 at different magnetic fields H_{ext}. The cyan solid lines are best fits of decaying sine function to the experimental data.

is excited at a much lower repetition rate of $F_{\text{Rep}} = 80\,\text{MHz}$ (performed by colleagues at Lomonosov Moscow State University, Russia), which can be considered as a single-pulse excitation, mode-2 has such a small amplitude that it cannot be resolved at all. Only under resonant excitation this mode gets amplified to a level high enough to be detectable.

5.2.3 Results for Sample-C

Pumping sample-C with circularly polarized light shows no time dependent Faraday rotation signal for most H_{ext}. As in sample-A, there is just one mode visible. However, only when matching the resonance condition from Eq. (5.4) very precisely, an oscillatory signal is traceable within a small range of just a few Oersted, see selected curves in Fig. 5.15. For a higher detuning the signal becomes quickly smaller than the noise level. Similar to the behavior of mode-2 in sample-B, the excited magnetic precession has a lifetime of significantly more than 1 ns. This leads to a large amplification of the precession amplitude when excited resonantly and to sharp resonance lines, see Fig. 5.16 for the first three resonances and Fig. 5.17 for a closer look to the second resonance line. Due to the long lifetime, several modes from the subsequent pump pulses are excited at the same time. A small detuning of the external field from the resonance value leads quickly to a significant phase mismatch of the different excited modes. The magnetic fields where the amplitude θ_0 is at its maximum are $H_{\text{ext}} = 224\,\text{Oe}$, $570\,\text{Oe}$, and $926\,\text{Oe}$ for the first, second and third resonance, respectively.

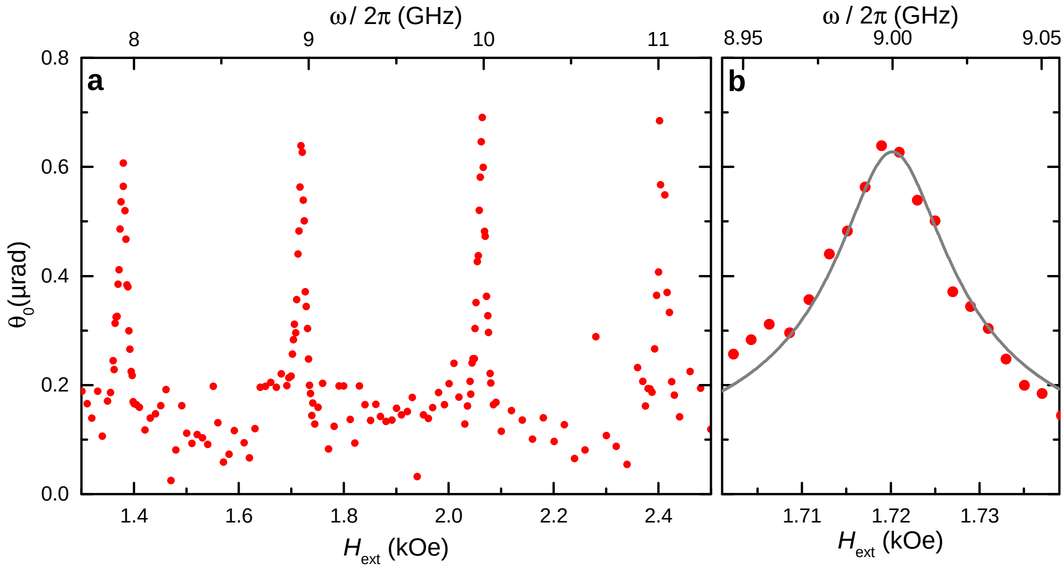

Figure 5.14: Extracted measured amplitudes (circles) of mode-2 in sample-B for different external magnetic fields, (**a**) over a wide range from $H_{\text{ext}} = 1.30 - 2.50\,\text{kOe}$ and (**b**) of the ninth resonance around $H_{\text{ext}} = 1.72\,\text{kOe}$ with a best fit of Eq. (5.17) to the experimental data (grey line), giving $\tau_{\text{B,fit}} = (8.9 \pm 0.5)\,\text{ns}$. Both figures have the same y-axis scale. Due to its long lifetime it has sharp resonance lines, where the value of the precession amplitude in resonance case is five times higher than the noise level.

Remarkably, due to lower saturation magnetization, the precession is excited efficiently even for small external magnetic fields of a few hundred Oersted, which allows the excitation of the first harmonic resonances ($N = 1$ in Eq. (5.4)) in this sample, see grey curve in Fig. 5.15.

5.2.4 Analysis of the Observed Phenomena

For a quantitative understanding of the observed phenomena, a closer look to the dynamical equation for the magnetization is helpful. In general, incident laser pulses excite the inverse Faraday effect causing a spatial and temporal pattern of the magnetization $\mathbf{M} = \mathbf{M}(\mathbf{r}, t)$. The dynamics triggered by the optical excitation are governed by the Landau-Lifshitz-Gilbert equation, see equation 2.16. In spherical coordinates they are:

$$\begin{cases} \sin\vartheta \frac{\partial\vartheta}{\partial t} = -\frac{\gamma}{M}\frac{\delta U}{\delta\varphi} - \alpha\sin^2\vartheta\frac{\partial\varphi}{\partial t} \\ \sin\vartheta \frac{\partial\varphi}{\partial t} = \frac{\gamma}{M}\frac{\delta U}{\delta\vartheta} + \alpha\frac{\partial\vartheta}{\partial t}, \end{cases} \tag{5.5}$$

with the spherical coordinates ϑ and φ and the internal energy U consisting of the sum of the Zeeman energy due to the external magnetic field $U_H = -HM\sin\vartheta\cos\varphi$, the demagnetizing

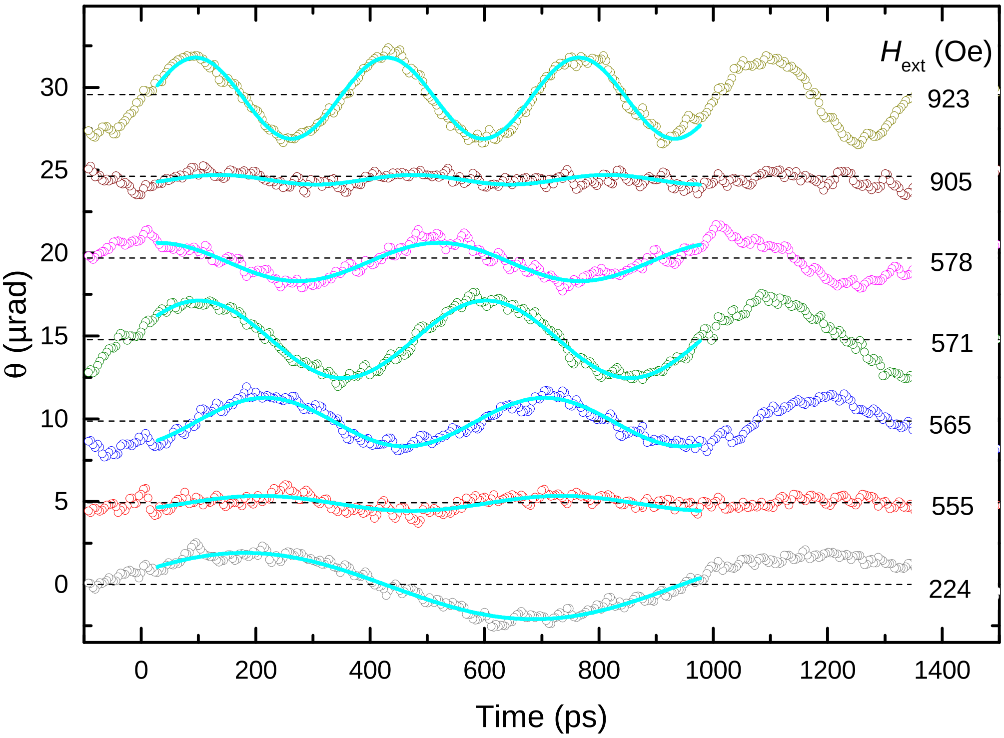

Figure 5.15: Magnetization oscillations in sample-C for different selected external magnetic fields H_{ext} (open circles) and sine fits (cyan solid curves). The oscillations appear only when their frequency match the resonance condition (Eq. (5.4)) very well. The amplitude decreases quickly even for small detuning of H_{ext} of a few Oersted (compare green and red curve).

energy $U_m = 2\pi M^2 \cos^2\vartheta$, the energy from the uniaxial anisotropy $U_{ua} = -K_u \cos^2\vartheta$ (K_u for the uniaxial anisotropy constant, and we assume the cubic energy to be zero), and from the induced inverse Faraday effect $U_F = -H_F(t)M(\sin\beta\sin\vartheta\cos\varphi - \cos\beta\cos\vartheta)$. Here, β is the angle under which the propagating pump pulses are transmitted through the magnetic film. All involved angles are shown in Fig. 5.18.

Changing from the polar angle ϑ to the angle of magnetization deflection $\theta = \pi/2 - \vartheta$ and taking into account the smallness of the angles ($\theta, \varphi \ll 1$), gets us for the Landau Lifshitz Gilbert equation:

$$\begin{cases} \frac{\partial\theta}{\partial t} - \alpha\frac{\partial\varphi}{\partial t} & = \gamma[H + H_F(t)\sin\beta]\varphi \\ \frac{\partial\varphi}{\partial t} + \alpha\frac{\partial\theta}{\partial t} & = -\gamma[H_e + H_F(t)\sin\beta]\theta + \gamma H_F(t)\cos\beta,, \end{cases} \tag{5.6}$$

where $H_e = H + 4\pi M_z - H_a$, with $H_a = 2K_u/M$.

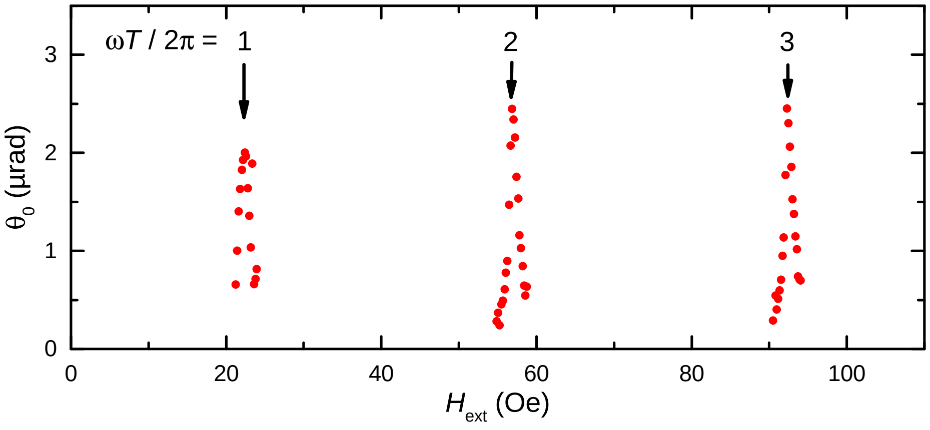

Figure 5.16: Extracted measured precession amplitudes for different external magnetic fields in sample-C. Due to the long lifetime of the excited mode, it exhibits sharp resonance lines with a large amplification of the amplitude. The first three resonances occur at $H_{\text{ext}} = 224\,\text{Oe}$, $570\,\text{Oe}$, and $926\,\text{Oe}$.

To find a solution for the Eqs. (5.6) we multiply the second line with α and add it to the first line. The result is differentiated and the expression for $\partial\varphi/\partial t$ from the second line of Eqs. (5.6) is applied. This gets us a differential equation of second order for θ which does not depend on φ:

$$\begin{aligned}\left(1+\alpha^2\right)\frac{\partial^2\theta}{\partial t^2} + \alpha\gamma(H + H_e + 2H_F(t)\sin\beta)\frac{\partial\theta}{\partial t} + \gamma^2(H + H_F(t)\sin\beta)(H_e + \\ H_F(t)\sin\beta)\theta = \gamma^2(H + H_F(t)\sin\beta)H_F(t)\cos\beta.\end{aligned} \tag{5.7}$$

Taking into account the smallness of both the Gilbert damping constant α and the magnetic field induced by the inverse Faraday effect $H_F(t)$ gives us:

$$\begin{cases}\frac{\partial^2\theta}{\partial t^2} + \alpha(\omega_H + \omega_e)\frac{\partial\theta}{\partial t} + (\omega_H + \omega_{F\perp}(t))(\omega_e + \omega_{F\perp}(t))\theta = \omega_H\omega_{F\|}(t) \\ \frac{\partial\varphi}{\partial t} = -\alpha\frac{\partial\theta}{\partial t} - (\omega_e + \omega_{F\perp}(t))\theta + \omega_{F\|}(t),\end{cases} \tag{5.8}$$

with $\omega_H = \gamma H$, $\omega_e = \gamma(H + 4\pi M - 2K_u/M)$, $\omega_{F\|} = \gamma H(t)\cos\beta$, and $\omega_{F\perp}(t) = \gamma H_F(t)\sin\beta$.

If the pump beam is parallel to H_{ext} ($\beta \to \pi/2$) and magnetic losses are neglected, the first line of Eqs. (5.8) becomes isomorphic to the Schrödinger equation with a periodic potential $V(t) = -\gamma H_F(t)(\omega_0 + \omega_e)$. The problem can now be reduced to the Kronig-Penney model with eigenfrequencies $\omega_0\omega_e$. If $H_F(t)$ is large enough, the oscillation spectrum exhibits band gaps, which would enable appealing effects such as possible parametric generation of magnetization oscillations.

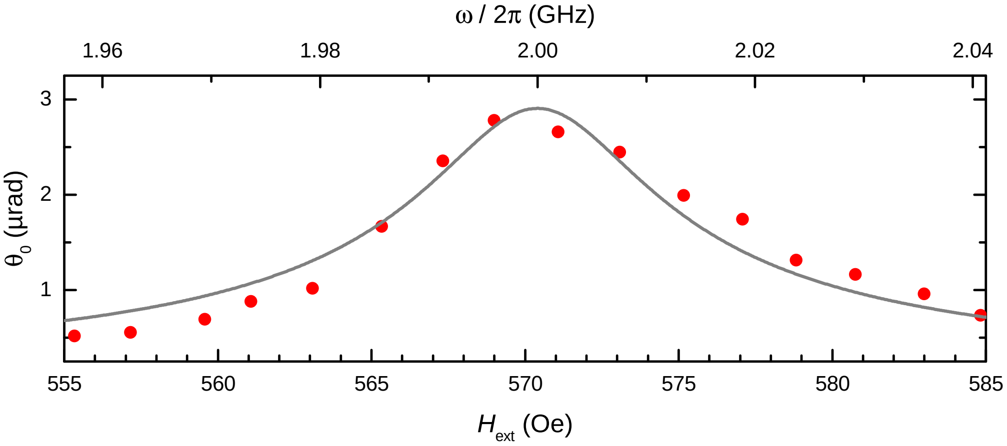

Figure 5.17: Amplitude of magnetization precession in sample-C at the second resonance (circles). The grey solid line is a best fit of Eq. (5.17) to the experimental data, with $\tau_{\mathrm{C,fit}} = (15 \pm 1)\,\mathrm{ns}$.

In our experimental conditions, the pump laser beam propagates through the magnetic film close along to its normal, thus, $\beta \ll 1$. The right hand side of the first line of Eqs. (5.8) becomes prominent and it simplifies to:

$$\frac{\partial^2\theta}{\partial t^2} + \frac{2}{\tau}\frac{\partial\theta}{\partial t} + \omega_0^2\theta = \omega_H\omega_F(t), \tag{5.9}$$

where $\tau = 2/(\alpha(\omega_H+\omega_e))$ and $\omega_0 = \sqrt{\omega_H\omega_e}$. Therefore, the periodic excitation of the inverse Faraday effect acts on the magnetization of the sample as an external periodic force. Since the optical pulse duration is relatively short ($\Delta t \ll T_{\mathrm{Rep}}, \omega_H^{-1}$), we can use the following representation of this external force:

$$\omega_F(t) = \gamma\Delta t h \sum_{m=0}^{+\infty} \delta(t - mT_{\mathrm{Rep}}); \qquad m \text{ is integer}, \tag{5.10}$$

where h is the amplitude of each pulse in H_F. Now the problem can be solved using the Green function formalism:

$$\theta(0) = \frac{1}{\omega}\sum_{m=0}^{\infty} hG(t + mT_{\mathrm{Rep}}), \tag{5.11}$$

with the Green function

$$\begin{cases} G(t) = \omega^{-1}\sin(\omega T_{\mathrm{Rep}})\exp(-t/\tau); & \text{for } t \geq 0 \\ G(t) = 0; & \text{for } t < 0, \end{cases} \tag{5.12}$$

where $\omega = \omega_0\sqrt{1-(\omega\tau)^{-1}} \approx \omega_0$ and $\omega_0 = \sqrt{\omega_H\omega_e}$.

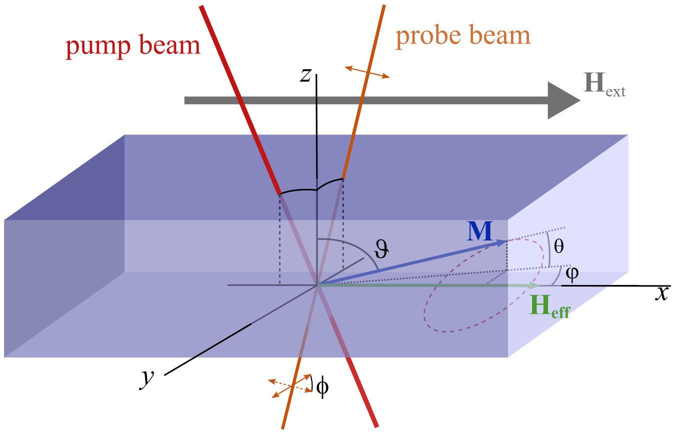

Figure 5.18: Description of involved angles in magnetization precession. ϕ: Faraday rotation angle, ϑ and φ spherical coordinates, θ: magnetization deflection angle.

The inhomogeneous differential equation (5.9) is equal to the driven harmonic oscillator equation. It can be reduced to a second-order homogeneous differential equation with respect to θ with boundary conditions arising from the periodicity of the solution:

$$\begin{cases} \frac{\partial^2\theta}{\partial t^2} + \frac{2}{\tau}\frac{\partial\theta}{\partial t} + \omega_0^2\theta = 0 \\ \theta(0) = \theta(T_{\text{Rep}}) \\ \frac{\partial\theta}{\partial t}(0+) - \frac{\partial\theta}{\partial t}(T_{\text{Rep}}-) = \gamma^2 H h \Delta t. \end{cases} \tag{5.13}$$

The solution of this set of equations can be written in the form:

$$\theta(t) = \theta_0 e^{-t/\tau} \sin(\omega t + \zeta), \tag{5.14}$$

which leads from the boundary conditions from Eqs. (5.13) to the simultaneous equations for the amplitude θ_0 and the phase ζ:

$$\begin{cases} \sin\zeta = e^{-T_{\text{Rep}}/\tau} \sin(\omega T_{\text{Rep}} + \zeta) \\ \theta_0 \left[\cos\zeta - \cos(\omega_{\text{Rep}} T + \zeta) e^{-T_{\text{Rep}}/\tau}\right] = \frac{\gamma^2 H h \Delta t}{\omega}. \end{cases} \tag{5.15}$$

With the trigonometric identity $\sin(a+b) = \sin a \cos b + \cos a \sin b$ one can simplify the expression for the phase to:

$$\tan\zeta = \frac{e^{-T/\tau} \sin\omega T_{\text{Rep}}}{1 - e^{-T/\tau}\cos\omega T_{\text{Rep}}}, \tag{5.16}$$

and with the trigonometric identity $\cos(a+b) = \cos a \cos b + \sin a \sin b$ the expression for the amplitude can be transformed to:

$$\theta_0 = \frac{\gamma^2 H h \Delta t}{\omega} \left(1 - 2e^{-T/\tau} \cos \omega T_{\mathrm{Rep}} + e^{-2T/\tau}\right)^{-1/2} . \tag{5.17}$$

If the separation of the train of pump pulses is large compared to the lifetime of the excited precession such that $e^{-T_{\mathrm{Rep}}/\tau}$ gets small, which is the case for the resonant excitation of sample-A, the denominator of Eq. (5.16) is close to 1, expressions with $e^{-2T_{\mathrm{Rep}}/\tau}$ can be neglected and we can use the Taylor series for $(1-2x)^{-1/2} \approx 1 + x$ for the remaining part of the $(\ldots)^{-1/2}$ term in Eq. (5.17). The equations for ζ and θ_0 can now be simplified to:

$$\begin{cases} \theta_0 = \frac{\gamma^2 H h \Delta t}{\omega} \left(1 + e^{-T_{\mathrm{Rep}}/\tau} \cos \omega T_{\mathrm{Rep}}\right) \\ \zeta = e^{-T/\tau} \sin \omega T. \end{cases} \tag{5.18}$$

In accordance with the experimental results, the precession shows a resonance, i.e. the amplitude θ_0 gets to it maximum value when the resonance condition $\omega T_{\mathrm{Rep}} = 2\pi N$ (N is integer) is fulfilled, cf. Eq. (5.4). For these values of ω the phase is vanishing, which means the oscillations start with $\theta = 0$ after the incident pump pulse. This is in good agreement with the theoretically expected behavior (see text in section 5.2.1) and with the experimental results (see Fig. 5.10).

Comparing the expected precession amplitude calculated by theory equations with the experimentally observed amplitudes shows good agreement as well. For relatively fast decay, so that $T_{\mathrm{Rep}} \geq \tau$, Eqs. 5.18 was fitted to the measured precession amplitudes of the mode excited in sample-A, see Fig. 5.11, giving a lifetime of

$$\tau_A = (0.70 \pm 0.04)\,\mathrm{ns}. \tag{5.19}$$

The mode-2 excited in sample-B and the one mode of sample-C have much longer lifetimes than the pump pulse separation, so Eq. (5.15) is used to properly calculate the precession amplitude, see Fig. 5.14b and 5.17. The red dots represent the experimentally acquired amplitudes for the different H_{ext}, while the grey solid lines are the fitted equations. The values for the lifetimes are:

$$\tau_B = (8.9 \pm 0.5)\,\mathrm{ns}, \tag{5.20}$$

$$\tau_C = (15 \pm 1)\,\mathrm{ns}. \tag{5.21}$$

Eq. (5.15) is shown for different Q factors (solid, colored lines) together with the experimental data from sample-B (open symbols) in Fig. 5.19. With $\tau = 2Q/\omega_0$ it is directly linked to the lifetime of the mode. Obviously, the contrast of the amplitude magnification in the resonance case is higher for large Q. The red line is a best fit to the experimental data with $Q = 230$, smaller values represent smaller contrast, e.g. as it is the case for sample-A.

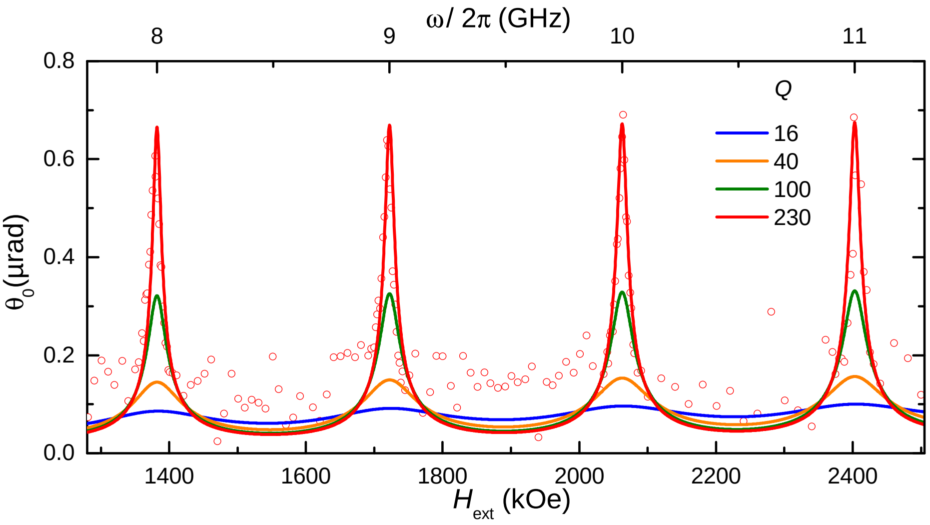

Figure 5.19: Measured precession amplitude in sample-B (open circles) and calculated precession amplitude for modes of different quality factors (solid lines, using Eqs. (5.15)) vs. external magnetic field or the corresponding $\omega/2\pi$, respectively. The red line is a best fit to the experimental data. Different quality factors of the modes mean different values of the lifetime τ, here: 0.6 ns (blue line), 1.5 ns (orange line), 4 ns (green line) and 8.9 ns (red line).

From Eq. (5.17) follows the ratio of the maximal and minimal amplitudes in resonance ($\cos\omega T_{\text{Rep}} = +1$) and anti-resonance case ($\cos\omega T_{\text{Rep}} = -1$), respectively:

$$\theta_{0,\text{max}}/\theta_{0,\text{min}} = \coth\left(\frac{T_{\text{Rep}}}{2\tau}\right) = \tanh\left(\frac{\omega_0 T_{\text{Rep}}}{4Q}\right). \tag{5.22}$$

Consequently, the amplitude is increased most strongly for magnetization modes with a high quality factor, see also Fig. 5.19. Compared to the excitation by a single pulse, the enhancement factor for resonant excitation is given by:

$$\theta_{\text{max}}/\theta_s = \left(1 - e^{-T_{\text{Rep}}/\tau}\right)^{-1}. \tag{5.23}$$

Fitting the experimentally observed data with the theoretical forms gives the lifetimes of the excited magnetization modes

Let us compare the efficiency of the excitation of the magnetization mode in sample-A and the mode-2 in sample-B. The lifetimes for the two magnetization modes are $\tau = 0.70$ ns and $\tau = 8.9$ ns, respectively. This corresponds to enhancement factors of 1.3 and 9.4 compared to the excitation by a single pulse. This huge difference is a key factor of detecting mode-2 in sample-B. By a single pulse, the sample-A mode is excited significantly stronger, however, in the multiple-pulse region mode-2 is enhanced 6.6 times more efficiently than the sample-A mode due to the large difference in their Q factors. As a result, the mode-2 becomes visible as its amplitude gets enhanced to a similar level as the amplitude of the sample-A mode.

5.3 Magnetic Precession at low Temperatures

How does the temperature affect the IFE and its following magnetization precession? All measurements have been performed at room temperature and so far, only the influence of higher temperatures on the oscillatory signal has been investigated [Hansteen et al., 2006]. There, a drop in the precession frequency was observed which they attributed to an increasing magnetocrystalline anisotropy with rising temperature, cf. Eq. (5.3).

We wanted to investigate the influence of lower temperatures on the magnetization precession. For this purpose, sample-A was mounted inside of a liquid helium flow cryostat, see Sec. 3.2.2. The following results were all measured on the low repetition setup with relatively rare pump pulses ($T_{\mathrm{Rep}} \gg \tau$) which can be considered as a single pulse excitation.

The sample temperature T is varied from a low value of $T = 15\,\mathrm{K}$ up to room temperature[b], see Figs. 5.20. Interestingly, at cryogenic temperature of $T = 15\,\mathrm{K}$ the Faraday rotation signal exhibits no oscillatory signal. After the pump pulse hits the sample at zero time, the magnetization is pushed out of its former position, but decays back to the equilibrium position within around 200 ps (Fig. 5.20a). At a slightly higher temperature of $T = 25\,\mathrm{K}$ a very small overshoot is visible after $t = 100\,\mathrm{ps}$ (Fig. 5.20b).

At $T = 60\,\mathrm{K}$ a highly damped but oscillating signal is observed when applying an external magnetic field of $H_{\mathrm{Ext}} = 1.79\,\mathrm{kOe}$ (Fig. 5.20c, green symbols), which is the highest possible value when measuring with the flow cryostat. For smaller values of the external magnetic field, the amplitude of the oscillation decreases: at $H_{\mathrm{Ext}} = 1.22\,\mathrm{kOe}$ (blue symbols) almost no magnetic precession is detected. This might be contributed to a change in the magnetocrystalline anisotropy of the investigated sample when cooling it to considerably lower temperatures. The angle of deflection of the magnetization $\mathbf{M}$ after impinged by the circularly polarized pump pulse is largest when the magnetization is saturated. For room temperature measurements this was the case for fields of $H_{\mathrm{ext}} > 1.0\,\mathrm{kOe}$.

When further increasing the temperature one can clearly see that the difference in the amplitudes between $H_{\mathrm{ext}} = 1.22\,\mathrm{kOe}$ and $1.79\,\mathrm{kOe}$ diminishes. The necessary externally applied magnetic field to saturate the magnetization of the sample decreases with an increase of T, see blue and green symbols in Figs. 5.20d–f.

Besides the amplitudes, the decay time τ of the precession is very much influenced by T, compare the green symbols in Figs. 5.20a–f. The time traces for the highest magnetic field are fitted with a decaying sine function (see Eq. (5.1)), and the parameter τ for the lifetime of the precession is extracted for each temperature and displayed in Fig. 5.21. The room

---

[b] In this section, T denotes in all cases the temperature. In all other parts of this thesis, T is abbreviated for the time period, mainly for the temporal distance between two subsequent pump pulses, which is indicated by the subscript *Rep*.

temperature value comes from the measurements shown in Sec. 5.2. When cooling down the sample, from $T < 250\,\mathrm{K}$ the lifetime drops by one order of magnitude until reaching $T = 25\,\mathrm{K}$. Let us also take a look at the precession frequencies ω for the different T, see Fig. 5.22. It reduces by around 10 % when cooling T from room temperature to 100 K.

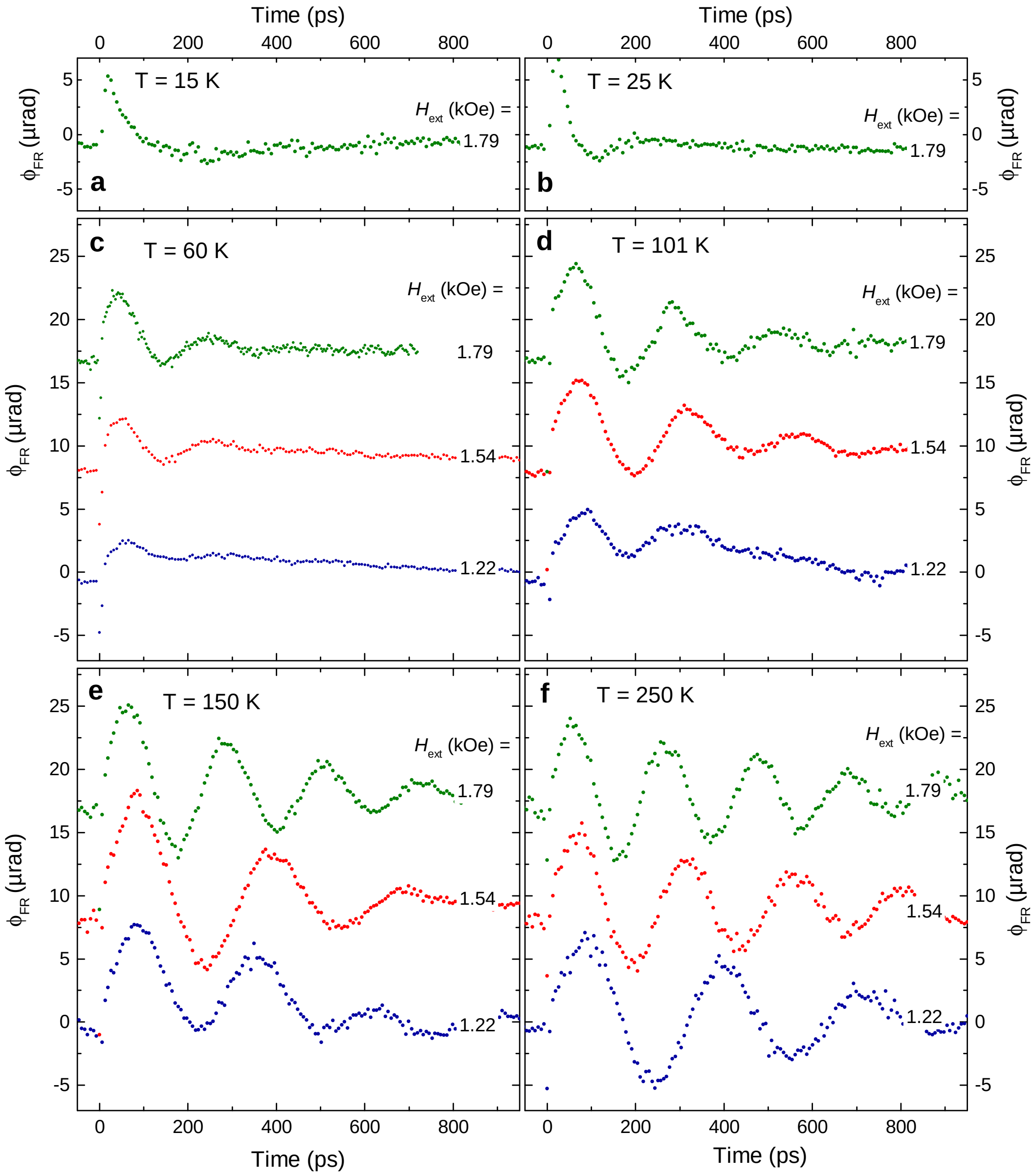

Figure 5.20: Magnetization precession signal for different low temperatures from $T = 15 - 250\,\mathrm{K}$ for different H_{ext}. All measurements were performed on sample-A. It is clearly visible that the lifetime of the precession drops with the temperature.

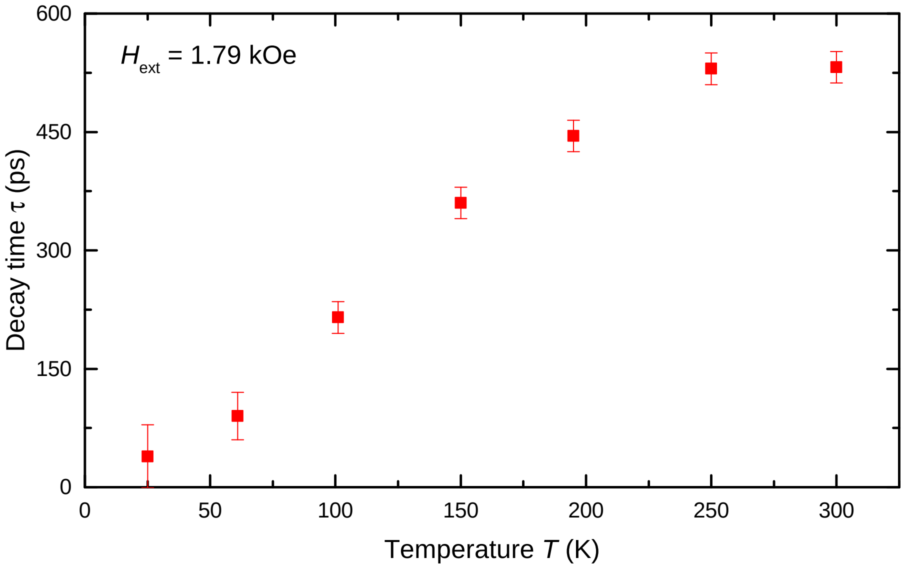

Figure 5.21: Decay time τ against temperature T in sample-A. It drops by one order of magnetitude when decreasing the temperature from about room temperature down to $T = 25\,\mathrm{K}$.

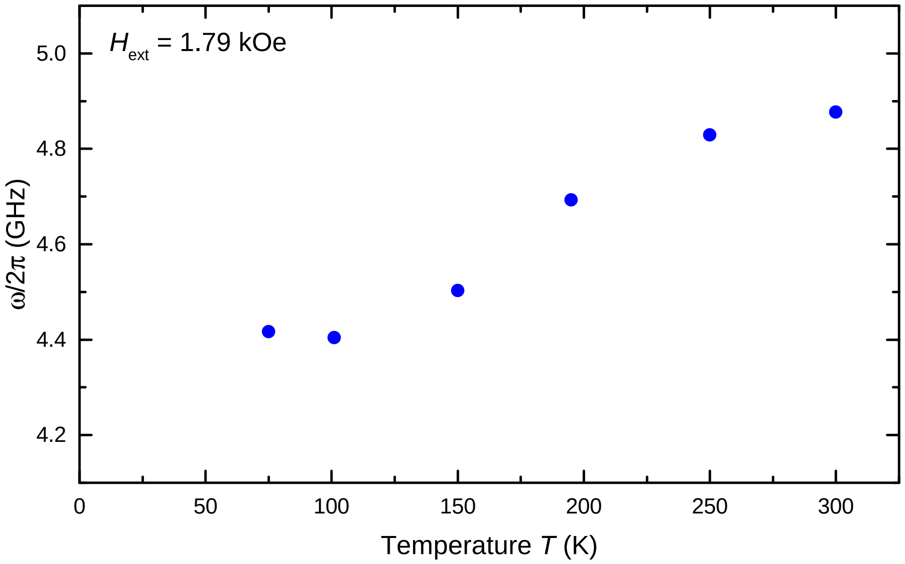

Figure 5.22: Precession frequency ω against temperature T in sample-A. For lower temperatures the frequency drops by around 10 %. An increasing magnetic anisotropy would lead to a decreasing frequency, see Eq. (5.3).

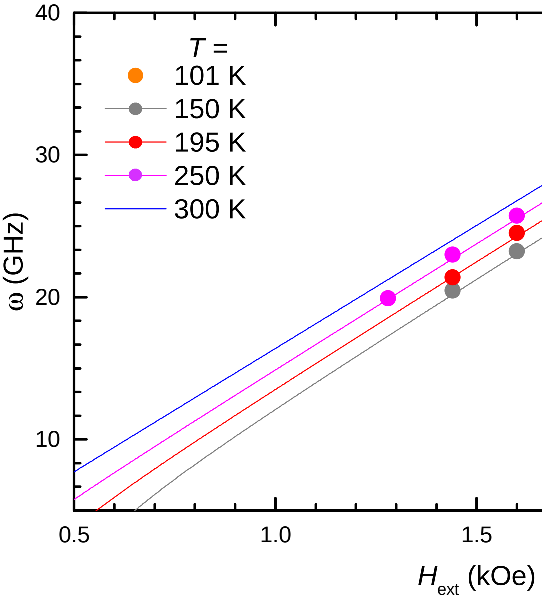

Figure 5.23: Precession frequency against H_{ext} for different T in sample-A. The circles represent experimentally acquired data points, solid lines are best fits using Eq. (5.3). The blue curve is from Fig. 5.6.

Both phenomena, drop of lifetime and frequency when reducing the temperature are possibly contributed due to an increase of the magnetocrystalline anisotropy. To investigate this, let us take a look how the frequency in dependence on H_{ext} changes with the temperature. The fit parameters for the frequency for $T = 101, 150, 195$ and $250\,\text{K}$ are shown in Fig. 5.23 as colored circles. For $T = 101\,\text{K}$ only two data points are available, but to the experimental data points of higher temperatures the Kittel formula in Eq. (5.3) is fitted with the least squares method, shown by the colored solid lines. Since we do not know the saturation magnetization M_s for others than room temperature, we consolidate the unknown terms to $H_{\text{fit}} = 4\pi M_s - H_a$. For the gyromagnetic ratio we used $\gamma = 1.76 \times 10^7\,\text{rad}\,\text{Oe}^{-1}\text{s}^{-1}$ and assumed it is independent on the ambient temperature. The blue line is the Kittel formula for room temperature from Fig. 5.6. The fit parameters for the three investigated temperatures are:

$$H_{\text{fit, 150 K}} = (-527 \pm 23)\,\text{Oe} \tag{5.24}$$

$$H_{\text{fit, 195 K}} = (-411 \pm 20)\,\text{Oe} \tag{5.25}$$

$$H_{\text{fit, 250 K}} = (-285 \pm 22)\,\text{Oe} \tag{5.26}$$

One can clearly see that the term $4\pi M_s - H_a$ is shifted to higher negative values for decreasing temperatures. This is achieved by lowering the saturation magnetization ($M_s > 0$) or increasing the anisotropy field H_a. For decreasing temperatures the saturation magnetization seems to rise (higher values of H_{ext} are necessary to maximize the precession amplitude, compare Figs. 5.20c and f), so this is a clear hint that the magnetocrystalline anisotropy is indeed increased for lower temperatures, which causes a reduction of the decay time of the magnetization precession. But to truely affirm this statement, further investigations on the temperature dependency of the MOKE signal would be necessary.

6 Optical Generation and Detection of Propagating Spin Waves

In this chapter the results of measurements on the generation and propagation of dipolar spin waves (SWs) are presented. Propagating SWs are a direct consequence from the leading mechanism of the previous chapter: circularly polarized femtosecond laser pulses disturb the spin system in a magnetically ordered material. In the previous chapter we were looking at the following precessional motion of the magnetization **M** at the same position of the sample where it got perturbed – or in other words: when pump and probe beams are overlapping. Due to the coupling of the spins (see section 2.1.2 and 2.1.3) the energy of the magnetization precession spreads away, the perturbation of the spin system under the illuminated spot is traveling across the sample. Consequently, the only difference in the experimental technique to the previous chapter is to spatially shift the focused pump and probe beams on the sample surface away from each other. For distances larger than the diameter of the focused laser spots, all the signal which is still measured by the probe beam originates solely from propagating spin waves.

We will start with the results of the measurements on sample-A, where we will see a narrow SW spectrum due to the resonant optical excitation which leads to long propagating distances. Afterwards the results from sample-C will be presented, where the resonant excitation works more efficiently owing to a higher quality factor of the excited mode. Here the train of laser pulses allows the wavelength to be tuned over a wide range by changing one of the setup parameters only slightly.

6.1 Periodic Pumping of SWs: Magnon Cloud (Sample-A)

6.1.1 Experimental Results

Let us start with SW measurements on sample-A. To improve the signals, for all traces the excitation with σ^+ and σ^- polarized light is taken and the difference of both calculated. For the correct values of the precession angle θ the data has to be divided by an additional factor of 2. With this method noise and undesired signal, which does not depend on the pump helicity, are canceling out. The acquiring time of one full signal is doubled then, but for very small signals, as they are for distances of several tens of micrometers, it is a suitable way to improve the signal-to-noise ratio significantly.

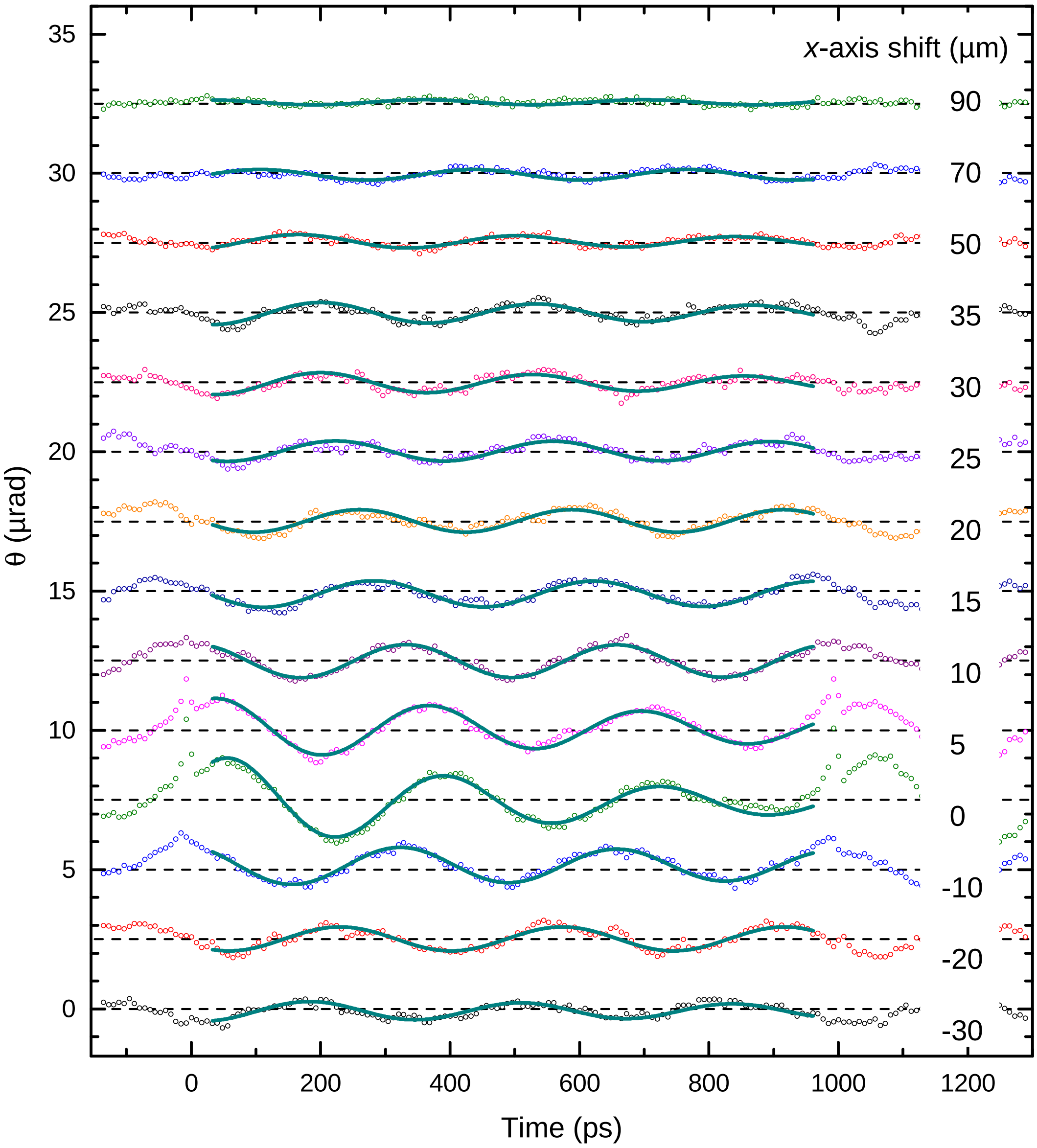

Figure 6.1: Time traces of magnetization oscillations for increasing shift between pump and probe in x-axis direction of sample-A(open circles) and decaying sine fits (cyan solid lines). For distances of up to 70 μm the oscillations are clearly visible and even for 90 μm still resolvable. Time traces are shifted for a better visibility, dashed lines represent $\theta = 0$ for each curve. External magnetic field for all curves: $H_{\text{ext}} = 1.03\,\text{kOe}$.

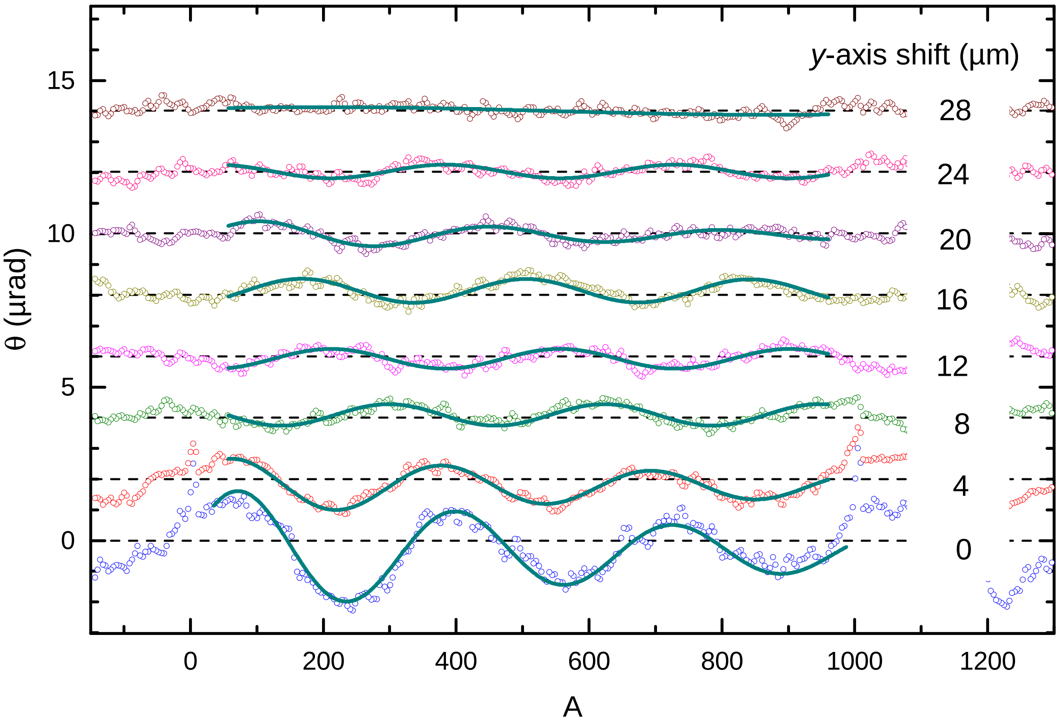

Figure 6.2: Time traces of magnetization oscillations for increasing shift between pump and probe in y-axis direction of sample-A(open circles) and decaying sine fits (cyan solid lines). The amplitude decreases quickly for much lower distances than for shifts in x-axis direction. From 28 μm no oscillation is resolvable anymore. Time traces are shifted for a better visibility, dashed lines represent $\theta = 0$ for each curve. External magnetic field for all curves: $H_{\text{ext}} = 1.03\,\text{kOe}$.

The signals for an increasing shift of pump and probe beams away from each other in $\pm x$ direction, which means along the externally applied magnetic field $\mathbf{H}_{\text{ext}}$, are shown in Fig. 6.1. For the results of the shift along the $y-$axis, see Fig. 6.2. All these time traces were recorded at $H_{\text{ext}} = 1.03\,\text{kOe}$. Between two subsequent pump pulses a decaying sine function (see Eq. (5.1)) is fitted to the experimental data, the calculated fit parameters of the amplitude θ_0 and the decay rate τ^{-1} (the latter only for measurements along the x-axis) are shown in Fig. 6.3.

For distances of 10 μm or more the spike of the impinging pump pulse at $t = 0$ is completely vanished, which means the observed magnetization oscillations originate predominantly from propagating SWs. This is in agreement with the spot radius of $5 - 6\,\mu$m. The amplitude decreases for an increasing shift, but in $\pm x$ direction so slowly, that the signal is still resolvable for distances of up to almost 100 μm, which is twice the propagation distance of SWs when excited by a single pulse[a]. However, along the $y-$axis the amplitudes decrease

---

[a] Measurements for single-pulse excitation performed by colleagues at the Lomonosov State University Moscow in Russia

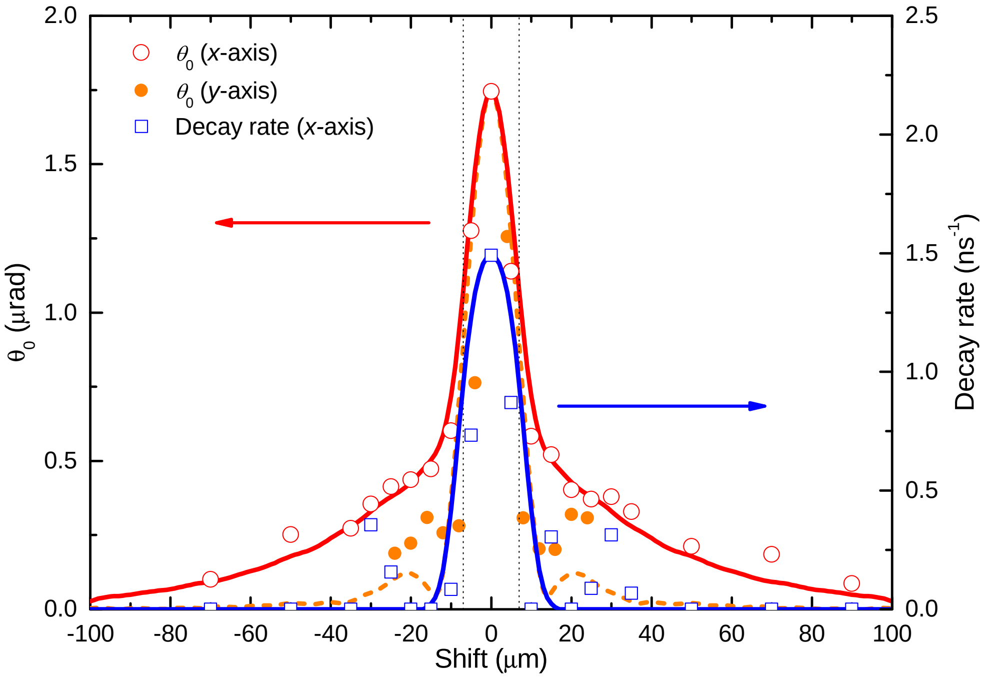

Figure 6.3: Amplitude (red and orange circles) and decay rate (blue squares) for different distances between pump and probe shifted away from each other along x- (open symbols) and y-axis (filled symbols). Values are from best fits of a decaying sine function to the experimental data. Calculations of the dispersion relation (see Eqs. (6.18)–(6.20)) to these fit parameters are in good agreement with experimental results and are shown by solid (along x-axis) and dashed lines (along y-axis). $H_{\text{ext}} = 1.03\,\text{kOe}$.

much quicker, already at $12\,\mu$m distance it is comparable to the amplitude of the SWs in $\pm x$ direction after around $40\,\mu$m. And after a propagation length of more than $24\,\mu$m they are not detectable anymore. Obviously, for the applied field of $H_{\text{ext}} = 1.03\,\text{kOe}$, the SWs can travel only much shorter distances in $\pm y$ direction.

Furthermore, with increasing spatial shift between pump and probe, the decay rate (τ^{-1}) diminishes. For distances where the precessional signal originates entirely from the propagating SWs, the rate undercuts $0.3\,\text{ns}^{-1}$ (see blue squares in Fig. 6.3), thus, in the time window of 1 ns between two pump pulses the oscillations decay so little that no damping is observable.

6.1.2 Discussion of the Observed Phenomena

All these features are again related to the periodic pumping, i.e. the synchronizing of the oscillations, and involve the specific character of the SW dispersion. Let us start with the explanation for the extraordinary long propagation distance. Iron garnets are known for its small Gilbert damping, and in fact for Bismuth substituted iron garnets $\alpha \approx 10^{-3}$ [Hung et al., 2010], which corresponds to a lifetime of $\tau \approx 100\,\mathrm{ns}$. Consequently, the decay time of the magnetization precession is mainly determined by two mechanisms: first, the energy spread away from the excitation spot by traveling SWs, and second, dephasing of SW modes with different frequencies due to the dispersion relation and group velocity. The first point is an inevitable circumstance when generating SWs, but the latter can in fact be tailored by periodic pumping as in our case, since the train of pump pulses narrows the spectrum of the generated SWs. In general, for optical generation of SWs, a single pulse excites all SWs with wavenumbers $k < 1/r$, so that their frequencies ω lie in the range:

$$\omega(1/r) < \omega < \omega(0), \tag{6.1}$$

where $\omega(r)$ is given by the dispersion relation of the excited SW. This means, optical excitation with laser beams focused on micrometer spot sizes comes along with a broad spectrum of SWs, causing a strong dephasing, limiting their propagation distance significantly. However, the train of pulses seperated by 1 ns temporal distance singles out these frequencies from the excited SW spectrum which are multiples of the laser repetition rate $F_{\mathrm{Rep}} = 1/T_{\mathrm{Rep}} = 1\,\mathrm{GHz}$. For the results presented here it is $T_{\mathrm{Rep}}\omega/2\pi = 3$. This narrows the SW spectrum considerably, decreasing dephasing mechanisms and enables the SWs to propagate over such long distances. This is in good agreement with the fact that the oscillatory signal caused by propagating SWs exhibit only integer multiples of the excitation rate when scanning H_{ext}, see Fig. 6.4. As a comparison, the magnetization precession frequencies for different magnetic fields are also shown, which exhibit approximately a linear dependency on H_{ext} for these magnetic field range.

What does the periodic pumping has to do with the pronounced directionality? Obviously, for $H_{\mathrm{ext}} = 1.03\,\mathrm{kOe}$ the SWs propagate along the x-axis (parallel to the applied magnetic field) much more efficiently than perpendicular to it along the y-axis. The maximum distance up to which the SWs are detectable is almost $100\,\mu\mathrm{m}$ in contrast to just $24\,\mu\mathrm{m}$ for $\pm x$ and $\pm y$ direction, respectively. This originates from different dispersion relations for the two directions, which are calculated from the transcedental equations deduced by Gieniusz and Smoczynski [1986].

In all cases, we are concentrating solely on an in-plane magnetized film ($H_{ext} = H_{\|}$). Let us start with SWs propagating along the applied magnetic field ($k_y = 0$):

$$\tan\left(k_x d\sqrt{\frac{-1}{\mu_{zz}}}\right) = \frac{-2\mu_{zz}\sqrt{-1/\mu_{zz}}}{1+\mu_{zz}}, \tag{6.2}$$

with d for the magnetic film thickness and μ_{zz} for the zz-component of the 3×3 permeability tensor μ:

$$\mu_{zz} = 1 + \frac{4\pi A}{AB - \Omega^2 - D^2}, \tag{6.3}$$

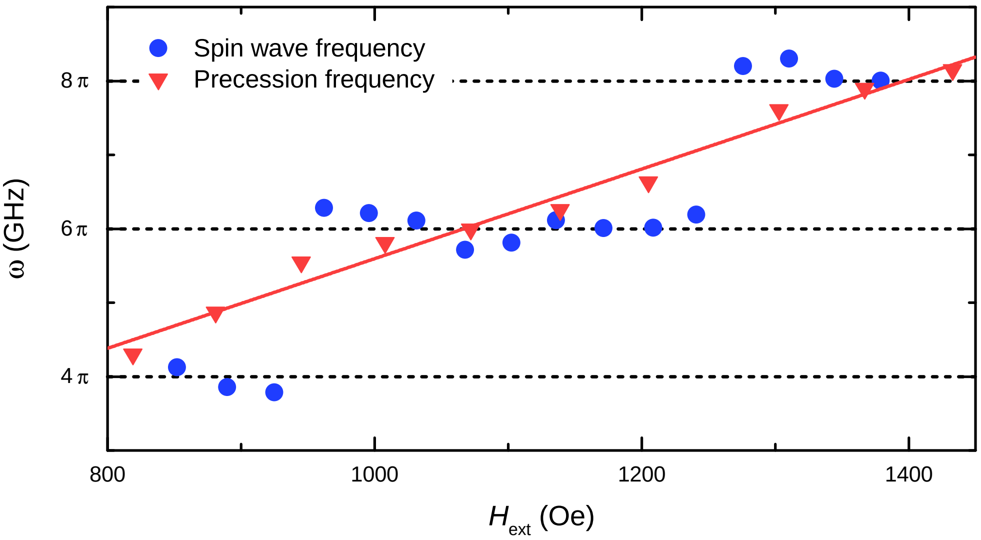

Figure 6.4: SW (blue circles) and magnetization precession frequencies (red triangles) for different external magnetic fields. The precession frequency increases roughly linearly for increasing magnetic field, while the SW frequencies are only integer multiples of the excitation rate ($F_{\text{Rep}} = 1\,\text{GHz}$), shown as dashed lines. The red solid line is a linear fit to the experimental data of the precession frequency.

with the abbreviations:

$$A = H_{ext}/M_s, \tag{6.4}$$

$$B = (H_{ext} - H_u - H_k)/M_s, \tag{6.5}$$

$$D = \sqrt{2}H_k/M_s, \tag{6.6}$$

$$\Omega = \omega/\gamma M_s, \tag{6.7}$$

where M_s is the saturation magnetization, $H_u = 2K_u/M_s$ the uniaxial anisotropy contribution, $H_k = K_1/M_s$ the cubic anisotropy contribution and $\gamma = 1.76 \times 10^{-11}\,\text{rad}\,\text{Oe}^{-1}\,\text{s}^{-1}$ the gyromagnetic ratio.

The backward volume waves are restricted to a finite frequency range, whose lower limit is:

$$\omega_0 = \gamma M_0\sqrt{AB - D^2}, \tag{6.8}$$

and the upper limit is:

$$\omega_2 = \gamma M_0\sqrt{AB - D^2 + 4\pi A}. \tag{6.9}$$

For $k_y \neq 0$ the dispersion relation reads:

$$\tan(k_y db) = \frac{-2\phi\mu_{zz}b}{\phi^2 - \left(\mu_{zy}^i\right)^2 - \left(\mu_{zy}^r\right)^2 + \mu_{zz}\left(\mu_{yy} + \chi^2\right)}, \tag{6.10}$$

where

$$b = \sqrt{\left(\mu^r_{zy}/\mu_{zz}\right)^2 - (1/\mu_{zz})\left(\mu_{yy} + \chi^2\right)}, \tag{6.11}$$

$$\phi = \sqrt{1 + \chi^2}, \tag{6.12}$$

$$\chi = k_x/k_y, \tag{6.13}$$

and the permability components:

$$\mu_{yy} = 1 + \frac{4\pi B}{AB - \Omega^2 - D^2}, \tag{6.14}$$

$$\mu^i_{zy} = \frac{4\pi\omega}{AB - \Omega^2 - D^2}, \tag{6.15}$$

$$\mu^r_{zy} = \frac{4\pi D}{AB - \Omega^2 - D^2}. \tag{6.16}$$

The lower and upper limits ω_1 and ω_3, respectively, of the restricted frequency range for these waves are given by:

$$\omega_{1/3} = \gamma M_s \left[AB - D^2 + 2\pi A + \left(\frac{2\pi}{\chi^2 + 1}\right) \cdot \left(B \pm \sqrt{(A(1+\chi^2) - B)^2 + 4(\chi^2 + 1)D^2}\right)\right]^{1/2}. \tag{6.17}$$

The calculated SW dispersion relation for sample-A is shown in Fig. 6.5 for $0 < kr_0 < 2$, where r_0 is the spot radius of the focused pump laser beam. The two displayed branches are for the two different geometries: SWs traveling along the external magnetic field ($k_y = 0$, blue line), calculated with Eq. (6.2) and perpendicular to it ($k_x = 0$, red line), calculated with Eq. (6.10). Optical pulses excite all SWs with $kr_0 < 1$, indicated by the cyan rectangular region in the figure. Both branches of the SW dispersion have frequencies ω and corresponding wavevector k which are inside of the 'excited' region, but e.g. for $H_{\text{ext}} = 1.03\,\text{kOe}$, only the k_x branch has values which are an integer multiple of the excitation rate F_{Rep} (here, for $kr = 0.4$: $\omega/2\pi = 3$, indicated by the green dashed line), while for the k_y there is no such value of ω. Consequently, the periodic pumping introduces an additional pronounced directionality. While the external magnetic field changes the dispersion relation, the excitation rate influences the values of ω which are singled out. By varying one of these parameters, one could possibly alter the pronounced propagation direction of the generated SWs.

To evaluate the SW amplitude and decay rate (see Fig. 6.3), we numerically calculate the measured oscillations for different distances from the pump spot in $\pm x$ and $\pm y$ direction. The probe beam travels approximately normal through the magnetic film and thus, the measured signal is determined by the m_z component of the induced magnetization. This is given by a two-dimensional integration over [Zhang et al., 2015]

$$m_z(\mathbf{r}, t) \propto \int d\mathbf{k}\hat{h}(\mathbf{k}) \sin(\mathbf{kr} - \omega(\mathbf{k})t) \exp(-\alpha_{\text{eff}}\omega(\mathbf{k})t), \tag{6.18}$$

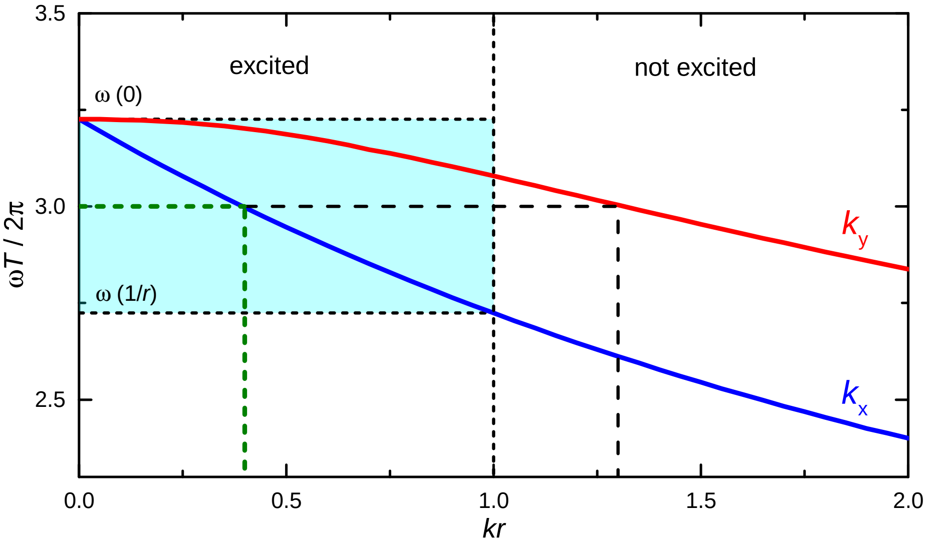

Figure 6.5: Dispersion relation for k_x and k_y of backward magnetostatic spin waves at $H_{\mathrm{ext}} = 1.03\,\mathrm{kOe}$. The cyan region is indicating all k values of the SWs which are excited by a optical pulse with spot radius r ($kr < 1$) and the corresponding angular frequency ω. For this magnetic field, only the SWs along the $x-$axis have a frequency component which is an integer multiple of the excitation rate.

with $\hat{h}(\mathbf{k})$ as the Fourier transform into k-space of the effective magnetic field $h(\mathbf{r})$ induced by a single laser pulse, $\omega(\mathbf{k})$ for the SW frequency calculated in the previous paragraphs and α_{eff} for an effective SW damping constant. The exciting pump laser spot has a Gaussian beam profile, i.e. $h(\mathbf{r}) \propto \exp(-r^2/r_0^2)$. In k-space this can be written as:

$$\hat{h}(\mathbf{k}) \propto \exp\left(-\mathbf{k}^2 r_0^2\right). \tag{6.19}$$

Eq. (6.18) is the induced magnetization m_z by a single pulse. For a train of laser pulses the sum of each m_z needs to be calculated. After N incident laser pulses, the total induced magnetization M_z is given by:

$$M_z(\mathbf{r}, t) = \sum_{n=0}^{N-1} m_z(\mathbf{r}, t - nT) \qquad n \text{ is integer}. \tag{6.20}$$

We set $N = 100$ for the calculations to achieve quasi-stationary magnetization dynamics. The resulting amplitudes and decay rates for the propagating SWs at different distances from the pump spot are shown in Fig. 6.3. The calculated SW distribution also reveals a pronounced directionality [Jäckl et al., 2017].

What is about the vanishing decay rate for sufficiently large distances from the excitation spot? The oscillatory signal recorded when pump and probe overlap (no spatial shift) is a superposition of the forced oscillations from the periodic pumping whose amplitude is

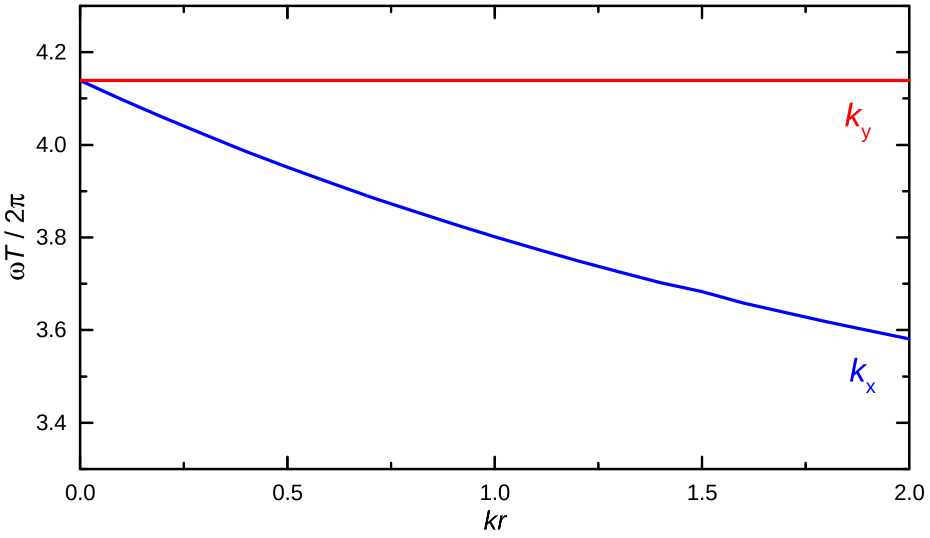

Figure 6.6: Dispersion relation for k_x and k_y at $H_{\text{ext}} = 1.03\,\text{kOe}$ without considering anisotropy effects ($K_u = K_1 = 0$). The branch for $k_x = 0$ is independent on k. In this case the group velocity for $k_x = 0$ is zero and no traveling SWs are launched.

constant in time and of the free oscillations whose decay time depends on the quality factor of the mode (see chapter 5.2), in the case of sample-A $\tau = 0.77\,\text{ns}$. When moving pump and probe away from each other, at distances from $15\,\mu\text{m}$ or more, the free-oscillation component is fully decayed and only the forced oscillation is visible, where the decay is zero. Consequently, the magnons at such distances do not decay in time.

But before we end this discussion, let us answer the question, what kind of SWs we observed for the propagation direction perpendicular to H_{ext} (along the y-axis). According to Sec. 2.3.2 we should observe for this geometry only magnetostatic surface waves with phase and group velocity in the same direction, thus considered to be *forward* waves. However, the dispersion relation shows an opposite dependency of ω on k. And indeed, we are detecting in this case also BVMSWs just as for the geometry of a propagation parallel to H_{ext}. For an efficient generation of MSSW the pump beam diameter has to be sufficiently small [Chernov et al., 2017]. That we still see backward volume waves has two reasons. Number one is a non-zero pump beam diameter, so even for a shift along the y-axis we detect SWs with $k_x \neq 0$ which is one condition for these waves. Second, magnetic anisotropy plays a big role in our experiment. If we set both anisotropy constants K_u and K_1 (uniaxial and cubic, respectively) to zero for the calculation of the SW dispersion, we get $\omega(k_x = 0, k_y)$ to be independent on k, see Fig. 6.6. Consequently, the group velocity is zero, $v_g = d\omega/dk = 0$, and no propagating SWs along this direction are generated. Due to anisotropy effects, however, this dispersion relation gets modified and even for $k_x = 0$ traveling BVMSWs are launched, see Fig. 6.5.

6.2 Magnon Wavelength Tuning (Sample-C)

6.2.1 Experimental Results

All the results of the previous section were achieved from measurements on sample-A. The lifetime of the excited mode in that sample is comparable to the period T_{Rep} between two subsequent excitation pulses. For sample-C, the quality factor Q of the excited mode is exceptionally higher, leading to a lifetime of about $\tau_c = 15\,\mathrm{ns}$, so that $\tau_c \gg T_{\mathrm{Rep}}$.

Let us take a look at the propagation of the spin waves excited around the second harmonic resonance ($\omega/2\pi = 2F_{\mathrm{Rep}}$). As shown in section 5.2.3, it is achieved for external magnetic fields around $H_{\mathrm{ext}} = 570\,\mathrm{Oe}$ (see Fig. 5.17). The SW propagation is shown in Fig. 6.7 for three slightly different magnetic fields around the resonance position.

The red-blue color code gives the polar angle of the magnetization for different time delays between pump and probe and spatial shifts along the x-axis, i.e. parallel to H_{ext}, as for all SW propagation measurements in this section. For the measurements on sample-C the laser beams were focused onto slightly smaller spot sizes on the sample surface, resulting in spot radii of about 4 and $5\,\mu\mathrm{m}$ for the probe and pump beam, respectively. As soon as the displacement of pump and probe is above this value, the overlap of both laser spots becomes negligible, all further signal comes again only from the propagating SWs. We see again the amplitude dropping for increasing distances from the origin, but also a linear change of the phase, which is due to the propagating SWs at a given phase velocity.

All acquired time traces can be fitted with a decaying sine function (see Eq. (5.1)), where amplitude and phase depend on the spatial distance to the excited spot: $\theta_0 = \theta_0(x)$ and $\zeta = \zeta(x)$. Remarkably, not only the amplitude depends very strongly on the external magnetic field (as already shown in Fig. 5.16) but also the phase ζ and its velocity v_p. However, the SW frequency $\omega/2\pi = 2\,\mathrm{GHz}$ remains almost constant, which is an integer multiple of the 1 GHz-excitation rate.

Let us take a closer look at the dependence of the phase ζ on the propagation distance x. The values from the best fits of the decaying sine function are extracted and presented in Fig. 6.8 for five different magnetic fields around the second resonance position and for an increasing distance to the excitation spot. From distances of $5\,\mu$ and more, the measured signal originates from traveling SWs and the change in $\zeta(x)$ becomes linear. The phase can then be represented as $\zeta(x) = k_m x + \mathrm{const.}$, where k_m is the mean wavenumber of the generated SWs. Fitting the experimental data of $\zeta(x)$ for $x > 5\,\mu\mathrm{m}$ with linear functions, reveals a growth of $k_m = (0.04 \pm 0.01)\,\mathrm{rad}\,\mu\mathrm{m}^{-1}$ for the smallest of the five magnetic fields $H_{\mathrm{ext}} = 560\,\mathrm{Oe}$ up to $k_m = (0.48 \pm 0.03)\,\mathrm{rad}\,\mu\mathrm{m}^{-1}$ at $H_{\mathrm{ext}} = 577\,\mathrm{Oe}$. This corresponds to a tremendous rise of k_m by more than one order of magnitude when varying the external magnetic field just slightly by 17 Oe or 3 % of the total value. The mean wavelength λ_m is connected to the mean wavenumber by $\lambda_m = 2\pi/k_m$, which means the wavelength varies

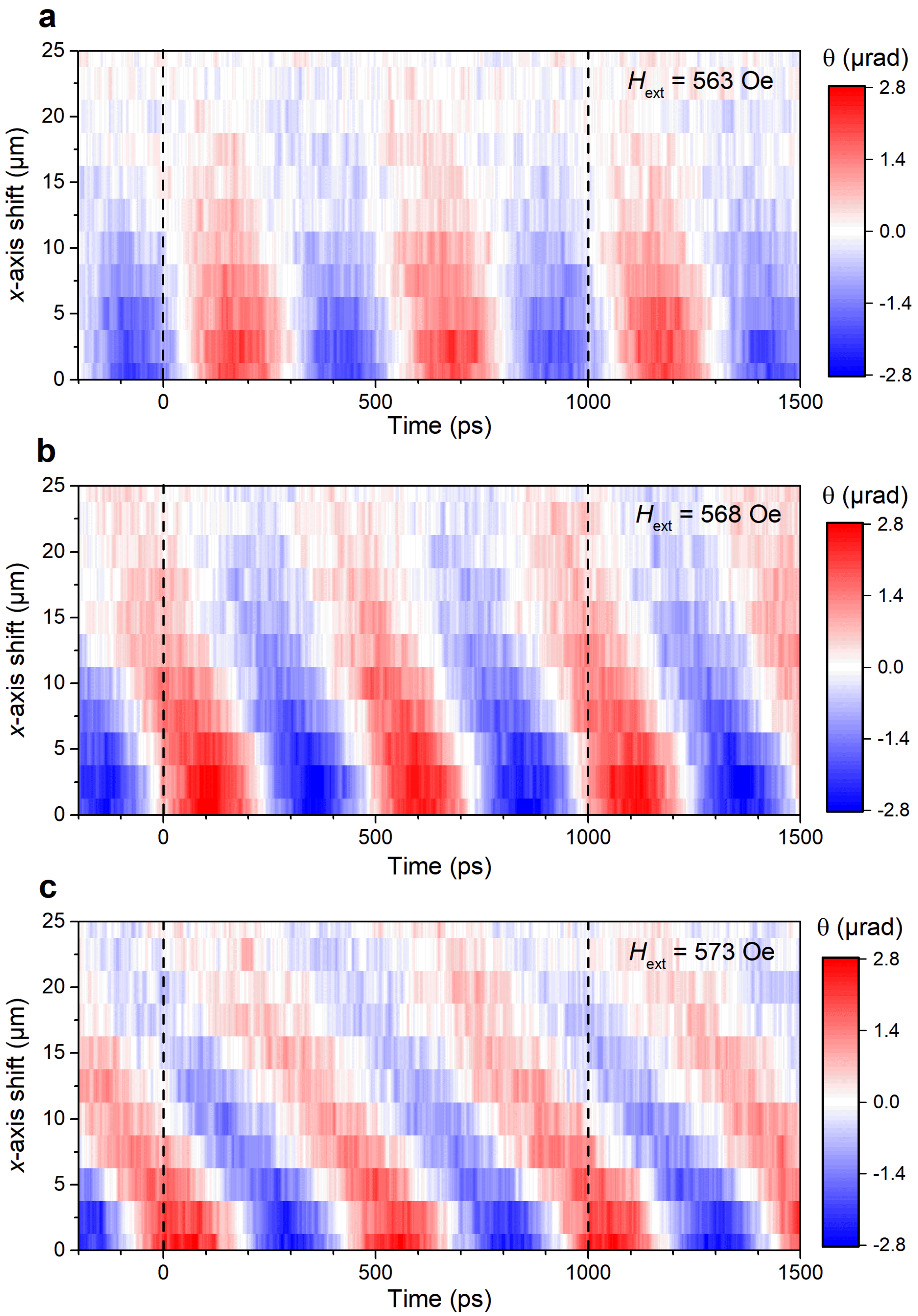

Figure 6.7: Color plot of propagating SWs in sample-C for three different external magnetic fields: $H_{\mathrm{ext}} = 563\,\mathrm{Oe}$ (**a**), 568 Oe (**b**) and 573 Oe (**c**). The color code (red and blue) gives the out-of-plane angle of magnetization θ. The black dashed lines indicate the impact of the pump pulses. The phase velocity of the propagating SWs depends strongly on H_{ext}, compare the different changes in phase when increasing the spatial shift.

from $\lambda_m = (13 \pm 1)\,\mu$m up to $(160 \pm 40)\,\mu$m. An overview of the mean wavenumber k_m to the corresponding external magnetic field is shown in Tab. 6.1.

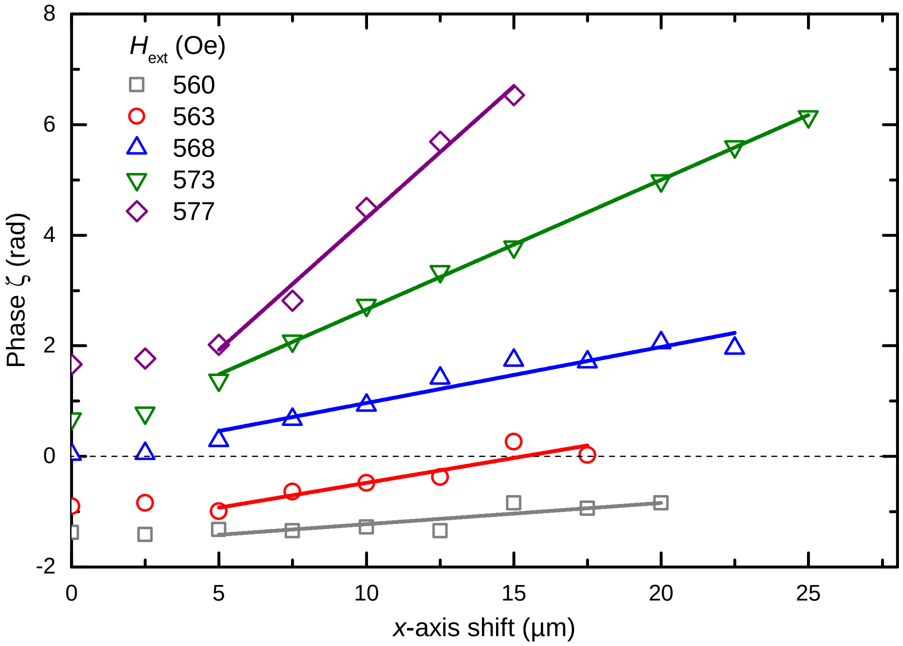

Figure 6.8: Phase $\zeta(x)$ of the propagating SWs for different magnetic fields around the second resonance position (open symbols) and linear fits to the experimental data (solid lines) in sample-C. Just a small variation of the external magnetic field H_{ext} by a few Oersted changes the phase velocity tremendously. The slope of $\zeta(x)$ gives the mean wavenumber k_m of the SWs.

The change of the SW wavelength when varying H_{ext} is also directly visible when looking at the magnetization angle $\theta = \theta(x, t = \mathrm{const.})$ parallel to the probe beam at a fixed time point t, see Fig. 6.9. The angle is shown for an increasing distance for the five different external magnet fields. The point of the fixed moment is chosen when the magnetization precession amplitude θ is maximal at the position where it is illuminated by the pump pulse $(x = 0)$.

Let us compare the results for $\zeta(x)$ in the configuration of a strong cumulative excitation, $T_{\mathrm{Rep}} \ll \tau$, with a configuration of relatively rare impinging of pump pulses, such that $T_{\mathrm{Rep}} \gg \tau$. For that, sample-A with $\tau_A = 0.70\,$ns was excited at different external magnetic fields by a laser system with 80 MHz repetition rate, i.e. $T_{\mathrm{Rep}} = 12.5\,$ns, by colleagues at the Lomonosov State University Moscow in Russia, see Fig. 6.10 [Savochkin et al., 2017]. Obviously, varying H_{ext} has no significant impact on the phase $\zeta(x)$. Within the range of error, the phase velocity is the same for all different magnetic fields. Also the amplitude of the Faraday rotation angle ϕ_{FR} does not change with H_{ext}, see inset in Fig. 6.10, which is

H_{ext} [Oe]	k_m [rad μm^{-1}]	Δk_m [rad μm^{-1}]	λ_m [μm]	$\Delta\lambda_m$ [μm]
560	0.04	0.01	160	40
563	0.09	0.02	70	14
568	0.10	0.01	62	7
573	0.234	0.003	26.8	0.4
577	0.48	0.03	13.2	0.9

Table 6.1: Evaluated mean wavenumbers k_m and corresponding wavelengths λ_m with standard deviation Δk_m and $\Delta\lambda_m$, respectively, of the generated SWs at different external magnetic fields H_{ext}. The values are from best fits of the linear dependency of the phase $\zeta(x)$ to the propagation length in x direction.

in accordance to the theory. In the expression for the amplitude of Eqs. (5.18), the part depending on ω, and therefore on H_{ext}, vanishes for sufficiently large pulse separation:

$$\exp(-T_{\mathrm{Rep}}/\tau) \longrightarrow 0. \tag{6.21}$$

6.2.2 Discussion of the Observed Phenomena

Dependence of the SW Amplitude on the Wavevector k

Let us start with the dependency of the SW dynamics on the wavevector $\mathbf{k}$. The SW amplitude, we will denote it with $\Theta(\mathbf{k})$, is determined by the Fourier transform of the magnetic field $h(\mathbf{r})$ in k-space: $\hat{h}(\mathbf{k})$. $h(\mathbf{r})$ is the strength of the magnetic field induced by one circularly polarized pump pulse via the inverse Faraday effect. Since the strength depends on the intensity $I(\mathbf{r})$ of the pump beam, $h(\mathbf{r}) \propto I(\mathbf{r})$, the Fourier transformed $\hat{h}(\mathbf{k})$ is also determined by $I(\mathbf{r})$.

For a uniformly illuminated magnetic film, $\hat{h}(\mathbf{k}) = \hat{h}\delta(\mathbf{k})$, only magnetic oscillations with $k = 0$ are excited and no propagating SWs are launched. If illuminated with a laser beam focused to a spot radius of r_0, SWs with nonzero wavenumbers can be generated. For a Gaussian beam profile $\hat{h}(\mathbf{k}) = h_0 r_0 \sqrt{\pi}\exp(-\mathbf{k}^2 r_0^2/4)$, the focused laser spot can be seen as a kind of SW antenna with a wavenumber bandwidth of $0 < k < k_{\mathrm{max}}$, constrained by $\hat{h}(\mathbf{k})$: $\Theta_0(\mathbf{k}) \propto \exp(-\mathbf{k}^2 r_0^2/4)$. From this follows $k_{\mathrm{max}} = 2/r_0$, which means for our experiments with spot radius of the pump of $r_0 \approx 4\,\mu$m: $k_{\mathrm{max}} = 0.5\,\mathrm{rad}\mu\mathrm{m}^{-1}$.

This is valid for the excitation of SWs by a single pulse. If they are generated by a sequence of pulses, $\Theta_0(\mathbf{k})$ is modified by the cumulative effect. Here, $\Theta_0(\mathbf{k})$ is also determined by $\theta_0(\omega)$, which is the amplitude of the magnetic precession under the area illuminated by the pump beam, and the SW dispersion $\omega(\mathbf{k})$:

$$\Theta_0(\mathbf{k}) \propto \hat{\theta}_0(\mathbf{k})\exp(-\mathbf{k}^2 r_0^2/4), \tag{6.22}$$

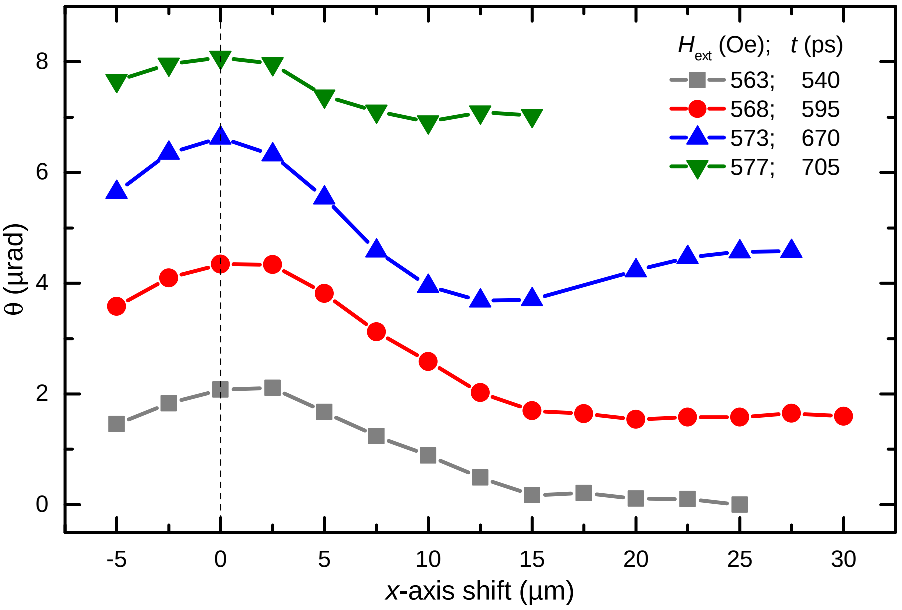

Figure 6.9: Distribution of the SW magnetization component along the probe beam propagation direction measured at a fixed time point when the precession angle is maximal at $x = 0$ for different external magnetic fields. It is clearly visible, that the wavelength at $H_{\text{ext}} = 577\,\text{Oe}$ is the smallest and increasing when reducing the field strength.

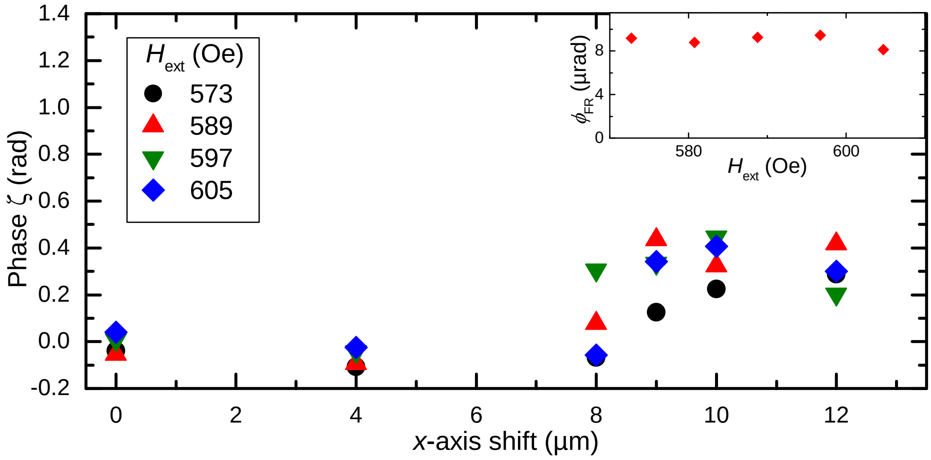

Figure 6.10: Phase of propagating SWs and precession amplitude of sample-A, excited by a single-pulse configuration ($T_{\text{Rep}} \gg \tau_A$). Changing the magnetic field has no influence on neither of both parameters. Measurements were performed by colleagues at Lomonosov State University Moscow, Russia [Savochkin et al., 2017].

with $\hat{\theta}_0(\mathbf{k}) = \theta_0(\omega(\mathbf{k}))$. Consequently, the efficiency of the generation of SWs with a particular wavenumber $\mathbf{k}$ also depends on the ratio T_{Rep}/τ.

Dependence of the Spin Dynamics on the Ratio T_{Rep}/τ

The experimental results show a big difference in the magnon wavelength tuning between highly periodic ($T_{\text{Rep}} \ll \tau$) and relatively rare pumping ($T_{\text{Rep}} \gg \tau$). To analyze this phenomen, let us start with the case where a mode of several nanoseconds lifetime, which is the case in sample-C, is excited with 1 GHz repetition rate and compare it then with the relatively short living mode in sample-A excited with a much smaller repetition rate of 80 MHz.

Optical excitation of SWs with focused light limits in our experimental setup their wavenumbers to the upper value of $k_{\text{max}} = 0.5\,\text{rad}\mu\text{m}^{-1}$. The range of wavenumbers determines the frequency range of the excited SWs through the dispersion relation $\omega(\mathbf{k})$ (calculated by Eq. (6.2)) to $\Delta\omega/2\pi = 53\,\text{MHz}$, see Fig. 6.11a. On the other hand, due to the periodic pumping the amplitude $\theta_0(\omega)$ exhibits sharp peaks with $\delta\omega/2\pi = 21\,\text{MHz}$, see Fig. 6.11b, which are separated by 1 GHz intervals equal to the excitation rate. Since the frequency range of excited SWs is much smaller than the peak separation, only one peak of $\theta_0(\omega)$ can appear within this frequency band. The SW dispersion is determined by the external magnetic field and thus, can be tuned by changing it. To generate propagating SWs, the frequency band has to be tuned by adjusting H_{ext} such that it contains one of the amplitude peaks. In the case for the second harmonic resonance ($N = 2$ in the resonance condition of Eq. (5.4)) this is given for external magnetic field strengths between $H_{\text{ext}} = 559\,\text{Oe}$ and 578 Oe.

The SW amplitude $\Theta_0(k)$ exhibits also a peak for certain values of the wavenumber k, whose position and width can be tuned by H_{ext}, see Fig. 6.11c. This is determined by the peak structure of the magnetization precession amplitude $\theta_0(\omega)$ [Fig. 6.11b] and a unique feature related to the periodic pumping. When at $\omega = \omega_1$ the precession amplitude $\theta_0(\omega_1)$ is at its maximum (here: $\omega_1 = 2\,\text{GHz}$), then the dispersion relation gives the corresponding wavenumber k_1 at which the SW amplitude $\Theta_0(k_1)$ is at its maximum. Changing H_{ext} tunes the SW dispersion [Fig. 6.11a] and therefore the wavenumber k_1 where Θ_0 is maximum. The sharper the resonance peaks of $\theta_0(\omega)$ are, the more pronounced should be the tunability of k_1.

Consequently, for $H_{\text{ext}} = 559\,\text{Oe}$ and 563 Oe, the maximum for $\Theta_0(k_x)$ is at $k_x = 0\,\text{rad}\mu\text{m}^{-1}$. However, when increasing the external magnetic field, the maximum of $\Theta_0(k_x)$ is shifted to higher wavenumber values, from $k_x = 0.11\,\text{rad}\mu\text{m}^{-1}$ at $H_{\text{ext}} = 568\,\text{Oe}$ and further to $k_x = 0.22\,\text{rad}\mu\text{m}^{-1}$ and $k_x = 0.35\,\text{rad}\mu\text{m}^{-1}$ for $H_{\text{ext}} = 573\,\text{Oe}$ and 579 Oe, respectively. When comparing these values with the experimentally measured results for the $\zeta(x)$ plots, we find wavenumbers which are very similar to the ones corresponding to the maxima of $\Theta_0(k_x)$, see Fig. 6.8 and Tab. 6.1. Accordingly, this is the explanation of the

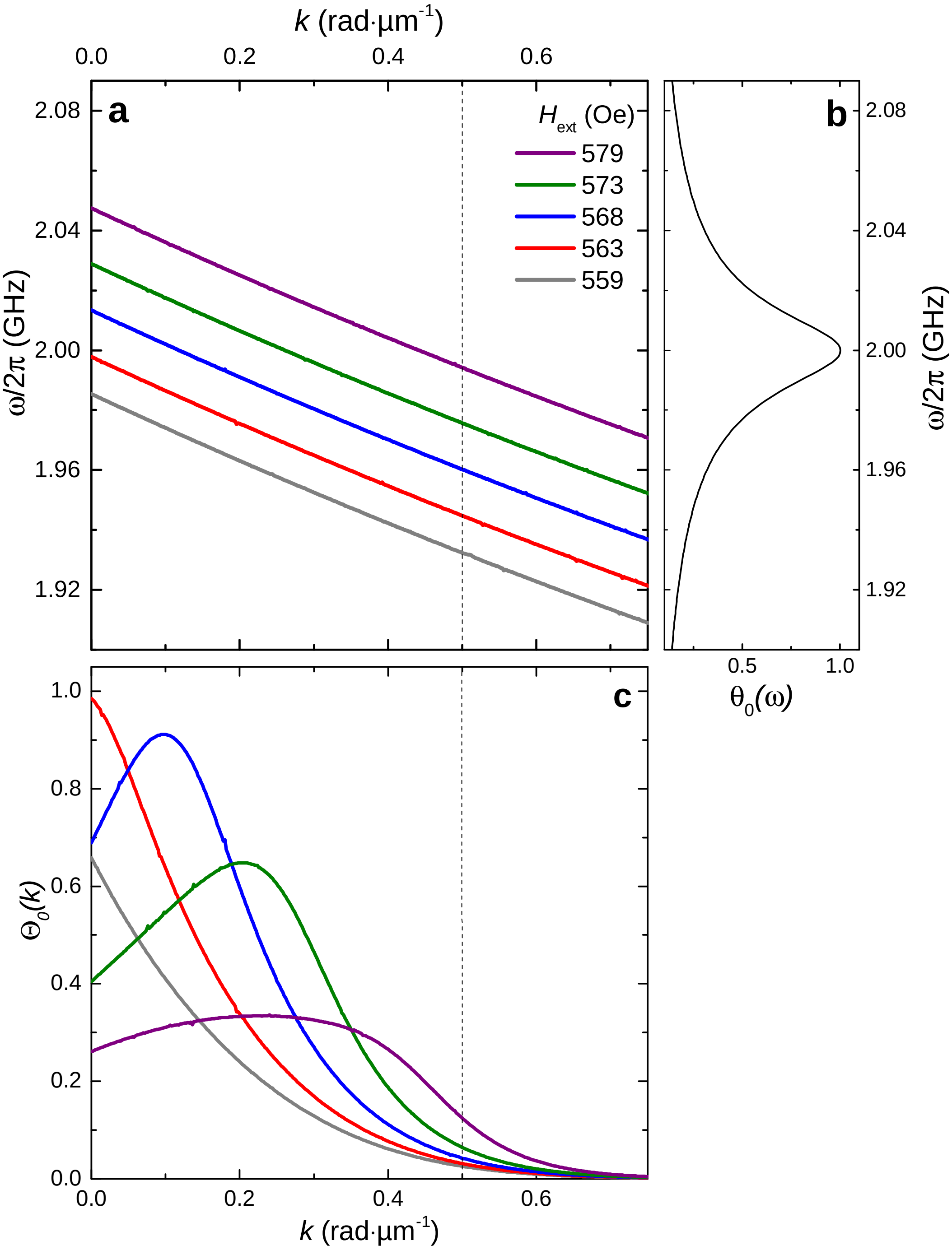

Figure 6.11: SW dynamics in sample-C under highly periodic pumping. (**a**) SW dispersion relation for five different external magnetic fields. (**b**) Dependency of the precession amplitude θ_0 on the frequency ω and (**c**) of the SW amplitude on the wavenumber k. The dashed, thin line in **a** and **c** gives $k_{\max}$ of the generated SWs. For a detailed explanation of the plots see the text.

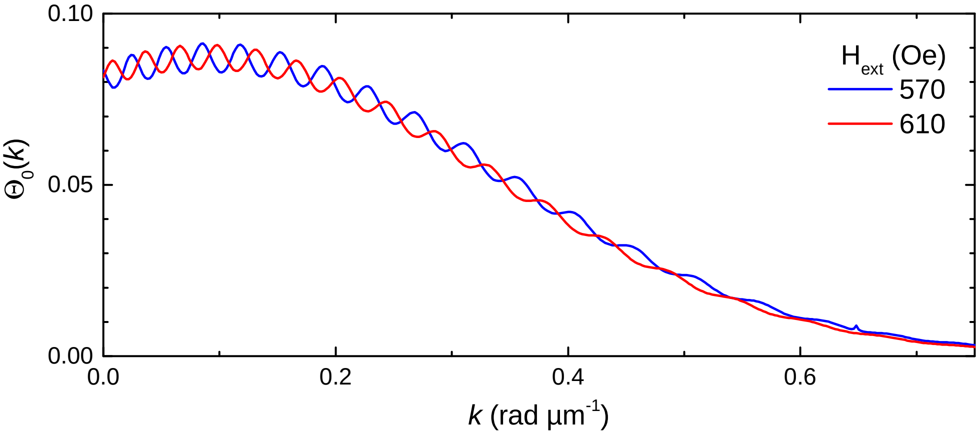

Figure 6.12: Calculation of $\Theta_0(k)$ for sample-A under relatively rare excitation with $F_{\text{Rep}} = 80\,\text{MHz}$. The oscillations are negligible small and therefore, one can speak of a single-pulse excitation, where the SW generation does not depend on small changes of H_{ext}.

tunability of the SW wavenumber and in consequenze of the wavelength by changing the magnetic field.

If, on the other hand, the excitation intervall is much larger than the lifetime, $\Theta_0(k)$ does not change the position and width of the peak with the external magnetic field H_{ext}, see Fig. 6.12. Only small oscillations occur, experimentally negligible, determined by the excitation repetition rate of 80 MHz. Therefore, one can speak of a single-pulse experiment in this case.

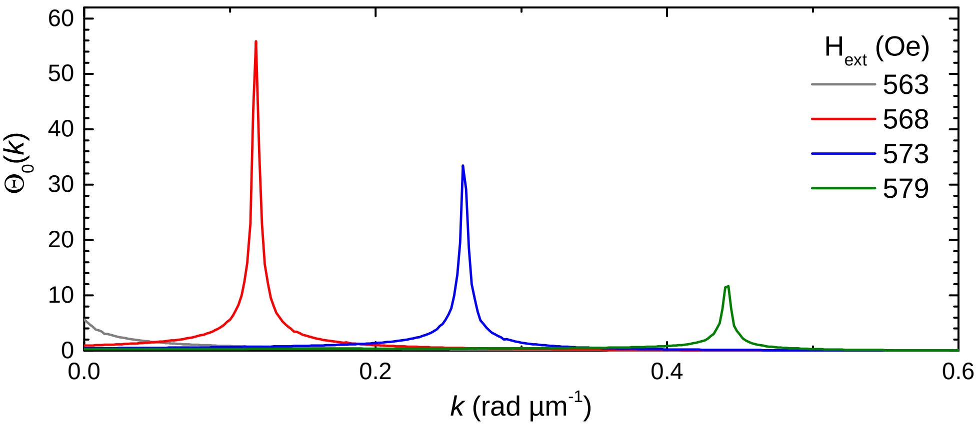

Figure 6.13: Calculation of $\Theta_0(k)$ for an iron garnet film with ultra low damping and therefore a lifetime of $\tau = 800\,\text{ns}$ of the magnetization precession, excited by a train of pulses with 1 ns separation. SWs are excited within a very narrow band of wavenumbers $\delta k \approx 6 \times 10^{-3}\,\text{rad}\,\mu\text{m}^{-1}$.

Putting these together, the ratio between the pulse intervall T_{Rep} and the lifetime τ of the excited mode is crucial for phenomena connected to the cumulative excitation. Consequently, for iron garnet films with ultra low magnetic losses and small group velocity of propagating SWs, the effective damping constant can be as small as $\alpha_{\mathrm{SW}} = 1 \times 10^{-4}$ [Hauser et al., 2016]. α_{SW} is an effective damping constant where all dissipation is included. In the case of iron garnets, where the Gilbert damping is negligible, it is mainly determined by energy spread away from propagating SWs, but also desynchronization and destructive interference of different harmonic modes. This effective damping constant corresponds to a lifetime of about $\tau = 800\,\mathrm{ns}$, which leads to even sharper resonances of $\Theta_0(k)$, allowing to generate SWs in a narrow wavenumbers band of $\delta k \approx 6 \times 10^{-3}\,\mathrm{rad}\,\mu\mathrm{m}^{-1}$ and an enhancement of the SW amplitude by a factor of about 800, see Fig. 6.13.

7 Optical Spin Orientation in a CdTe Quantum Well

7.1 Introduction

In this chapter we will present the results from optical (spin) orientation measurements on a CdTe semiconductor performed with the 1 GHz laser system (see chapter 3.2.3) which can give an insight into spin coherence. If the dephasing time is longer than the excitation period, each pump pulse injects again a spin polarization and triggers its macroscopic precession before the previously excited spin ensemble has dephased completely and could come back to its equilibrium position. The spin precession can then be amplified resonantly by the train of laser pulses, similar to the resonant excitation of magnetization precession in iron garnet films in chapter 5.2. This well established technique is called resonant spin amplification (RSA) [Kikkawa and Awschalom, 1998]. Topic of interest is the coherent spin dynamics of carriers which are confined in semiconductor nanostructures such as quantum wells (QWs).

Usually, when RSA measurements are performed with an ordinary pump probe setup[a], the time delay between pump and probe pulse is set to a fixed point, normally to a small delay shortly before the arrival of the pump pulse, e.g. at $t = -100\,\text{ps}$. The formerly randomly aligned spins get partially oriented after illumination by the circularly polarized pump pulse. This induces a spin polarization which is called optical orientation. The now induced macroscopic magnetic moment then starts to precess around an external magnetic field. The Larmor precession frequency Ω_L of the spin ensemble is determined by the externally applied magnetic field B_{ext}, thus by varying the field strength, the precession frequency is tuned, see corresponding chapters in Section 2.4 and Eq. 2.44. Note that we will use in this entire chapter the magnetic flux density B to describe the magnetic field induced by the electromagnet instead of H. In vacuum ($M = 0$) both quantities are the same and only differ in their units. Here, no magnetization M is induced inside of the sample, so the choice between both quantities is quite random. We will use B_{ext} to be consonant with most textbooks describing the Larmor precession.

Equally to the resonant excitation of magnetization precession, the Larmor precession amplitude is maximized when its frequency is an integer multiple of the excitation frequency (cf. Eq. (5.4)), which is now a resonant spin amplification. Sweeping the external magnetic

---

[a] Where both lasers emit pulses with the same repetition rate and the time delay between the pump and probe pulses is varied by a retroreflector on a delay line.

field and measuring the magnetization component along the propagation axis M_z (by a second probe pulse) at a fixed time point reveals sharp resonance peaks, whose width gives insight of the spin dephasing time T_2^* of the excited spin ensemble. This method of RSA is useful to measure spin dynamics of carriers, in particular the spin dephasing time. For further information, see the work of [Kikkawa and Awschalom, 1998; Yakovlev and Bayer, 2008; Yugova et al., 2012]. For a more detailed comparison to the resonant excitation of magnetization precession in iron garnets from Chapter 5, see the introduction of Sec. 2.4.

7.2 Optical Spin Orientation with the ASOPS Technique

In the case of spin excitation by the ASOPS technique there is no delay line, and therefore, the time delay between pump and probe cannot be fixed at one certain point. Instead, the whole dynamics between two subsequent pump pulses in the time window of $T_{\text{Rep}} = 1\,\text{ns}$ is measured for each magnetic field. Due to much higher signal magnitude than at the measurements with the iron garnet sample, a significantly smaller number of averaging is necessary, leading to a total integration time of about 20 s for each time trace. Some example graphs are shown in Fig. 7.1, where the red, green, blue and brown symbols show the first four resonance cases where the Larmor frequency fulfills the resonance condition:

$$\Omega_L(B) = N\frac{2\pi}{T_{\text{Rep}}} \qquad N \text{ is integer.} \tag{7.1}$$

The blue and the pink symbols represent intermediate cases between the first and the second side resonance peak. The grey symbols show the signal for $H_{\text{ext}} = 0$. Obviously, the precession amplitude is at its maximum when the Larmor precession fulfills the resonance condition.

7.2.1 Analysis by Fitting a Decaying Sine Function

Basically there are two ways to analyze the acquired time traces. One is to fit a decaying sinusoidal function to each of them and extract the fitparameters, from where one can gather information about the spin dynamics. The second would be to extract the signal at one specific time point and plot it versus the external magnetic field. This would be very similar to ordinary RSA measurements.

But let us start with the first method, which is very similar to the analysis of the magnetization precession measurements in iron garnet films. For this the time-resolved ellipticity $\varepsilon(t)$ measurements are fitted with a decaying sine function:

$$\varepsilon(t) = \varepsilon_0 e^{-t/\tau}\sin(\Omega_L t + \phi), \tag{7.2}$$

with the precession amplitude ε_0, the spin dephasing time $\tau = T_2^*$ and the phase ϕ. This gives only reasonable results for sufficient large H_{ext} when $\varepsilon(t)$ exhibit an oscillatory signal,

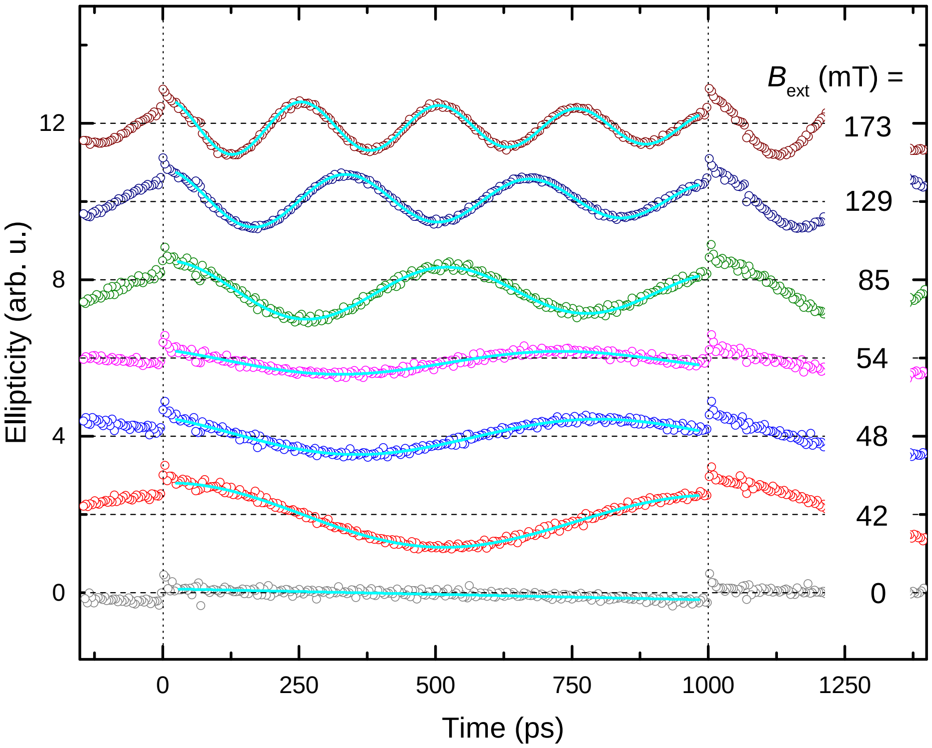

Figure 7.1: Spin precession in the CdTe sample for different magnetic fields (open circles) measured by Faraday ellipticity. The first, second, third and fourth harmonic of the spin precession is shown, as well as for zero-field (grey symbols) and intermediate steps (blue and pink symbols). A best fit of a decaying sine function (see Eq. (7.2)) to the experimental data is displayed by cyan lines, for the zero-field measurement a linear function was fitted.

i.e. it is not working around $H_{\text{ext}} = 0$. The smallest value where the signal can be fitted by a decaying sine is $B_{\text{ext}} = 30\,\text{mT}$.

The fit parameters can give an insight to the spin dynamics. Let us first take a look at the angular Larmor precession frequency[b] Ω_L versus the swept externally applied magnetic field, shown in Fig. 7.2. In accordance to Eq. (2.44) the frequency exhibits a linear dependency to B. A best fit of a linear function, using the least square method, gives for the slope:

$$m = (1.437 \pm 0.004) \times 10^{11}\,\text{Hz/T}, \tag{7.3}$$

from where follows for the electron g-factor:

$$|g_e| = 1.64. \tag{7.4}$$

---

[b] Often we will display $\Omega_L/2\pi = F_L$ because it is easier to compare with the excitation rate of $F_{\text{Rep}} = 1\,\text{GHz}$.

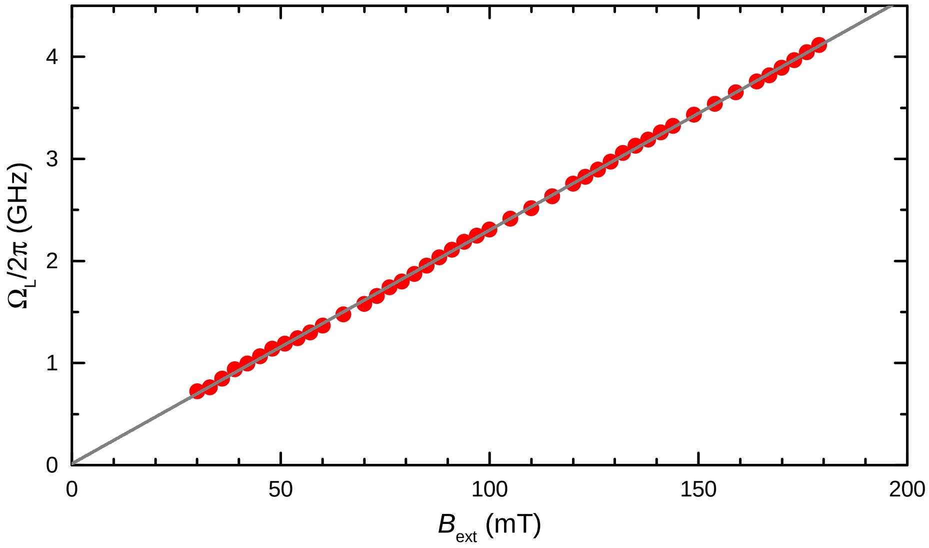

Figure 7.2: Larmor precession frequency Ω_L versus external magnetic field (red circles). The frequency shows a linear dependency. A best fit of a linear equation (grey line) to the experimental data reveals a electron g-factor of $|g_e| = 1.64$.

This is the equal to a previously evaluated value for a 20-nm-thick CdTe/(Cd,Mg)Te quantum well [Yakovlev and Bayer, 2008].

Taking a look at the fit parameter for the phase ϕ shows also a dependency on the magnetic field, see Fig. 7.3. It is oscillating between $\phi_{\text{min}} \approx \pi/3$ and $\phi_{\text{max}} \approx 2\pi/3$ and for the resonance cases (green dashed lines) the phase is close to $\phi_{\text{res}} = \pi/2$. In the resonance case the spin injection is in phase with the spin precession. The fitting function is a decaying sine, see Eq. 7.2, a phase shift of $+\pi/2$ transforms it into a cosine. Consequently, the pump pulse triggers a cosinusoidal precession of the spin ensemble.

However, the most interesting quantity is the spin dephasing time T_2^*. It can be obtained by two different ways. One is to extract the fit parameter for the lifetime $\tau = T_2^*$ from Eq. (7.2), the other is to extract the fitted amplitude for different magnetic fields and estimate the width of the resonance line by fitting a Lorentzian peak function to the data. The latter is performed for different pump densities between $13\,\text{W}\,\text{cm}^{-2}$ and $130\,\text{W}\,\text{cm}^{-2}$, see filled symbols in Fig. 7.4. The uncertainty principle

$$\Delta E \Delta t \geq \frac{\hbar}{2} \tag{7.5}$$

connects the lifetime of a state Δt with a broadening in its spectrum ΔE. With $\Delta E = \hbar\Delta\omega$ it directly follows that

$$T_2^* = (2\Gamma_\Omega)^{-1}\,, \tag{7.6}$$

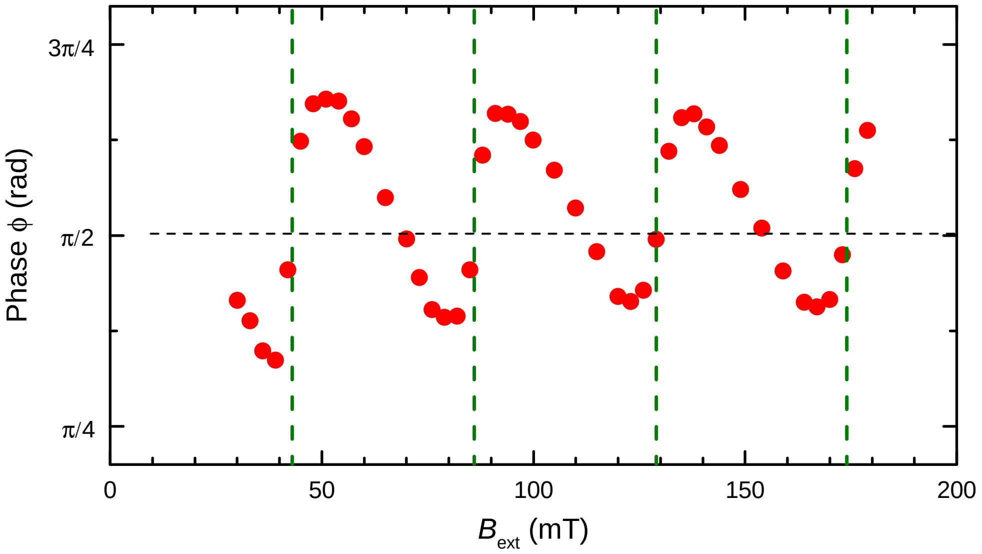

Figure 7.3: Spin precessin phase for different external magnetic fields (red circles), extracted from decaying sine fits. When the precession frequency is an integer multiple of the excitation rate (green dashed lines), the excited spin precession modes are synchronized and the phase of the decaying sine is about $\zeta = \pi/2$ (black dashed line), leading to a cosine function.

where $T_2^* = \Delta t$ is the lifetime of the Larmor precession and Γ_Ω the spectral width in the angular frequency range. It can be shown that the broadening of the spectrum has a Lorentzian shape (e.g. [Bass et al., 2009]), given by the function:

$$I(\omega) \propto \frac{2}{\pi} \frac{\Gamma_\Omega}{4(\omega - \omega_c)^2 + \Gamma_\Omega^2}. \tag{7.7}$$

Each resonance peak is fitted with the Lorentzian peak function (cyan lines in Fig. 7.4) and from the extracted fit parameter for the width the lifetime of the spin precession is calculated, see Fig. 7.5. In the same figure are also shown the extracted fit parameters from the decaying sine function of Eq. (7.2) for the different pump power densities.

A strong dependence of T_2^* on the pump power density is visible. Increasing the pump power by a factor of ten lets the spin dephasing time decrease by around 30 %. It is well known that a rise of the temperature lets the dephasing time sink when the pump wavelength is tuned onto the trion energy in the quantum well [Zhukov et al., 2007]. Increasing the power density gives also rise to the temperature of the sample under the illuminated spot.

At last, let us take a look at the amplitudes of the Larmor precession when sweeping the magnetic field over the full range[c], which is in this setup up to $B_{\text{ext}} \approx 180\,\text{mT}$. The extracted

---

[c] Experimental note: The maximal possible externally applied magnetic field strength depends strongly on the distance of the ferrites in the electromagnet. Due to the necessary flow cryostat in this experiment, the minimal distance of the ferrites is bigger than in the iron garnet measurements, decreasing the maximal possible magnetic field strength.

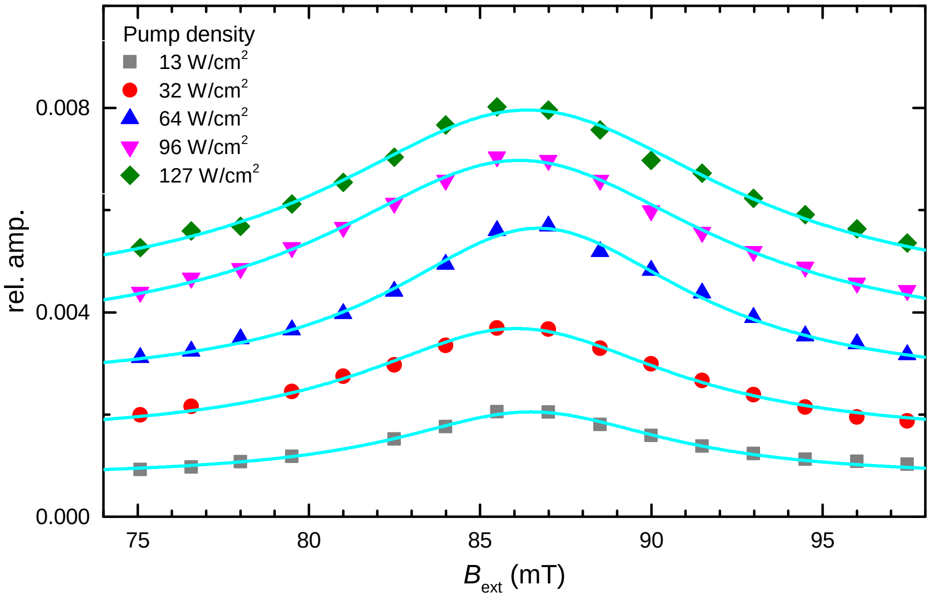

Figure 7.4: Amplitudes extracted from decaying sine function vs external magnetic field for different pump power densities. The resonance line is fitted with a Lorentzian peak function, whose width (in Hz) gives the lifetime of the spin precession. Sample temperature $T = 10\,\mathrm{K}$.

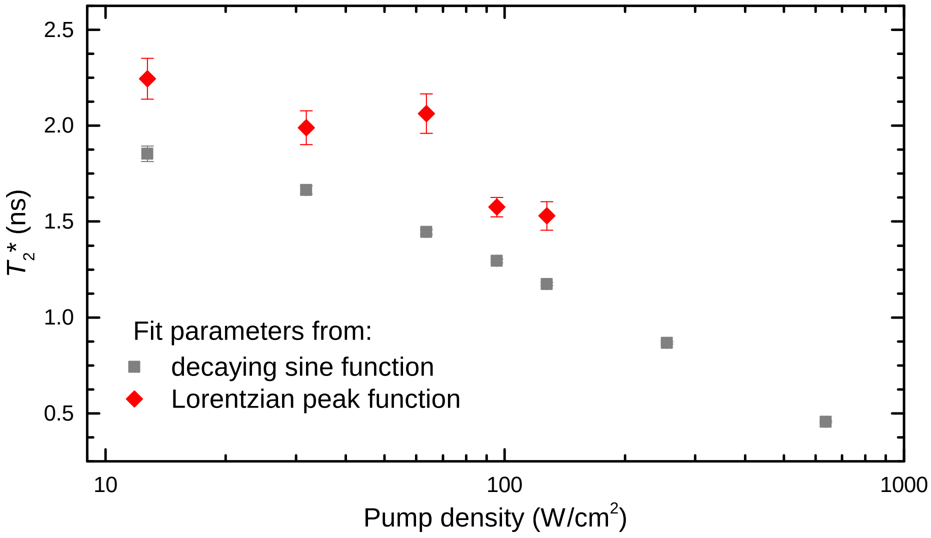

Figure 7.5: Spin dephasing time T_2^* of the Larmor precession for different pump power densities, extracted from two different fitting methods. The values are in both ways in the same order of magnitude but differ by around 20 %. The value of $T_2^* \approx 2\,\mathrm{ns}$ is around the estimated value from the literature [Yakovlev and Bayer, 2008]. Sample temperature $T = 10\,\mathrm{K}$.

fit parameter for the amplitude ε_0 is shown in Fig. 7.6 for all measured time traces against the applied magnetic field. Four resonant side peaks for $\Omega_L = 2\pi N F_{\text{Rep}}$ with $N = (1, 2, 3, 4)$ are within the magnetic field range. Each of the peaks are fitted with a Lorentzian peak function.

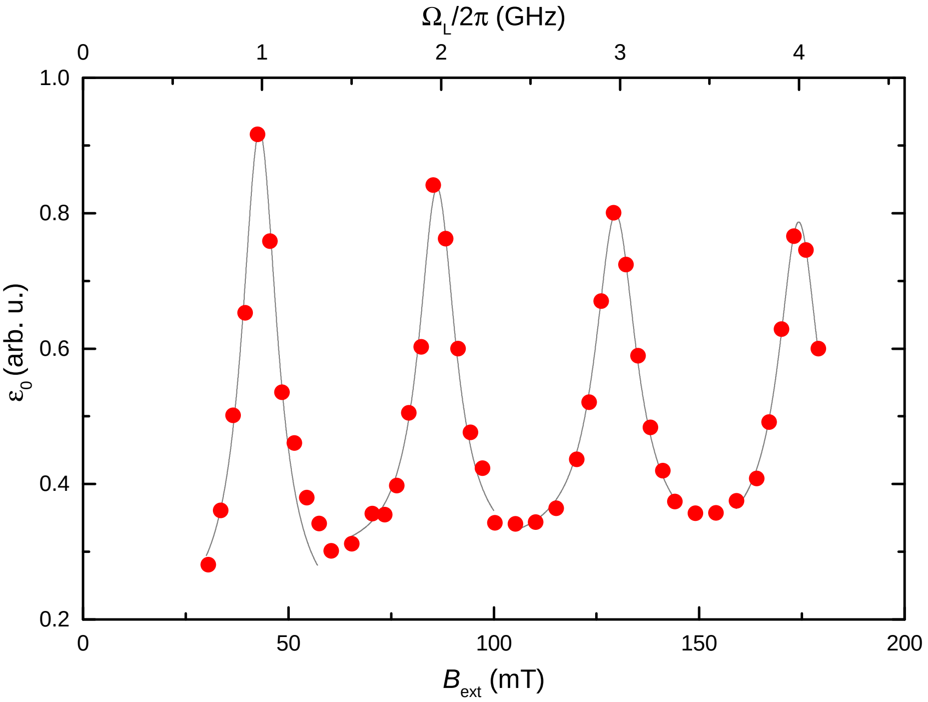

Figure 7.6: Spin precession amplitudes for different external magnetic fields (red circles), extracted from decaying sine fits. They are amplified when the precession frequency f is an integer multiple of the excitation rate, cf. Eq. (5.4). The resonances are fitted with a Lorentzian shape function (grey lines). Sample temperature $T = 10\,\text{K}$, pump power density $13\,\text{W}\,\text{cm}^{-2}$.

The widths for the four peaks are:

$$\begin{cases} \Gamma_{\Omega,1} = (0.240 \pm 0.034)\,\text{GHz} \\ \Gamma_{\Omega,2} = (0.247 \pm 0.023)\,\text{GHz} \\ \Gamma_{\Omega,3} = (0.279 \pm 0.009)\,\text{GHz} \\ \Gamma_{\Omega,4} = (0.270 \pm 0.016)\,\text{GHz}, \end{cases} \tag{7.8}$$

from where follows for the dephasing times:

$$\begin{cases} T^*_{2,1} = (2.1 \pm 0.3)\,\mathrm{ns} \\ T^*_{2,2} = (2.0 \pm 0.2)\,\mathrm{ns} \\ T^*_{2,3} = (1.8 \pm 0.1)\,\mathrm{ns} \\ T^*_{2,4} = (1.9 \pm 0.1)\,\mathrm{ns}. \end{cases} \tag{7.9}$$

The standard deviation of each value is relatively high, so no precise statement about the dependency on the external field is possible. It seems that the value is slightly dropping when increasing H_{ext}. This is easily explained by a spread Δg_e of the electron g-factors when addressing an ensemble of electron spins which causes an inhomogeneous dephasing [Yakovlev and Bayer, 2008].

7.2.2 Analysis by Signal Magnitudes

To analyze the data as in an 'ordinary RSA' analysis, one has to look at the signal magnitude (here: ellipticity) at a certain time point. As mentioned in the beginning of this chapter, the time point is usually set to shortly before the impinging pump pulse which is equal to shortly before the end of one time window. Based on time resolved measurements, we can take the average value from a certain time interval out of the full time traces for each B_{ext} to reduce noise. This is calculated for three different time intervals: $\Delta t = 10 - 20\,\mathrm{ps}$, $5 - 25\,\mathrm{ps}$ and $945 - 995\,\mathrm{ps}$, see colored squares in Fig. 7.7. For each trace four peaks for the four resonance cases are visible but the general shape of them is very noisy, a reasonable analysis by fitting Lorentzian shaped functions to each peak is not possible.

The obstacle with analysing the existing time traces is probably a bad signal-to-noise ratio and, due to a precession lifetime of only about two times of the pump pulse repetition rate, a relatively low contrast in terms of spin precession amplification which leads to broad resonance peaks. Further increasing of the time interval of averaging signal magnitude should enhance the signal-to-noise ratio. We calculate the average magnitude of each acquired time trace. For this, we take the absolute value of each data point of one full time window between two subsequent pump pulses and calculate their average value. Thus, we can improve the RSA plots substantially, see red circles in Fig. 7.8. Now, analogously to the amplitudes extracted from the decaying sine functions, we can fit Lorentzian shaped functions to each peak, see grey solid lines. From the fit parameters for the width we calculate the T_2^* value for each resonance, the results are shown in Tab. 7.1 together with the results from the previous section, see Eqs. (7.9).

One last remark on using the RSA technique for optical orientation measurements with the 1 GHz repetition frequency setup. Usually, around zero field ($B_{\mathrm{ext}} = 0$) there should be also a peak, just like the four peaks visible in Fig. 7.8 for the four resonant fields [Kikkawa and Awschalom, 1998]. The time trace of $\varepsilon(t)$ in this case does not show an oscillatory signal,

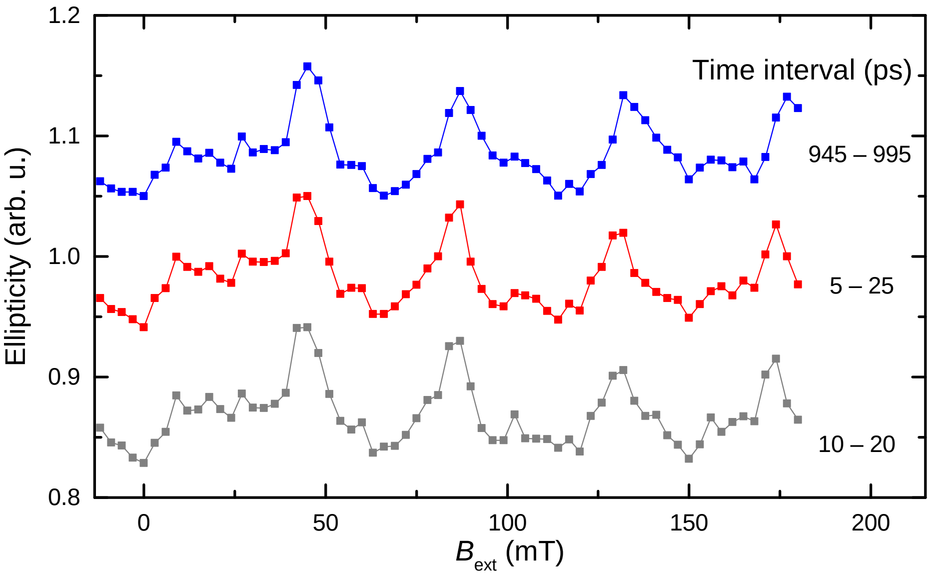

Figure 7.7: RSA plots for three different time intervals. The shape of each curve is similar to Fig. 7.6 but much more noisy. The lines between the squares are just to guide the eyes and without any physical meaning.

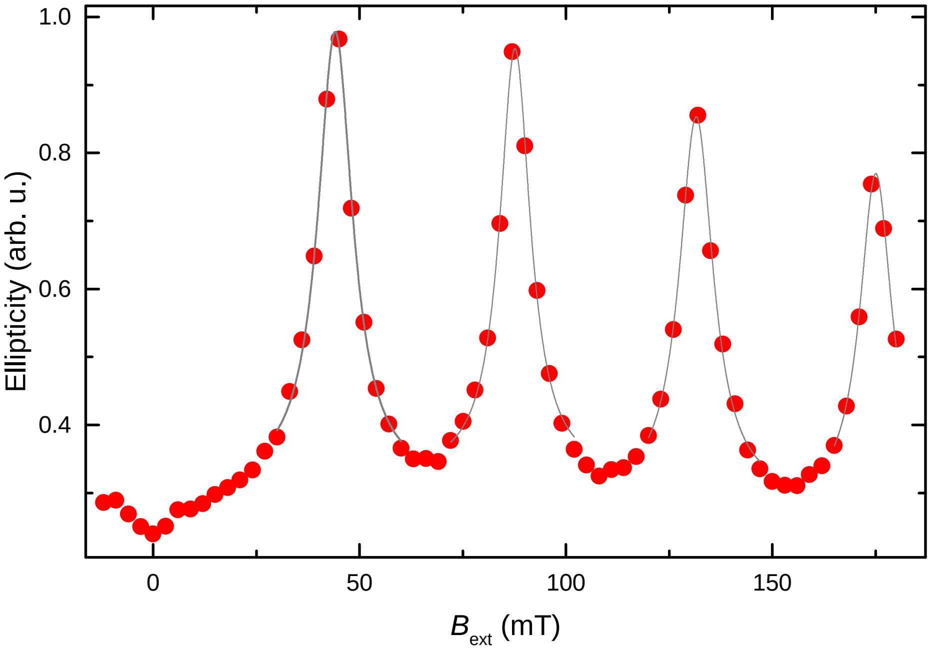

Figure 7.8: RSA spectrum with the first four side resonances. Experimental data displayed by red circles with best fit of Lorentzian shape function to the results, shown by solid grey lines.

	Signal magnitude		Decaying sine fits	
No.	T_2^* [ns]	ΔT_2^* [ns]	T_2^* [ns]	ΔT_2^* [ns]
1	2.3	0.1	2.1	0.3
2	2.4	0.1	2.0	0.2
3	2.3	0.1	1.8	0.1
4	2.3	0.1	1.9	0.1

Table 7.1: Spin dephasing time T_2^*, calculated by the two different analysis methods with standard deviation from fitting Lorentzian shaped functions for the first four side resonances in the CdTe quantum well semiconductor sample.

as there is no Larmor precession, but a constant offset, which reaches its maximum for zero field and decreases when tuning B_{ext} away. Again, the width of the Lorentzian shaped peak gave the spin dephasing time. However, in our measurements this constant offset changed only slightly around $B_{\text{ext}} = 0$, see Fig. 7.8. This is explained by a technical issue of the signal detection. The ellipticity of the transmitted probe was measured by balanced photodiodes with an additional DC filter, which helps to separate the AC oscillations from slower changes of the total signal, thus decreases noise significantly. This filters the constant offset around zero field almost completely out (a very small peak remains) and should be turned off or decreased for future measurements around zero field or where we are interested in constant offsets.

8 Summary and Outlook

Aim of this work was the study of coherent optical pumping of spin systems. The first and the main part was about the perturbation of the magnetization in a magnetically ordered system by a train of circularly polarized femtosecond laser pulses. Due to the usage of a time-resolved spectroscopy employing the ASOPS technique we were able to measure on such a low noise level that we resolved signals as low as 10^{-7} compared to the total DC signal. This is a key factor to detect magnetization precession triggered by the IFE induced by pump pulses with energies of only 50 pJ, which is inevitable when pumping with high repetition rates.

This train of laser pulses excites the magnetization precession resonantly when its frequency F_{osc} is an integer multiple of the excitation frequency F_{Rep}. The precession amplitude is magnified in these cases, and the amplification factor depends on the ratio of the lifetime τ of the excited mode to the pulse repetition time T_{Rep}. For modes with a relatively short lifetime of about $\tau = 0.7\,\mathrm{ns}$ the amplitude is increased by approximately 60 % compared to the anti-resonance case, while for modes with a larger lifetime it can be significantly higher. If it is the scale of about 10 ns, the amplitude is amplified by one order of magnitude. Furthermore, we have shown that the magnetization precession is influenced by the ambient temperature. Cooling the sample down might change its anisotropy energy, which affects the precession properties such as precession lifetime or frequency. Here, more investigations would be necessary for a deeper understanding. First, temperature dependence of the hysteresis loop measurements are required for a fundamental analysis of the change in the precession signal. Second, the same series of measurements should be performed for other samples with different chemical compositions, so one could be able to find the elements which contribute to the strong temperature dependency. If the magnetic rare-earth ions give rise of the anisotropy, then no such effect should be observable for sample-B, which contains none of these ions.

The measurements of propagating spin waves in iron garnets show good agreement with theoretical models. Again, periodic pumping led us to unique features of SW generation. Main advantages are a narrow spectrum despite the optical excitation, and thus, long propagation paths and a pronounced directionality. The resonant excitation establishes a quasi-stationary source of magnons, which we call *magnon cloud*. This local balance of energy arriving from the illuminated pump spot area and the energy carried away by the traveling SWs is accountable for a diminishing decay rate in time of the magnetization precession for sufficiently large distances from the excitation spot. The optical way of SW excitation has some limitations, but our approach with the resonant excitation may significantly broaden its functionality. If the ratio τ/F_{Rep} is large, a small variation by just a few percent of the externally applied magnetic field, which modifies the dispersion relation of the generated SWs, changes the mean wavenumber k_m considerably. Thus, the periodic pumping gives the possibility of a sensitive wavelength tuning by varying setup parameters just slightly.

The next step forward would be the additional implementing of plasmonic structures with which one could concentrate the optical fields to nanometer thick magnetic films onto spot sizes of less than 100 nm in diameter [Liu et al., 2015]. Direct magneto-optic effects can already be increased extraordinarily by plasmonic structures [Belotelov et al., 2011], but the inverse magneto-optic effects are still waiting for the boost by plasmonic implementation.

The third part of investigations within this work was about optical spin orientation and measurements of spin dephasing times in a CdTe/CdMgTe 20 nm quantum well semiconductor structure. Here, we presented a way to optically align the spins of the system and inject a spin precession. Again, if we do this resonantly then the precesison amplitude can be enhanced. This is similar to the resonant spin amplification (RSA) idea, which is a pump probe technique with a constant time delay between both pulses. With the ASOPS based laser system there is no mechanical delay line, and therefore, the time offset cannot be set to a fixed point. Instead, the time-resolved measurements of the spin precession, within the whole period between two subsequent pump pulses, are performed. This has the advantage to not have only the signal magnitude for the different magnetic fields but the whole oscillatory signal from where one can also extract the lifetime and the phase of the precession. This could give a more detailed insight into the physical system. The technical implementation of these measurements could be enhanced to achieve a better signal-to-noise ratio and to decrease the data acquiring times by enlarging the focused pump beam to a larger diameter which lowers the pump density, and thus, thermal heating which shrinks the dephasing time.

Nonetheless, the measurements already showed good agreement with previous published results for optical orientation measurements of confined spin electrons in semiconductor structures. Using a Laser system with an even higher repetition rate would further increase the contrast of the RSA measurements.

All in all we demonstrated different ways of perturbing spin systems optically and when using a train of optical pulses how these effects can be amplified. This is a big difference to most standard pump-probe experiments where each pump laser pulse excited systems which are in their equilibrium position. Our approach enabled us new features and gives us a more detailed knowledge of certain physical properties. Using a laser system with an even higher repetition rate, e.g. $F_{\mathrm{Rep}} = 10\,\mathrm{GHz}$ would increase the contrast of precession amplitude enhancement significantly, thus the cumulative effects should be enlarged as well.

Bibliography

Abragam, A. (1994). *The principles of nuclear magnetism.* International series of monographs on physics. Oxforx: Univ. Press.

Adam, J. D. (1988). Analog signal processing with microwave magnetics. *Proceedings of the IEEE*, 76(2):159–170.

Akimov, I., Puls, J., Rabe, M., and Henneberger, F. (2008). Visible-bandgap ii-vi quantum dot heterostructures. In Bimberg, D., editor, *Semiconductor Nanostructures*, chapter 12. Springer-Verlag Berlin Heidelberg.

Baibich, M. N., Broto, J. M., Fert, A., Van Dau, F. N., Petroff, F., Etienne, P., Creuzet, G., Friederich, A., and Chazelas, J. (1988). Giant magnetoresistance of (001)fe/(001)cr magnetic superlattices. *Phys. Rev. Lett.*, 61:2472–2475.

Bailleul, M., Olligs, D., Fermon, C., and Demokritov, S. O. (2001). Spin waves propagation and confinement in conducting films at the micrometer scale. *EPL (Europhysics Letters)*, 56(5):741.

Bartels, A., Hudert, F., Janke, C., and Dekorsy, T. (2006). Femtosecond time-resolved optical pump-probe spectroscopy at kilohertz-scan-rates over nanosecond-time-delays without mechanical delay line. *Applied Physics Letter*, 88(041117).

Bass, M., DeCusatis, C., Enoch, J., Lakshminarayanan, V., Li, G., MacDonald, C., Mahajan, V., and Van Stryland, E. (2009). *Handbook of Optics, Third Edition Volume II: Design, Fabrication and Testing, Sources and Detectors, Radiometry and Photometry.* Number Bd. 2 in Handbook of Optics. McGraw-Hill Education.

Bauer, M., Mathieu, C., Demokritov, S. O., Hillebrands, B., Kolodin, P. A., Sure, S., Dötsch, H., Grimalsky, V., Rapoport, Y., and Slavin, A. N. (1997). Direct observation of two-dimensional self-focusing of spin waves in magnetic films. *Physical Review B*, 56:R8483–R8486.

Beaurepaire, E., Merle, J.-C., Daunois, A., and Bigot, J.-Y. (1996). Ultrafast spin dynamics in ferromagnetic nickel. *Phys. Rev. Lett.*, 76:4250–4253.

Belotelov, V. I., Akimov, I. A., Pohl, M., Kotov, V. A., Kasture, S., Vengurlekar, A. S., Gopal, A. V., Yakovlev, D. R., Zvezdin, A. K., and Bayer, M. (2011). Enhanced magneto-optical effects in magnetoplasmonic crystals. *Nat Nano*, 6(6):370–376.

Belotelov, V. I. and Zvezdin, A. K. (2012). Inverse transverse magneto-optical kerr effect. *Physical Review B*, 86:155133.

Binasch, G., Grünberg, P., Saurenbach, F., and Zinn, W. (1989). Enhanced magnetoresistance in layered magnetic structures with antiferromagnetic interlayer exchange. *Phys. Rev. B*, 39:4828–4830.

Birt, D. R., OíGorman, B., Tsoi, M., Li, X., Demidov, V. E., and Demokritov, S. O. (2009). Diffraction of spin waves from a submicrometer-size defect in a microwaveguide. *Applied Physics Letters*, 95(12):122510.

Bloch, F. (1930). Zur theorie des ferromagnetismus. *Zeitschrift für Physik*, 61(3):206–219.

Bossini, D. and Rasing, T. (2017). Femtosecond optomagnetism in dielectric antiferromagnets. *Physica Scripta*, 92(2):024002.

Cardona, M., Christensen, N., and Fasol, G. (1988). Relativistic band structure and spin-orbit splitting of zinc-blende-type semiconductors. *Physical Review B*, 38(3):1806.

Chernov, A. I., Kozhaev, M. A., Savochkin, I. V., Dodonov, D. V., Vetoshko, P. M., Zvezdin, A. K., and Belotelov, V. I. (2017). Optical excitation of spin waves in epitaxial iron garnet films: Mssw vs bvmsw. *Opt. Lett.*, 42(2):279–282.

Choi, S., Lee, K.-S., and Kim, S.-K. (2006). Spin-wave interference. *Applied Physics Letters*, 89(6):062501.

Chumak, A. V., Serga, A. A., and Hillebrands, B. (2014). Magnon transistor for all-magnon data processing. *Nature Communications*, 5:4700.

Chumak, A. V., Vasyuchka, V. I., Serga, A. A., and Hillebrands, B. (2015). Magnon spintronics. *Nat Phys*, 11(6):453–461.

Cohen-Tannoudji, C. N. (1998). Nobel lecture: Manipulating atoms with photons. *Reviews of Modern Physics*, 70(3):707.

Damon, R. and Eshbach, J. (1961). Magnetostatic modes of a ferromagnet slab. *Journal of Physics and Chemistry of Solids*, 19(3):308 – 320.

Damon, R. W. and Vaart, H. V. D. (1965). Propagation of magnetostatic spin waves at microwave frequencies in a normally magnetized disk. *Journal of Applied Physics*, 36(11):3453–3459.

Davis, J. A., Venkatesan, R., Kaloyeros, A., Beylansky, M., Souri, S. J., Banerjee, K., Saraswat, K. C., Rahman, A., Reif, R., and Meindl, J. D. (2001). Interconnect limits on gigascale integration (gsi) in the 21st century. *Proceedings of the IEEE*, 89(3):305–324.

Delone, N. B. and Krainov, V. P. (1999). Ac stark shift of atomic energy levels. *Physics-Uspekhi*, 42(7):669.

Demidov, V. E., Jersch, J., Rott, K., Krzysteczko, P., Reiss, G., and Demokritov, S. O. (2009a). Nonlinear propagation of spin waves in microscopic magnetic stripes. *Physical Review Letters*, 102:177207.

Demidov, V. E., Kostylev, M. P., Rott, K., Krzysteczko, P., Reiss, G., and Demokritov, S. O. (2009b). Excitation of microwaveguide modes by a stripe antenna. *Applied Physics Letters*, 95(11):112509.

Demokritov, S. O., Demidov, V. E., Dzyapko, O., Melkov, G. A., Serga, A. A., Hillebrands, B., and Slavin, A. N. (2006). Bose-einstein condensation of quasi-equilibrium magnons at room temperature under pumping. *Nature*, 443(7110):430–433.

Dirac, P. A. M. (1926). On the theory of quantum mechanics. *Proceedings of the Royal Society of London. Series A, Containing Papers of a Mathematical and Physical Character*, 112(762):661–677.

DiVincenzo, D. P. (1995). Quantum computation. *Science*, 270(5234):255–261.

du Tremolet de Lacheisserie, E., Gignoux, D., and Schlenker, M., editors (2005). *Magnetism - Fundamentals*. Springer Science+Business Media.

Dutta, S., Chang, S.-C., Kani, N., Nikonov, D. E., Manipatruni, S., Young, I. A., and Naeemi, A. (2015). Non-volatile clocked spin wave interconnect for beyond-cmos nanomagnet pipelines. *Scientific Reports*, 5:9861.

Dyson, F. J. (1956). General theory of spin-wave interactions. *Phys. Rev.*, 102:1217–1230.

Eshbach, J. R. (1962). Spin-wave propagation and the magnetoelastic interaction in yttrium iron garnet. *Phys. Rev. Lett.*, 8:357–359.

Eshbach, J. R. and Damon, R. W. (1960). Surface magnetostatic modes and surface spin waves. *Phys. Rev.*, 118:1208–1210.

Faraday, M. (1846). On the magnetization of light and the illumination of magnetic lines of force. *Philosophical transactions of the Royal Society*, 136:104–123.

Finkelstein, G., Shtrikman, H., and Bar-Joseph, I. (1995). Optical spectroscopy of a two-dimensional electron gas near the metal-insulator transition. *Phys. Rev. Lett.*, 74:976–979.

Fonthal, G., Tirado-MejÌa, L., MarÌn-Hurtado, J., Ariza-CalderÛn, H., and Mendoza-Alvarez, J. (2000). Temperature dependence of the band gap energy of crystalline cdte. *Journal of Physics and Chemistry of Solids*, 61(4):579 – 583.

Freiser, M. (1968). A survey of magnetooptic effects. *IEEE Transactions on Magnetics*, 4(2):152–161.

Garcia-Otero, J., Porto, M., Rivas, J., and Bunde, A. (1999). Influence of the cubic anisotropy constants on the hysteresis loops of single-domain particles: A monte carlo study. *Journal of Applied Physics*, 85(4):2287–2292.

Gebs, R., Klatt, G., Janke, C., Dekorsy, T., and Bartels, A. (2010). Sub-50 fs time-domain spectroscopy using high-speed asops. In *Conference on Lasers and Electro-Optics 2010*, page CMA1. Optical Society of America.

Getzlaff, M. (2007). *Fundamentals of Magnetism.* Springer Berlin Heidelberg.

Gieniusz, R. and Smoczynski, L. (1986). Magnetostatic spin waves in (111)-oriented thin garnet films with combined cubic and uniaxial anisotropies. *Journal of Magnetism and Magnetic Materials*, 66:366–372.

Gilbert, T. A. (1955). Equation of motion of magnetization. *Armor Research Foundation Rep.*, 11.

Gilleo, M. A. and Geller, S. (1958). Magnetic and crystallographic properties of substituted yttrium-iron garnet, $3\mathrm{y}_2\mathrm{o}_3 \cdot x\mathrm{m}_2\mathrm{o}_3 \cdot (5 - x)\mathrm{fe}_2\mathrm{o}_3$. *Phys. Rev.*, 110:73–78.

Goedsche, F. (1970). Reflection and refraction of spin waves. *physica status solidi (b)*, 39(1):K29–K33.

Gorobets, Y. I. and Reshetnyak, S. A. (1998). Reflection and refraction of spin waves in uniaxial magnets in the geometrical-optics approximation. *Technical Physics*, 43(2):188–191.

Griffiths, J. H. E. (1946). Anomalous high-frequency resistance of ferromagnetic metals. *Nature*, 158:670–671.

Gurevich, A. G. and Melkov, G. A. (1996). *Magnetization Oscillations and Waves.* CRC Press, Inc.

Hansteen, F., Kimel, A., Kirilyuk, A., and Rasing, T. (2006). Nonthermal ultrafast optical control of the magnetization in garnet films. *Phys. Rev. B*, 73:014421.

Hauser, C., Richter, T., Homonnay, N., Eisenschmidt, C., Qaid, M., Deniz, H., Hesse, D., Sawicki, M., Ebbinghaus, S. G., and Schmidt, G. (2016). Yttrium iron garnet thin films with very low damping obtained by recrystallization of amorphous material. *Scientific Report*, 6:20827.

Heisenberg, W. (1926). Mehrkörperproblem und resonanz in der quantenmechanik. *Zeitschrift für Physik*, 38(6):411–426.

Herman, M. A. and Sitter, H. (1996). *Molecular Beam Epitaxy*, volume 7 of *Springer Series in Materials Science*. Springer-Verlage Berlin Heidelberg.

Holstein, T. and Primakoff, H. (1940). Field dependence of the intrinsic domain magnetization of a ferromagnet. *Phys. Rev.*, 58:1098–1113.

Hung, D. S., Fu, Y. P., Lee, S. F., Yao, Y. D., and Ahad, F. B. A. (2010). Relaxation behaviors of the bismuth-substituted yttrium iron garnet in the microwave range. *Journal of Applied Physics*, 107.

Jäckl, M., Belotelov, V. I., Akimov, I. A., Savochkin, I. V., Yakovlev, D. R., Zvezdin, A. K., and Bayer, M. (2017). Magnon accumulation by clocked laser excitation as source of long-range spin waves in transparent magnetic films. *Phys. Rev. X*, 7:021009.

Kabos, P. and Stalmachov, V. S. (1994). *Magnetostatic Waves and Their Applications.* Chapman & Hall, London.

Kahl, S., Popov, V., and Grishin, A. M. (2003). Optical transmission and faraday rotation spectra of a bismuth iron garnet film. *Journal of Applied Physics*, 94(9):5688–5694.

Kalashnikova, A. M., Kimel, A. V., Pisarev, R. V., Gridnev, V. N., Kirilyuk, A., and Rasing, T. (2007). Impulsive generation of coherent magnons by linearly polarized light in the easy-plane antiferromagnet febo$_3$. *Physical Review Letters*, 99:167205.

Kalinikos, B. A. (1980). Excitation of propagating spin waves in ferromagnetic films. *Microwaves, Optics and Antennas, IEE Proceedings H*, 127(1):4–.

Kasap, S. and Capper, P., editors (2006). *Springer Handbook of Electronic and Photonic Materials.* Springer Science & Business Media.

Kerr, J. (1877). Xliii. on rotation of the plane of polarization by reflection from the pole of a magnet. *Philosophical Magazine Series 5*, 3(19):321–343.

Khitun, A., Bao, M., and Wang, K. L. (2010). Magnonic logic circuits. *Journal of Physics D: Applied Physics*, 43(26):264005.

Kikkawa, J. and Awschalom, D. (1998). Resonant spin amplification in n-type gaas. *Physical Review Letters*, 80(19):4313.

Kimel, A., Kirilyuk, A., and Rasing, T. (2007). Femtosecond opto-magnetism: ultrafast laser manipulation of magnetic materials. *Laser & Photonics Reviews*, 1(3):275–287.

Kimel, A. V., Kirilyuk, A., Usachev, P. A., Pisarev, R. V., Balbashov, A. M., and Rasing, T. (2005). Ultrafast non-thermal control of magnetization by instantaneous photomagnetic pulses. *Nature*, 435:655–657.

Kirilyuk, A., Kimel, A. V., and Rasing, T. (2010). Ultrafast optical manipulation of magnetic order. *Rev. Mod. Phys.*, 82:2731–2784.

Kittel, C. (1947). Interpretation of anomalous larmor frequencies in ferromagnetic resonance experiment. *Physical Review*, 71(4):270.

Kittel, C. (1948). On the theory of ferromagnetic resonance absorption. *Physical Review*, 73(2):155–161.

Kittel, C. (2004). *Introduction to Solid State Physics*. John Wiley and Sons Ltd.

Klingshirn, C., editor (2004). *CdTe quantum wells*, pages 13–48. Springer Berlin Heidelberg.

Kostylev, M. P., Serga, A. A., Schneider, T., Leven, B., and Hillebrands, B. (2005). Spin-wave logical gates. *Applied Physics Letters*, 87(15):153501.

Kozhanov, A., Ouellette, D., Rodwell, M., Allen, S. J., Jacob, A. P., Lee, D. W., and Wang, S. X. (2009). Dispersion and spin wave 'tunneling' in nanostructured magnetostatic spin waveguides. *Journal of Applied Physics*, 105(7):07D311.

Kruglyak, V. and Hicken, R. (2006). Magnonics: Experiment to prove the concept. *Journal of Magnetism and Magnetic Materials*, 306(2):191 – 194.

Kruglyak, V. V., Demokritov, S. O., and Grundler, D. (2010). Magnonics. *Journal of Physics D: Applied Physics*, 43(26):264001.

Ladd, T. D., Jelezko, F., Laflamme, R., Nakamura, Y., Monroe, C., and O/'Brien, J. L. (2010). Quantum computers. *Nature*, 464(7285):45–53.

Landau, L. and Lifshitz, E. (1935). On the theory of the dispersion of magnetic permeability in ferromagnetic bodies. *Phys. Z. Union.*, 8:153–164.

Lenk, B., Ulrichs, H., Garbs, F., and M¸nzenberg, M. (2011). The building blocks of magnonics. *Physics Reports*, 507(4):107 – 136.

Liu, T.-M., Wang, T., Reid, A. H., Savoini, M., Wu, X., Koene, B., Granitzka, P., Graves, C. E., Higley, D. J., Chen, Z., Razinskas, G., Hantschmann, M., Scherz, A., Stˆhr, J., Tsukamoto, A., Hecht, B., Kimel, A. V., Kirilyuk, A., Rasing, T., and D¸rr, H. A. (2015). Nanoscale confinement of all-optical magnetic switching in tbfeco - competition with nanoscale heterogeneity. *Nano Letters*, 15(10):6862–6868. PMID: 26312732.

Maekawa, S. (2006). *Concepts in Spin Electronics*. Oxford science publications. OUP Oxford.

Menzer, G. (1930). *Die Kristallstruktur der Granate*. Akad. Verlagsges., Leipzig.

Moore, G. E. (1965). Cramming more components onto integrated circuits. *Electronics*, 38(8).

Nikonov, D. E. and Young, I. A. (2013). Overview of beyond-cmos devices and a uniform methodology for their benchmarking. *Proceedings of the IEEE*, 101(12):2498–2533.

O'Handley, R. C. (2000). *Modern magnetic materials: principles and applications*. Wiley, New York.

Owens, J. M., Collins, J. H., and Carter, R. L. (1985). System applications of magnetostatic wave devices. *Circuits, Systems and Signal Processing*, 4(1):317–334.

Pauli, W. (1925). Über den zusammenhang des abschlusses der elektronengruppen im atom mit der komplexstruktur der spektren. *Zeitschrift für Physik*, 31(1):765–783.

Pershan, P. S. (1963). Nonlinear optical properties of solids: Energy considerations. *Physical Review*, 130(3):919–929.

Pershan, P. S., van der Ziel, J. P., and Malmstrom, L. D. (1966). Theoretical discussion of the inverse faraday effect, raman scattering, and related phenomena. *Physical Review*, 143(2):574–583.

Petta, J. R., Johnson, A. C., Taylor, J. M., Laird, E. A., Yacoby, A., Lukin, M. D., Marcus, C. M., Hanson, M. P., and Gossard, A. C. (2005). Coherent manipulation of coupled electron spins in semiconductor quantum dots. *Science*, 309(5744):2180–2184.

Pitaevskii, L. P. (1961). Electric forces in a transparent dispersive medium. *Soviet Physics JETP*, 12(5):1008–1013.

Popova, D., Bringer, A., and Blügel, S. (2012). Theoretical investigation of the inverse faraday effect via a stimulated raman scattering process. *Phys. Rev. B*, 85:094419.

Prasankumar, R. and Taylor, A. (2016). *Optical Techniques for Solid-State Materials Characterization*. CRC Press.

Reinsel, D., Gantz, J., and Rydning, J. (2017). Data age 2025: The evolution of data to life-critical.

Robertson, J. M., Wittekoek, S., Popma, T. J. A., and Bongers, P. F. (1973). Preparation and optical properties of single crystal thin films of bismuth substituted iron garnets for magneto-optic applications. *Applied physics*, 2(5):219–228.

Satoh, T., Terui, Y., Moriya, R., Ivanov, B. A., Ando, K., Saitoh, E., Shimura, T., and Kuroda, K. (2012). Directional control of spin-wave emission by spatially shaped light. *Nat Photon*, 6(10):662–666.

Savochkin, I., Jackl, M., Belotelov, V., Akimov, I., Sylgacheva, D., Chernov, A., Shaposhnikov, A., Prokopov, A., Berzhansky, V., Yakovlev, D., Zvezdin, A., and Bayer, M. (2017). Generation of spin waves by a train of fs-laser pulses: a novel approach for tuning magnon wavelength. *Scientific Reports*, 7:5668.

Scott, G. and Lacklison, D. (1976). Magnetooptic properties and applications of bismuth substituted iron garnetssco. *IEEE Transactions on Magnetics*, 12(4):292–311.

Seeger, K. (1991). *Semiconductor Physics*, volume 40 of *Springer Series in Solid-State Sciences*. Springer-Verlag Berlin Heidelberg.

Serga, A. A., Chumak, A. V., and Hillebrands, B. (2010). Yig magnonics. *Journal of Physics D: Applied Physics*, 43(26):264002.

Shen, Y. R. and Bloembergen, N. (1966). Interaction between light waves and spin waves. *Physical Review*, 143:372–384.

Stancil, D. D. and Prabhakar, A. (2009). *Spin Waves: Theory and Applications*. Springer.

Stolze, J. and Suter, D. (2008). *Quantum Computing: A Short course from Theory to Experiment*. Wiley-VCH.

Stupakiewicz, A., Szerenos, K., Afanasiev, D., Kirilyuk, A., and Kimel, A. V. (2017). Ultrafast nonthermal photo-magnetic recording in a transparent medium. *Nature*, 542(7639):71–74.

Tabuchi, Y., Ishino, S., Noguchi, A., Ishikawa, T., Yamazaki, R., Usami, K., and Nakamura, Y. (2015). Coherent coupling between a ferromagnetic magnon and a superconducting qubit. *Science*, 349(6246):405–408.

Uchida, K., Adachi, H., Kikuchi, D., Ito, S., Qiu, Z., Maekawa, S., and Saitoh, E. (2015). Generation of spin currents by surface plasmon resonance. *Nature Communications*, 6:5910.

van der Ziel, J. P., Pershan, P. S., and Malmstrom, L. D. (1965). Optical-induced magnetization resulting from the inverse faraday effect. *Physical Review Letters*, 15(5):190–193.

van Kampen, M., Jozsa, C., Kohlhepp, J. T., LeClair, P., Lagae, L., de Jonge, W. J. M., and Koopmans, B. (2002). All-optical probe of coherent spin waves. *Phys. Rev. Lett.*, 88:227201.

van Vleck, J. H. (1937). On the anisotropy of cubic ferromagnetic crystals. *Phys. Rev.*, 52:1178–1198.

van Vleck, J. H. (1977). Quantum mechanics - the key to understanding magnetism. In Lundqvist, S., editor, *Noble Lectures*. World Scientific Publishing Co.

Vashkovsky, A. V. and Lock, E. H. (2006). Properties of backward electromagnetic waves and negative reflection in ferrite films. *Physics-Uspekhi*, 49(4):389.

Verba, R., Carpentieri, M., Finocchio, G., Tiberkevich, V., and Slavin, A. (2016). Excitation of propagating spin waves in ferromagnetic nanowires by microwave voltage-controlled magnetic anisotropy. *Scientific Reports*, 6:25018.

Vlaminck, V. and Bailleul, M. (2008). Current-induced spin-wave doppler shift. *Science*, 322(5900):410–413.

Waldrop, M. M. (2016). More than moore. *Nature*, 530:144–147.

Walker, L. R. (1957). Magnetostatic modes in ferromagnetic resonance. *Phys. Rev.*, 105:390–399.

Wesenberg, J. H., Ardavan, A., Briggs, G. A. D., Morton, J. J. L., Schoelkopf, R. J., Schuster, D. I., and Mølmer, K. (2009). Quantum computing with an electron spin ensemble. *Phys. Rev. Lett.*, 103:070502.

Wettling, W., Andlauer, B., Koidl, P., Schneider, J., and Tolksdorf, W. (1973). Optical absorption and faraday rotation in yttrium iron garnet. *physica status solidi (b)*, 59(1):63–70.

Williams, M., Tomlinson, R., and Hampshire, M. (1969). X-ray determination of the lattice parameters and thermal expansion of cadmium telluride in the temperature range 20-240. *Solid State Communications*, 7(24):1831 – 1832.

Winkler, G. (1981). *Magnetic Garnets*, volume 5 of *Vieweg Tracts in Pure and Applied Physics*. Friedr. Vieweg & Sohn, Braunschweig/Wiesbaden.

Yakovlev, D. and Bayer, M. (2008). Coherent spin dynamics of carriers. In Dyakonov, M., editor, *Spin Physics in Semiconductors*, chapter 6. Springer-Verlag Berlin Heidelberg.

Yugova, I. A., Glazov, M. M., Yakovlev, D. R., Sokolova, A. A., and Bayer, M. (2012). Coherent spin dynamics of electrons and holes in semiconductor quantum wells and quantum dots under periodical optical excitation: Resonant spin amplification versus spin mode locking. *Phys. Rev. B*, 85:125304.

Zhang, X., Zou, C.-L., Zhu, N., Marquardt, F., Jiang, L., and Tang, H. X. (2015). Magnon dark modes and gradient memory. *Nature Communications*, 6:8914.

Zhukov, E. A., Yakovlev, D. R., Bayer, M., Glazov, M. M., Ivchenko, E. L., Karczewski, G., Wojtowicz, T., and Kossut, J. (2007). Spin coherence of a two-dimensional electron gas induced by resonant excitation of trions and excitons in CdTe?(Cd, Mg)Te quantum wells. *Phys. Rev. B*, 76:205310.

Zvezdin, A. K. and Kotov, V. A. (1997). *Modern Magnetooptics and Magnetooptical Materials*. Condensed Matter Physics.

Acknowledgment

Finally I want to express my greatest gratitude towards all the people who supported me during the time I worked on this thesis and without whom it would not exist in the way it does now.

At first, my acknowledgments goes to Prof. Manfred Bayer for the confidence and enabling me the opportunity to do my research work at his chair which he is leading in an excellent way, and where I benefited from uncountable collective years of intense experience and knowledge in scientific research.

I am also particularly thankful to Dr. Ilya Akimov who supervised me during my years of being an PhD student. I profited from his enormous experience in experimental physics innumerable times when I came to a dead end of my own ideas and I have learned from his ways of researching a lot for myself. I am happy that I was able to do my PhD under his supervision and would always come to the same decision again.

Dr. Vladimir Belotelov and his PhD student Igor Savochkin from the Lomonosov Moscow State University contributed a substantial help for theoretical understanding and analyzing of the experimentally observed phenomena and always answered patiently my questions about theoretical problems. Additionally, Igor helped also with some experimental realizations during his visits in Dortmund.

I am also very thankful to all my colleagues at the E2 chair. Always open to help where it is possible even if the effort for it goes far beyond what one could expect. In particular, I want to thank my current or former office neighbors Felix Spitzer, Jonas Vondran and Markus Kuhnert. And thank you a million times, Jonas, for checking this thesis for orthographic or grammatical errors.

A special thanks goes to my former supervisor during my Master thesis, Lars Kreilkamp. His enthusiasm in physics is exceptional and rubbed off on me. I am not sure if I would have chosen to do my PhD if I had not worked with him.

At last but not least, the greatest acknowledgment goes to my mother who supported my mentally and financially during my whole study and the PhD years. She gave me the confidence to study physics and without that, who knows what I would be doing now?